

Prediction of Liner Cavitation Occurrence Induced by Piston Slap in the Internal Combustion Engine Considering Acoustic Characteristics of Water Coolant Passage

王, 暁宇

<https://doi.org/10.15017/1543964>

出版情報：九州大学, 2015, 博士（工学）, 課程博士
バージョン：
権利関係：全文ファイル公表済

**Prediction of Liner Cavitation Occurrence Induced by Piston Slap
in the Internal Combustion Engine Considering Acoustic
Characteristics of Water Coolant Passage**

Doctoral Thesis

June 2015

Wang Xiaoyu

Supervisor

Kazuhide OHTA (Professor)

Department of Mechanical Engineering

Kyushu University

TABLE OF CONTENTS

Chapter 1 Introduction	1
1.1 Cavitation	1
1.2 Cavitation erosion	3
1.3 Liner cavitation	6
1.4 Objective of this research and topics of discussion	14
Chapter 2 Numerical method to predict water pressure fluctuation considering dynamic characteristics of engine structure and water acoustic field	15
2.1 FEM formulations of dynamic response of engine structure and water acoustic field in water coolant passage	18
2.2 Application of modal analysis technique	19
2.3 Dynamic characteristics of structure and acoustic field coupled system	22
2.4 Dynamic response of total engine system in running condition	27
2.5 Chapter summary	34
Chapter 3 Evaluation of numerical method by use of rectangular tank model	35
3.1 Rectangular tank model	35
3.2 FEM model of acoustic field	39
3.3 Pressure fluctuation and structure acceleration induced by impact force	41
3.4 Effect of variation of sound speed	46
3.5 Chapter summary	51
Chapter 4 Application of the numerical method to the internal combustion engine	52
4.1 Vibration characteristics of water acoustic field	52
4.2 Vibration characteristics of coupled system of crankcase and water coolant passage	66
4.3 Prediction of pressure fluctuation induced by piston slap force	72
4.4 Pressure fluctuation in running condition	85
4.5 Chapter summary	90
Chapter 5 Conclusion	91
Acknowledgement	93
Reference	94
Appendix	100

Chapter 1

INTRODUCTION

1.1 Cavitation

When it comes to vaporization of fluid, two physical phenomena are under consideration, boiling and cavitation. Boiling is common in daily life, which implies that the formation of bubbles is caused by increasing fluid temperature at constant pressure. On the other hand, cavitation describes the formation of voids in a fluid when the pressure is reduced to a certain critical value without change in the ambient temperature. In the thermodynamics phase diagram as shown in Fig.1.1 [1], the curve from Triple point T_r (where the three phase of substance can coexist) to Critical point C (where liquid and vapor can coexist) separates the liquid and vapor domains. Crossing that curve represents a reversible transformation between liquid and vapor under static conditions. Liquid can be transformed into vapor by either increasing temperature or lowering pressure. Vapor pressure P_v of water is a function of temperature T . As temperature T increases, the vapor pressure increases exponentially [2]. In Fig.1.2, at around 80°C which is the working temperature of coolant of internal combustion engine, the vapor pressure is about 48kPa. Cavitation is similar to boiling except the driving mechanism is not temperature change but pressure change.

The first mention of cavitation came from Isaac Newton in the paper entitled "Opticks" in 1704. "A little white spot" was detected during his observation of Newton's rings formed between a lens and a plane glass in water [3]. The experiment of observation of cavitation flows through venturi tube was first exhibited by Reynolds in 1894 [4]. Reynolds discovered the formation of bubbles at relatively high speed of fluid, which is in accordance with Bernoulli's law. The first attempt to give a theory of the destructive action of cavities was made by Cook. [5]. In 1917, Rayleigh improved Cook's theory under the same preconditions proposed by Besant [6], which assumed the liquid to be incompressible, neglecting viscosity, and supposed

that there was an absolute vacuum within the cavity. Rayleigh deduced the radial velocity of the boundary of the cavity, which can be expressed in terms of the radius as shown in Eq.(1.1).

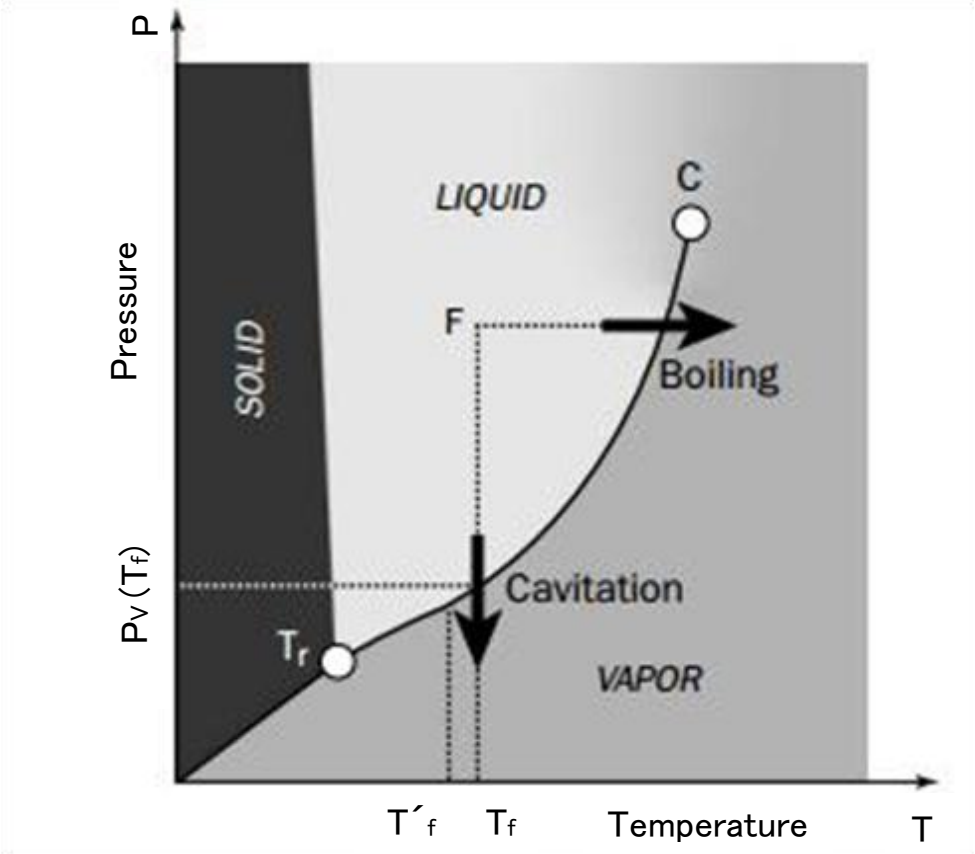


Fig.1.1 Three phase diagram of water [1]

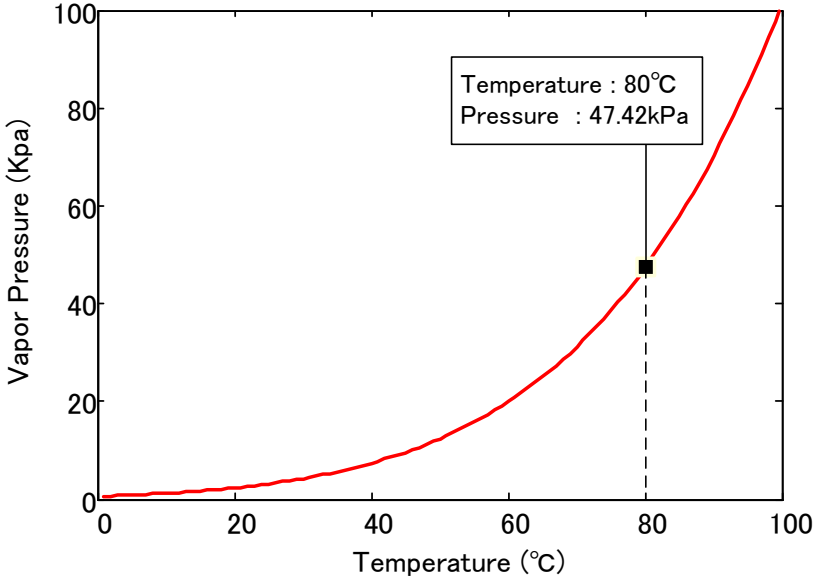


Fig.1.2 Vapor pressure of water changing with temperature [2]

$$U^2 = \frac{2P}{3\rho} \left(\frac{R_0^3}{R^3} - 1 \right) \quad (1.1)$$

where, P is the hydrostatic pressure at infinity, ρ is the density of the liquid, R is the radius of the boundary of cavity at the moment under consideration, R_0 is the initial value of R . Rayleigh also calculated that the pressure arising in the vicinity of the cavity has a maximum value at a distance of $1.57R$ from its center. If the supposition of incompressibility is still maintained, an infinite pressure may result, but if the compressibility is admitted, the instantaneous pressure P' is finite and can be given by the Eq.(1.2) [7].

$$\frac{(P')^2}{2\beta'} = \frac{P}{3} \left(\frac{R_0^3}{R^3} - 1 \right) \quad (1.2)$$

where, β' is the coefficient of compressibility. Different from the assumptions of Rayleigh's analysis, liquids in reality are both compressible and viscous and there is a certain amount of vapor or gas within the cavities, so Rayleigh only indicated the possibility of extremely high pressure and velocity near the point of bubble collapse. Rayleigh's work did lay good foundation for the exploration of cavitation for the coming researchers.

1.2 Cavitation erosion

In most cases, cavitation is associated with cavitation erosion which gives rise to pitting on the neighboring solid surfaces. General agreement can be concluded that damage due to cavitation erosion is caused by repeated mechanical forces acting on the solid surface as a result of bubble collapse. The collapse of bubbles in very short time can produce very high local pressure to remove small amount of metal from the adjacent surface. The bubbles or cavities are brought by the relatively low pressure of liquid. In order to study the mechanism of cavitation erosion process, numerical analysis of collapse of bubbles under different assumptions and experiments of observing cavitation bubbles have been carried out [8~19].

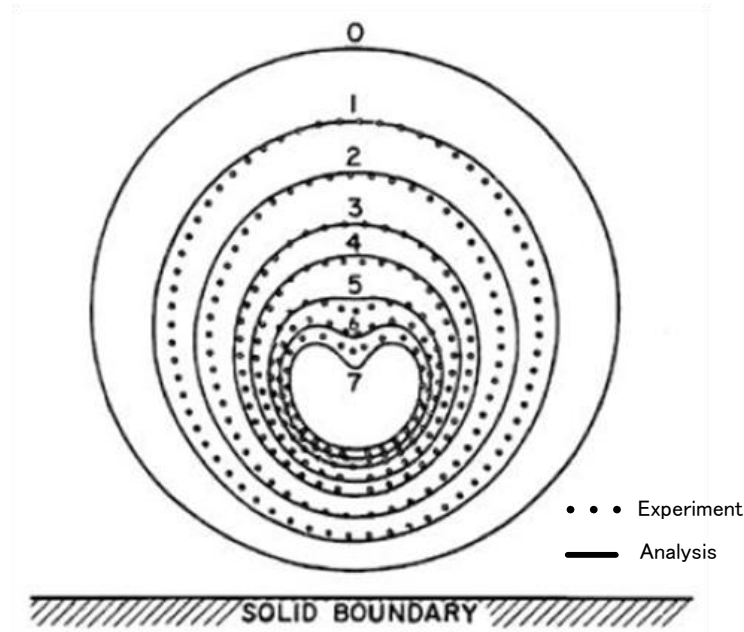


Fig.1.3 Comparison of experimentally determined bubble shapes (dotted line) of a spherical bubble near a plane solid wall with theoretical curves (solid line) [13].

Rayleigh took the foundational step on numerical analysis of the collapse of an empty cavity in liquid and pointed out that the pressure in the liquid adjacent to the cavity wall could be very high. On the basis of Rayleigh's work, Hickling and Plesset [8] calculated the pressure pulse at the vicinity of collapse and the subsequent rebound of spherical bubble containing a small amount of gas in the compressible fluid. The results indicated that the stress fell off rapidly as the distance from the bubble increased and was too small to damage solid surface unless the surface is quite close to the bubble. Yeh and Yang [9] analyzed the dynamic behavior of a moving gas bubble induced by the flow field with a non-uniform pressure gradient. The bubble size, shape and the translational velocity were calculated under the assumptions of constant liquid density and neglecting the effects of heat transfer. Kornfeld and Suvorov [10] suggested that cavitation bubbles might collapse asymmetrically and produce a liquid jet which caused damage on the solid surface. Benjamin and Ellis [11] confirmed the liquid jets which were assumed by Kornfeld and Suvorov through experiments of collapsing bubbles near a solid wall. They observed that these bubbles firstly became elongated in the direction normal to the wall; then tended to flatten and form an inward moving jet on the side of the bubble against the

wall. Plesset and Chapman [12] calculated the liquid jet developing through the bubble towards the solid surface during the collapse of an empty asymmetry bubble close to the solid surface. They also conducted the numerical techniques to trace models of individual cavitation bubbles as far into their collapse as possible under a number of asymmetric initial and boundary conditions. As shown in Fig.1.3, the theoretical curves taken from the calculation results of Plesset and Chapman has been verified 5 years later by experiment conducted by Lauterborn and Bolle [13]. Challier and Rebound [14] introduced a new parameter which was defined as the ratio between the pressure wave energy and the generated pit volume to evaluate the interaction between pressure wave emitted during vapor structures collapses and neighboring solid boundaries by numerical simulations concerning spherical bubble implosions and material deformation. Chen and Li [15] performed experiment and numerical simulation of bubble collapse process to study the damage mechanism in the incubation stage of vibration cavitation erosion. The results showed that there were three typical kinds of erosion pits--- complete, incomplete and thermal pits which were mainly caused by micro-jet, shock wave and high temperature respectively. This jet passes across the cavity, penetrates the further surface of cavity and hits the solid surface. Shock wave can even destroy the structure of the surface material.

In experiments of cavitation research, the facilities of generating cavities and observing formation and collapse of bubbles play a vital role. In 1960s, Hammitt's laboratory [16] used a flowing system of water tunnel facility and various high speed photographic systems to observe the collapse mode of cavitation bubbles and the damage produced by the collapsing bubbles through the impact of high speed water jets. In 1970s, laser was used to produce highly controlled cavitation bubbles without mechanical destruction, which also opened up a new area called optical cavitation [13][17]. Nowadays, vibration cavitation erosion can be performed with the help of ultrasonic transducer [18]. Formation and evolution of erosion pit can be observed by SEM (Scanning Electro Microscope) and high speed camera in order to investigate

the damage mechanism of cavitation erosion [19].

In practical devices, the negative effect caused by cavitation is diverse. Almost all hydrodynamic systems are confronting the problems of cavitation, such as pumps, propellers, hydraulic turbines and cylinder liners etc. However, every coin has two sides, there are also positive applications of cavitation, such as rock cutting by cavitation as it flows through a rough rock surface and cavitation generators that can enlarge the solubility of oxygen in fish farming industry.

1.3 Liner cavitation

Cavitation erosion found on the exterior side of cylinder liners has been bothering the designers and users of internal combustion engine for decades since 1940s [20~23]. A ship engine was first found to stop operation by cavitation erosion of liners after only 800 hours [24]. Liner cavitation erosion is usually featured by a longitudinal band of honeycombed surface from the top to the bottom of liners on thrust side as shown in Fig.1.4. The degree and size of erosion as well as the form and distribution on the affected zones can vary from engine to engine and from cylinder to cylinder within the same engine, which is due to various reasons such as variation in liner vibration levels, different coolant temperatures, different coolant pressure of localized flow and the vibration characteristics of acoustic field of water coolant passage. Variation of liner vibration levels may be caused by factors such as variations of piston and liners dimensions, the engine block machining variations. [25].



Fig.1.4 Cavitation erosion on the thrust side of real engine cylinder [25]

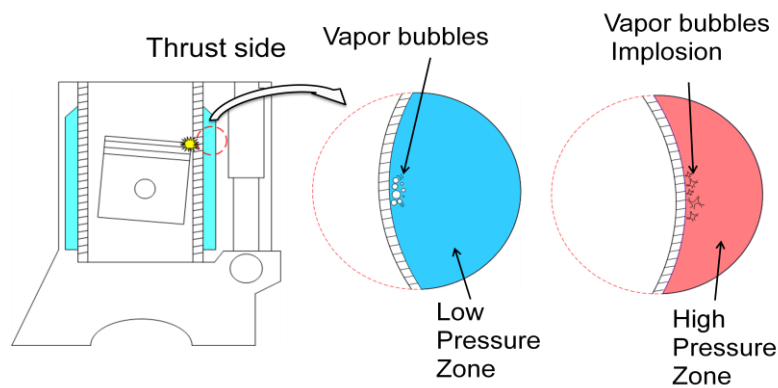


Fig.1.5 Liner vibration and cavitation in the coolant

The liner cavitation erosion is initiated by cylinder liner vibration induced by piston slap force. When the cylinder wall vibrates seriously, the coolant cannot follow the rapid motion of the liner wall. As shown in Fig.1.5, vapor bubbles are created due to an instantaneous low pressure in the coolant as the liner moves away from the coolant. Immediately after the formation of vapor bubbles, the liner surface moves reversely to create a localized high pressure in the coolant and cause the vapor bubbles to collapse. The impact which causes the most serious liner vibration occurs just after the combustion top dead center with maximum cylinder pressure. The magnitude of piston slap force is related to the clearance between piston skirt and liner wall, which explains some engines with an increase of clearance resulting from liner wear, or piston scuffing after a considerable period of operation, may develop water-side erosion.

This case by case variation of cavitation erosion makes it difficult to estimate when cavitation occurs. Cavitation erosion of the outside of liners is more rapid than progressive wear of the inside surface by piston ring friction [26]. When a hole completely penetrating the liner wall has developed, the mixture of cooling water and lubricating oil in the combustion chamber causes the failure of engine [24]. An expensive in-frame overhaul is then required to repair the engine. Thus cavitation erosion of liner often seriously reduces the reliability and life expectancy of internal combustion engine and brings expensive down time to change cylinder liners.

Though mechanical components are thought to contribute more to cavitation corrosion [24], chemical and electrochemical actions are also considered to have some influence [27]. T.K.Ross and A.F.Aspin [28] reported several experiments which concerned the influence of vibration on the liquid corrosion of mild steel specimens through electrochemical way. They discussed the contribution of some factors induced by vibration and flow in the coolant such as dissolved oxygen reduction, the influence of heat transfer from the metal to the liquid and the possible increased anodic activity of iron when stressed. The conclusion can be drawn that vibration itself does increase the corrosion but the stress in mild steel induced by vibration does not contribute to the increase of corrosion rate. Heat transfer from steel surface is affected by both flow and vibration and increases the corrosion rate.

(1) Coolant condition

Anything done to reduce liner vibration also reduces liner pitting. When liner vibration is at normal levels, liner pitting can be adequately controlled by the proper choice of coolant additive. Coolant for heavy duty engine usually consists of water, antifreeze and supplemental coolant additives (SCAs). Water is the heat conducting medium and the liquor for antifreeze and SCAs. Antifreeze is designed to prevent freeze and boil over and SCAs are used for

protection against deposits, corrosion and pitting. In mid 1950's it was found cylinder liner cavitation pitting could be controlled through proper addition of chromate to the engine coolant. Later, chromate was displaced by nitrites for liner cavitation control as the toxicity of chromates becomes apparent [25]. Later, more environment friendly antifreeze containing nitrite was invented, which used chemicals to plate sleeves with a thin protective layer [29]. For most engines, generous use of SCAs adequately controlled pitting. In 1980s, the problems of overtreatment such as silicate gelation [30], water pump seal seepage [31] and solder corrosion [32] raised the awareness that not only undertreatment but also overtreatment was undesirable. The geometry of the water coolant passage at the thrust side of liner that are most injured by pitting is also an important factor. Generally, the less the width of the coolant passage, the greater the pitting without considering other factors [27][33]. The pitting on liners is caused by the formation and collapse of bubbles. Temperature and pressure of coolant at the thrust side of liner directly determine the environment of creation and implosion of bubble. Nonlinear effects of temperature and pressure are examined by laboratory tests using a vibrating cast iron specimen in coolant [34]. The judgment of the occurrence of cavitation bubbles can be expressed mathematically by the equation

$$K = \frac{P_w - P_v}{\rho v^2 / 2g} \quad (1.3)$$

where, K is cavitation number, P_w is pressure at the cylinder wall, P_v is vapor pressure of the coolant, ρ is fluid density, v is fluid velocity and g is gravitational constant. When the cavitation number becomes zero or less, the boiling point has been reached, cavitation will begin to occur. Preventing the formation of cavitation bubbles, the pressure of coolant near cylinder wall (P_w) should be made as large as possible and vapor pressure (P_v) should be made as small as possible. The higher the temperature, the higher the vapor pressure will be, therefore lowering P_v can be achieved by lowering the coolant temperature. P_w can be increased by directly raising the head pressure. The summation of coolant pressure, vibration pressure P_w

and vapor pressure P_v should always be greater than zero to prevent generation of cavitation. An engine operating at atmospheric pressure will be much more prone to cavitation than a cooling system with a pressure cap of 1.72atm or more [35].

R.D. Hercamp and R.D. Hudgens [25] reported a cavitation erosion bench test which was used for evaluating the performance of coolant in protecting cast iron cylinder liners against cavitation erosion. The bench test showed that extensive pitting appeared on cylinders with coolant of mixture of antifreeze and tap water. While under the same engine test procedure but using mixture of antifreeze, tap water and SCA, there was no liner pitting for any cylinders. Chemical corrosion had little effect on forming the honeycombed structure of the eroded surface [24]. To search the main reason of liner cavitation, Yu Kang Zhou and Jiu Gen He [24] carried out experiments of metallographic comparisons between vibratory cavitation specimens of cast iron and a real damaged liner. Results show that the appearance of the damaged liner is similar to that of the vibratory specimen. On the other hand, a corrosion test of specimens of the same material was performed. Material was removed evenly from the surface, which is different from the cavitation damage.

(2) Liner material

The corrosion resistance and strength of liner outside surface affect the performance of pitting. The ultimate resilience of materials has been found in bench tests to relate closely with cavitation resistance [36~38]. Because of the versatility and high cost performance ratio, cast irons are widely used in the manufacture of hydraulic machinery. Particularly, diesel engine cylinder liners are almost all manufactured from flake graphite grey irons. The erosion of the flake graphite cast irons is relatively severe because of the large volume of the matrix intersected by the weak graphite flakes, which acted as stress concentrators and cut through the matrix [39~47]. Cavitation erosion in distilled water is considered to be predominantly

mechanical in nature [48], which is related to the mechanical properties of the material and generally the ultimate resilience and the Brinell hardness are most relevant. The largest weakening effect of graphite occurred with plate-like graphite, followed by flake graphite and then by spheroidal graphite. Spheroidal graphite grey irons are most likely to erosion because of the influence of matrix. The contribution of the matrix to erosion strength decreased in the order of brinite, tempered martensite, fine ferrite-carbide mixture, pearlite, martensite and finally as-cast containing free ferrite [47]. Small amounts of silicon increase the cavitation erosion resistance [43], while small amounts of chromium or molybdenum decrease the resistance [49]. Laser surface melting can increase the cavitation erosion resistance of cast irons by eliminating graphite flakes and refining the microstructure. Diffusion coatings increase considerably the resistance of cast irons to cavitation attack [50] [51]. Improvement can be made on microstructure of cast iron to reduce cavitation erosion attack. Outside diameter coating have also been evaluated, such as chrome which has been reported to be helpful to prevent cavitation [52] [53].

(3) Piston slap induced liner cavitation

As the liner cavitation is initiated and exaggerated by piston slap induced liner vibration, the vibration of cylinder wall under the action of piston slap force is crucial to this problem. Endo and Ikenouchi [54] examined the dynamical deformation of the cylinder of a two cycle marine use engine with bore of 280mm in running conditions. It was found that the pitting damage distribution on the cylinder surface of cooling water side favorably correspond to the cylindrical mode of vibration with two nodal point in its circumference which was excited by the impact force acting on the cylinder from moving piston. Using a 350mm bore two stroke marine use diesel engine, Endo and Ikenouchi [55] measured the cylinder liner dynamic behaviors in more details from the viewpoint of cavitation erosion. In the experiment, the

cylinder liner deflection caused by piston slap impact force showed the value more than 0.1mm at each cycle, and this deflection was followed by cylinder vibration which caused the pressure fluctuation of water coolant largely enough to initiate cavitation. Cavity motion was observed directly to verify the estimation. Test results showed that if the vibration amplitude is kept within 0.04mm, cylinder liners will be successfully prevented from cavitation erosion. Addition of soluble oil to coolant was found to have remarkable effect on the reduction of cavitation erosion due to the variation of surface tension of water by the addition of soluble oil.

Yonezawa et al. regarded piston slap induced liner vibration as the major reason of liner cavitation [56]. They studied the mechanism of piston slap by introducing oil film between piston and liner and tracking transient response of liner through FEM models of cylinder liner and cylinder block [57]. In circumferential direction, the biggest liner vibration appeared at thrust side which is nearly two times than that of anti thrust side. In vertical direction, the biggest liner vibration appears at liner center when piston goes down [58]. In order to study the relationship between liner vibration and the generation of bubbles, test equipment was established to simulate piston slap process of diesel engine as shown in Fig.1.6. The behavior of cavitation bubbles was observed continuously by taking microscopic photographs under different rotating speed. As the vibration increased, vaporous bubbles were generated, which would bring impingement during the transient collapsing after life time of 150 μ s. Eq.(1.4) described the relation between liner vibration and pressure fluctuation, which was concluded from the experimental results with rotating speed changing from 200RPM to 1100RPM [59].

$$\Delta P_w = \alpha \cdot \rho \cdot C \cdot V_1 \quad (1.4)$$

where, α is attenuation coefficient, ρ is the density of coolant, C is the sound speed of coolant and V_1 is the velocity of liner vibration. As shown in Eq.(1.3), pressure at cylinder wall P_w equals standard atmospheric pressure minus liner vibration induced pressure fluctuation ($P_{ST} - \Delta P_w$). The criterion of cavitation generation can be concluded as shown in

Eq.(1.5).

$$P_v \geq P_{ST} - \Delta P_w \quad (1.5)$$

The influence of the width of water coolant passage near the wet surface of cylinder liner was investigated by changing the distance h between liner wall and testing plate as shown in Fig.1.6. The results showed that smaller h would bring more cavitation bubbles [60]. The relationship between pressure fluctuation and cavitation characteristics such as the bubble quantity, distribution, average diameter, duration time and volume of bubbles and was also investigated [61] [62].

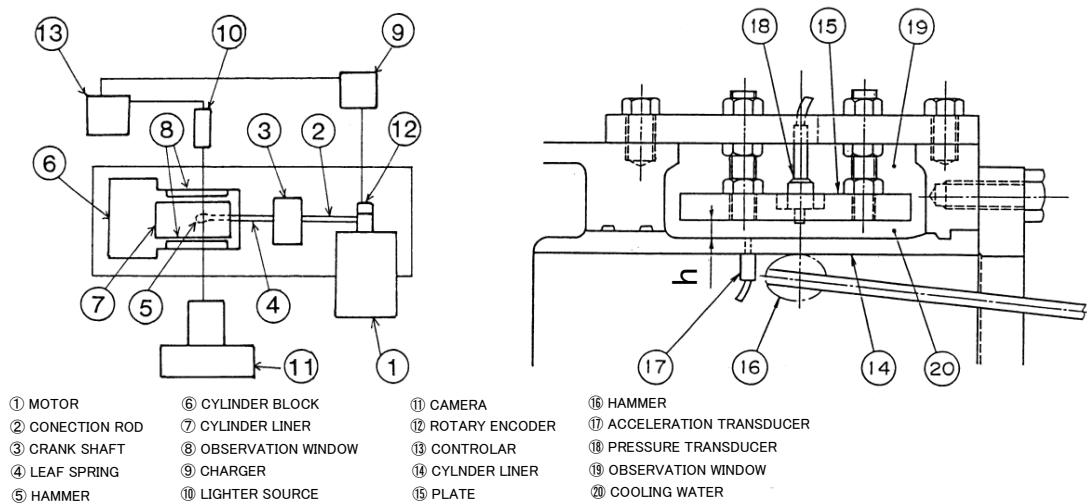


Fig.1.6 Experiment of observing cavitation bubbles under piston slap forces [59]

The research of liner cavitation until now concentrates more on the piston slap force and the subsequent liner vibration. Efforts are made to reduce engine noise, piston scuffing and liner vibration by modifying piston profile, offset and clearance. Liner coating and SCA as practical applications are preferred in practical problems. However, few researches have been done with respect to the vibration characteristics of acoustic field of water coolant passage in the structural-acoustic coupled system of crankcase and water coolant.

1.4 Objective of this research and topics of discussion

Analytical method to predict the water pressure fluctuation in the water coolant passage is required to discuss the occurrence of liner cavitation and protection of cavitation erosion. This research aims to develop the numerical procedure to predict the water pressure fluctuation induced by engine exciting forces like combustion pressure, piston slap, main bearing impact and gear impact at the engine operating condition.

In chapter 2, numerical model of water acoustic field is incorporated into the equation of motion of the coupled vibration of the total engine system, considering the rotating shaft and fuel injection force, to evaluate the effect of engine exciting forces other than piston slap on the water pressure fluctuation.

In chapter 3, the experiment of rectangular tank model filled with water inside is carried out to evaluate the validity of this numerical procedure. Dynamic water pressure and structural vibration excited by impact force acting on the structure are measured and compared with the calculated results. In the rectangular tank model experiment, cavitation occurrence criteria that cavitation is generated when the water pressure fluctuation decreases to the vapor pressure or less is discussed and confirmed.

In chapter 4, dynamic response of actual engine structure and water pressure in the water coolant passage induced by piston slap force are calculated considering the vibratory characteristics of crankcase and acoustic characteristics of water coolant passage. As the speed of sound in water changes with the small content of air bubble, natural frequencies of the water acoustic field vary and coupled mode shapes of structure and water acoustic field changes. The effects of the proximity of natural frequency between structural vibration and water acoustic field are discussed and moreover the effect of mode shape of piston slap impact point is examined.

In chapter 5, summary and conclusion are drawn of this doctoral thesis.

Chapter 2

NUMERICAL METHOD TO PREDICT WATER PRESSURE FLUCTUATION CONSIDERING DYNAMIC CHARACTERISTICS OF ENGINE STRUCTURE AND WATER ACOUSTIC FIELD

In this chapter, FEM (finite element method) formulation of equation of motion for coupled acoustic vibration between fluid and structure is proposed considering the coupling effect on the boundary. The unsymmetrical coupled equation is then diagonalized by left and right eigenvectors. The diagonalized equation of motion of engine block and water coolant passage coupled system is then substituted into the equation of motion of assembled engine system containing piston, connecting rod, crankcase, cylinder head, rotating crank shafts and meshing gear trains with external forces such as combustion pressure, piston slap force acting on cylinder liner, fuel injection pressure, opening and closing force of the valve system, meshing force of gear train and reaction force of engine mount.

Nomenclature

0	Index indicates Engine block
1	Index indicates Crank shaft
2	Index indicates Intermediate gear
3	Index indicates Injection pump
4	Index indicates Intake and exhaust valve train
A	Index indicates Acoustic field
0A	Index indicates Coupled system between engine block and water coolant passage
C_A	Damping matrix of acoustic field
\tilde{C}_A	Modal damping matrix of acoustic field
C_{ij}^G	Damping matrix of meshing between gear i and gear j

\mathbf{C}_S	Damping matrix of structure
$\tilde{\mathbf{C}}_S$	Modal damping matrix of structure
$\Delta\mathbf{C}$	Damping matrix caused by Coriolis force in rotational coordinate system
\mathbf{F}'_{B1}	Reaction force from crank shaft
\mathbf{F}'_{B2}	Reaction force from intermediate gear shaft
\mathbf{F}'_{B3}	Reaction force from injection pump shaft
\mathbf{F}'_{B4}	Reaction force from valve train shaft
\mathbf{F}_C	Gas force acting on crank pin and inertial force of piston and con-rod
\mathbf{F}_{C0}	Reaction force from valve train
\mathbf{F}_{c3}	Force from injection pump acting on cam
\mathbf{F}_{c4}	Force from valve trains acting on cam
\mathbf{F}_{E0}	Reaction force from engine mount
\mathbf{F}_{G0}	Gas force
\mathbf{F}_{I0}	Reaction force from injection pressure
\mathbf{F}_M	Centrifugal force of crank shaft
\mathbf{F}_{S0}	Piston slap force
\mathbf{K}_A	Stiffness matrix of acoustic field
$\tilde{\mathbf{K}}_A$	Modal stiffness matrix of acoustic field
\mathbf{K}_E	Stiffness of mounting part of engine block
\mathbf{K}_{ij}^B	Stiffness matrix of bearing between structure i and structure j
\mathbf{K}_{ij}^G	Stiffness matrix of meshing between gear i and gear j
\mathbf{K}_m	Stiffness matrix of structure m
\mathbf{K}_S	Stiffness matrix of structure
$\tilde{\mathbf{K}}_S$	Modal stiffness matrix of structure
$\Delta\mathbf{K}$	Stiffness matrix caused by Coriolis force in rotary coordinate system

- \mathbf{M}_A Mass matrix of acoustic field
- $\tilde{\mathbf{M}}_A$ Modal mass matrix of acoustic field
- \mathbf{M}_m Mass matrix of structure m of engine
- \mathbf{M}_S Mass matrix of structure
- $\tilde{\mathbf{M}}_S$ Modal mass matrix of structure
- \mathbf{P} Pressure fluctuation of water coolant passage
- \mathbf{S} Matrix of element area at the boundary of fluid and structure
- S Index indicates Structure

2.1 FEM formulation of dynamic response of engine structure and water acoustic field in water coolant passage

If the boundary of structure is not rigid wall but is instead flexible, as shown in Fig.2.1, the acoustic field in the cavity is influenced by the vibration of structure surface and the vibration of structure surface is also excited by the fluid pressure loading.

From Appendix C, the equation of motion of acoustic field with acceleration loading acting on the boundary is given as [63~70]

$$-\omega^2 \mathbf{M}_A \mathbf{p} + j\omega \mathbf{C}_A \mathbf{p} + \mathbf{K}_A \mathbf{p} = \mathbf{S} \mathbf{a}_B \quad (2.1)$$

The equation of motion of structure considering the acoustic loading acting on the boundary can be derived by FEM formulation [70].

$$\begin{aligned} -\omega^2 \mathbf{M}_S \mathbf{x} + j\omega \mathbf{C}_S \mathbf{x} + \mathbf{K}_S \mathbf{x} = \mathbf{f}_0 + \mathbf{f}_B = \mathbf{f}_0 - \mathbf{S} \mathbf{p}_B \\ \mathbf{f}_B = -\mathbf{S} \mathbf{p}_B, \quad \mathbf{S} = \begin{bmatrix} \ddots & & \\ & S_e & \\ & & \ddots \end{bmatrix}, \quad \mathbf{p}_B = \begin{pmatrix} \vdots \\ p_e \mathbf{n}_e \\ \vdots \end{pmatrix} \end{aligned} \quad (2.2)$$

where \mathbf{f}_0 is the external force acting on the structure, \mathbf{f}_B is the force acting on the structure boundary caused by acoustic pressure \mathbf{p}_B , \mathbf{S} is the area matrix and S_e is the area of element e on the boundary, p_e is the pressure corresponding to element e ,

The equation of motion of structure and acoustic field coupled system can be given by Eq.(2.1) and Eq.(2.2),

$$\begin{cases} -\omega^2 \mathbf{M}_S \mathbf{x} + j\omega \mathbf{C}_S \mathbf{x} + \mathbf{K}_S \mathbf{x} = \mathbf{f}_0 + \mathbf{f}_B = \mathbf{f}_0 - \mathbf{S} \mathbf{p}_B \\ -\omega^2 \mathbf{M}_A \mathbf{p} + j\omega \mathbf{C}_A \mathbf{p} + \mathbf{K}_A \mathbf{p} = \mathbf{S} \mathbf{a}_B = -\omega^2 \mathbf{S} \mathbf{x}_B \end{cases} \quad (2.3)$$

2.2 Application of modal analysis technique

(1) Natural frequency and mode shape of structure

The equation of motion of the structure without damping and external force in the frequency domain is described by the following matrix form [71~73].

$$-\omega^2 \mathbf{M}_s \mathbf{x} + \mathbf{K}_s \mathbf{x} = 0 \quad (2.4)$$

The eigenvalue analysis of Eq.(2.4) gives the following solutions:

- | | |
|--|---|
| ω_{Sn} | The n-th natural frequency |
| $\phi_n = (\dots, \phi_{qn}, \dots)^t$ | The n-th vibration mode shape |
| ϕ_{qn} | The n-th vibration mode shape at the q-th degree of freedom |
| $\Phi = [\dots, \phi_n, \dots]$ | The mode shape matrix of vibration |

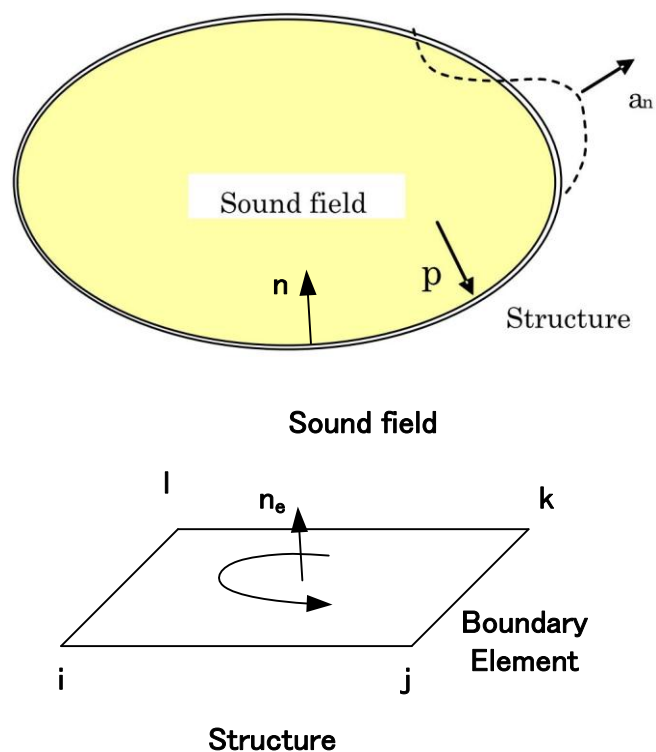


Fig.2.1 Analytical model of structural-acoustic coupled system

$$\tilde{\mathbf{M}}_A = \Psi^t \mathbf{M}_A \Psi = \begin{bmatrix} \ddots & & 0 \\ & \tilde{m}_{An} & \\ 0 & & \ddots \end{bmatrix}, \quad \tilde{m}_{An} = \psi_n^t \mathbf{M}_A \psi_n \quad (2.9)$$

$$\tilde{\mathbf{K}}_A = \Psi^t \mathbf{K}_A \Psi = \begin{bmatrix} \ddots & & 0 \\ & \tilde{k}_{An} & \\ 0 & & \ddots \end{bmatrix}, \quad \tilde{k}_{An} = \tilde{m}_{An} \omega_{An}^2 = \psi_n^t \mathbf{K}_A \psi_n \quad (2.10)$$

The orthogonality condition of damping matrix is assumed as follows:

$$\tilde{\mathbf{C}}_A = \Psi^t \mathbf{C}_A \Psi = \begin{bmatrix} \ddots & & 0 \\ & \tilde{c}_{An} & \\ 0 & & \ddots \end{bmatrix}, \quad \tilde{c}_{An} = 2\zeta_{An} \tilde{m}_{An} \omega_{An} = \psi_n^t \mathbf{C}_A \psi_n \quad (2.11)$$

(3) Dynamic response of structure and acoustic field coupled system

The displacement of the coupled system can be expressed as linear combination of the eigen mode of each system. The displacement of structure vibration is supposed to be \mathbf{x} , which is expressed as liner combination of eigenmode of structure ϕ_i .

$$\mathbf{x} = \sum_i \phi_i a_i = \Phi \mathbf{a} \quad (2.12)$$

Displacement of the boundary \mathbf{x}_B which is normal to the surface is also expressed as follows:

$$\mathbf{x}_B = \begin{pmatrix} \vdots \\ x_{en} \\ \vdots \end{pmatrix} = \sum_i \begin{pmatrix} \vdots \\ \phi_{ei} \cdot \mathbf{n}_e \\ \vdots \end{pmatrix} a_i = \sum_i \begin{pmatrix} \vdots \\ \phi_{en,i} \\ \vdots \end{pmatrix} a_i = \Phi_B \mathbf{a} \quad (2.13)$$

$$\Phi_B = [\cdots \quad \phi_{Bi} \quad \cdots], \quad \phi_{Bi} = \begin{pmatrix} \vdots \\ \phi_{en,i} \\ \vdots \end{pmatrix}, \quad \phi_{en,i} = \phi_{ei} \cdot \mathbf{n}_e \quad (2.14)$$

The pressure of the coupled system \mathbf{p} can be expressed as linear combination of the eigen mode of acoustic field.

$$\mathbf{p} = \sum_i \psi_i \mathbf{b}_i = \Psi \mathbf{b} \quad (2.15)$$

$$\mathbf{p}_B = \begin{pmatrix} \vdots \\ p_e \mathbf{n}_e \\ \vdots \end{pmatrix} = \sum_i \begin{pmatrix} \vdots \\ \psi_{ei} \mathbf{n}_e \\ \vdots \end{pmatrix} \mathbf{b}_i = \Psi_B \mathbf{b} \quad (2.16)$$

$$\Psi_B = [\cdots \quad \Psi_{Bi} \quad \cdots], \quad \Psi_{Bi} = \begin{pmatrix} \vdots \\ \psi_{ei} \mathbf{n}_e \\ \vdots \end{pmatrix} \quad (2.17)$$

where Ψ_B is the mode shape matrix of boundary elements of acoustic field, ψ_{ei} is the mode shape of boundary element e, \mathbf{n}_e is the normal vector of boundary element e. Substituting Eq.(2.12)~Eq.(2.17) into Eq.(2.3), and multiplying Φ and Ψ from left, the equations of coupled motion are given by

$$\begin{cases} -\omega^2 \tilde{\mathbf{M}}_S \mathbf{a} + j\omega \tilde{\mathbf{C}}_S \mathbf{a} + \tilde{\mathbf{K}}_S \mathbf{a} = -\Phi_B^t \mathbf{S} \Psi_B \mathbf{b} + \tilde{\mathbf{f}}_0 \\ -\omega^2 \tilde{\mathbf{M}}_A \mathbf{b} + j\omega \tilde{\mathbf{C}}_A \mathbf{b} + \tilde{\mathbf{K}}_A \mathbf{b} = -\omega^2 \Psi_B^t \mathbf{S} \Phi_B \mathbf{a} \end{cases} \quad (2.18)$$

2.3 Dynamic characteristics of structure and acoustic field coupled system

(1) Natural frequency and mode shape of the coupled system

If the damping matrix and external forces are ignored, Eq.(2.18) becomes

$$\begin{cases} -\omega'^2 \tilde{\mathbf{M}}_S \mathbf{a}' + \tilde{\mathbf{K}}_S \mathbf{a}' + \Phi_B^t \mathbf{S} \Psi_B \mathbf{b}' = 0 \\ -\omega'^2 \tilde{\mathbf{M}}_A \mathbf{b}' + \tilde{\mathbf{K}}_A \mathbf{b}' + \omega'^2 \Psi_B^t \mathbf{S} \Phi_B \mathbf{a}' = 0 \end{cases} \quad (2.19)$$

$$-\omega'^2 \begin{bmatrix} \tilde{\mathbf{M}}_S & 0 \\ -\Psi_B^t \mathbf{S} \Phi_B & \tilde{\mathbf{M}}_A \end{bmatrix} \begin{pmatrix} \mathbf{a}' \\ \mathbf{b}' \end{pmatrix} + \begin{bmatrix} \tilde{\mathbf{K}}_S & \Phi_B^t \mathbf{S} \Psi_B \\ 0 & \tilde{\mathbf{K}}_A \end{bmatrix} \begin{pmatrix} \mathbf{a}' \\ \mathbf{b}' \end{pmatrix} = 0 \quad (2.20)$$

Solving the characteristic equation of the system as expressed in Eq.(2.20), the natural

frequencies ω'_n and corresponding eigenvectors $\begin{pmatrix} \mathbf{a}'_n \\ \mathbf{b}'_n \end{pmatrix}$ are obtained, where \mathbf{a}'_n and \mathbf{b}'_n

stand for the structural and acoustic components of the eigenvector respectively. The vibration mode shape of structure and acoustic field of coupled system are written by the following

equations:

$$\begin{aligned}\phi'_n &= \Phi \mathbf{a}'_n = \sum_r \phi_r \mathbf{a}'_{r,n} \\ \psi'_n &= \Psi \mathbf{b}'_n = \sum_r \psi_r \mathbf{b}'_{r,n}\end{aligned}\tag{2.21}$$

Since the mass and stiffness matrices in Eq.(2.20) are not symmetrical, the conventional mode-superposition method cannot be applied to the coupled system to orthogonalize the mass and stiffness matrix. For this reason, the so-called left eigenvectors is imported for diagonalization of mass and stiffness matrix [74].

The left eigenvector is defined to yield the following equation.

$$\begin{pmatrix} \mathbf{c}_i^t & \mathbf{d}_i^t \end{pmatrix} \left(-\omega_i'^2 \begin{bmatrix} \tilde{\mathbf{M}}_S & 0 \\ -\Psi_B^t \mathbf{S} \Phi_B & \tilde{\mathbf{M}}_A \end{bmatrix} + \begin{bmatrix} \tilde{\mathbf{K}}_S & \Phi_B^t \mathbf{S} \Psi_B \\ 0 & \tilde{\mathbf{K}}_A \end{bmatrix} \right) = 0\tag{2.22}$$

As has been proofed in Appendix A, left eigenvector becomes

$$\begin{pmatrix} \mathbf{c}_i^t & \mathbf{d}_i^t \end{pmatrix} = \begin{pmatrix} \mathbf{a}_i'^t & \frac{1}{\omega_i'^2} \mathbf{b}_i'^t \end{pmatrix}\tag{2.23}$$

The n-th right eigenvector $\begin{pmatrix} \mathbf{a}'_n \\ \mathbf{b}'_n \end{pmatrix}$ yields

$$-\omega_n'^2 \begin{bmatrix} \tilde{\mathbf{M}}_S & 0 \\ -\Psi_B^t \mathbf{S} \Phi_B & \tilde{\mathbf{M}}_A \end{bmatrix} \begin{pmatrix} \mathbf{a}'_n \\ \mathbf{b}'_n \end{pmatrix} + \begin{bmatrix} \tilde{\mathbf{K}}_S & \Phi_B^t \mathbf{S} \Psi_B \\ 0 & \tilde{\mathbf{K}}_A \end{bmatrix} \begin{pmatrix} \mathbf{a}'_n \\ \mathbf{b}'_n \end{pmatrix} = 0\tag{2.24}$$

Multiplying the r-th left eigenvector $\begin{pmatrix} \mathbf{a}_r'^t & \frac{1}{\omega_r'^2} \mathbf{b}_r'^t \end{pmatrix}$ from the left side, one can obtain

$$\begin{pmatrix} \mathbf{a}_r'^t & \frac{1}{\omega_r'^2} \mathbf{b}_r'^t \end{pmatrix} \left\{ -\omega_n'^2 \begin{bmatrix} \tilde{\mathbf{M}}_S & 0 \\ -\Psi_B^t \mathbf{S} \Phi_B & \tilde{\mathbf{M}}_A \end{bmatrix} + \begin{bmatrix} \tilde{\mathbf{K}}_S & \Phi_B^t \mathbf{S} \Psi_B \\ 0 & \tilde{\mathbf{K}}_A \end{bmatrix} \right\} \begin{pmatrix} \mathbf{a}'_n \\ \mathbf{b}'_n \end{pmatrix} = 0\tag{2.25}$$

The r-th left eigenvector $\begin{pmatrix} \mathbf{a}_r'^t & \frac{1}{\omega_r'^2} \mathbf{b}_r'^t \end{pmatrix}$ yields

$$\begin{pmatrix} \mathbf{a}_r^t & \frac{1}{\omega_r'^2} \mathbf{b}_r^t \end{pmatrix} \left(-\omega_r'^2 \begin{bmatrix} \tilde{\mathbf{M}}_S & 0 \\ -\Psi_B^t \mathbf{S} \Phi_B & \tilde{\mathbf{M}}_A \end{bmatrix} + \begin{bmatrix} \tilde{\mathbf{K}}_S & \Phi_B^t \mathbf{S} \Psi_B \\ 0 & \tilde{\mathbf{K}}_A \end{bmatrix} \right) = 0 \quad (2.26)$$

Multiplying the right eigenvector $\begin{pmatrix} \mathbf{a}'_n \\ \mathbf{b}'_n \end{pmatrix}$ from the right side, the following equation is obtained

$$\begin{pmatrix} \mathbf{a}_r^t & \frac{1}{\omega_r'^2} \mathbf{b}_r^t \end{pmatrix} \left(-\omega_r'^2 \begin{bmatrix} \tilde{\mathbf{M}}_S & 0 \\ -\Psi_B^t \mathbf{S} \Phi_B & \tilde{\mathbf{M}}_A \end{bmatrix} + \begin{bmatrix} \tilde{\mathbf{K}}_S & \Phi_B^t \mathbf{S} \Psi_B \\ 0 & \tilde{\mathbf{K}}_A \end{bmatrix} \right) \begin{pmatrix} \mathbf{a}'_n \\ \mathbf{b}'_n \end{pmatrix} = 0 \quad (2.27)$$

Subtracting Eq.(2.25) from Eq.(2.27) becomes

$$(\omega_r'^2 - \omega_n'^2) \begin{pmatrix} \mathbf{a}_r^t & \frac{1}{\omega_r'^2} \mathbf{b}_r^t \end{pmatrix} \begin{bmatrix} \tilde{\mathbf{M}}_S & 0 \\ -\Psi_B^t \mathbf{S} \Phi_B & \tilde{\mathbf{M}}_A \end{bmatrix} \begin{pmatrix} \mathbf{a}'_n \\ \mathbf{b}'_n \end{pmatrix} = 0 \quad (2.28)$$

Since $\omega_r'^2 \neq \omega_n'^2$, Eq.(2.28) suggests that

$$\begin{pmatrix} \mathbf{a}_r^t & \frac{1}{\omega_r'^2} \mathbf{b}_r^t \end{pmatrix} \begin{bmatrix} \tilde{\mathbf{M}}_S & 0 \\ -\Psi_B^t \mathbf{S} \Phi_B & \tilde{\mathbf{M}}_A \end{bmatrix} \begin{pmatrix} \mathbf{a}'_n \\ \mathbf{b}'_n \end{pmatrix} = 0 \quad (2.29)$$

Similarly,

$$\begin{pmatrix} \mathbf{a}_r^t & \frac{1}{\omega_r'^2} \mathbf{b}_r^t \end{pmatrix} \begin{bmatrix} \tilde{\mathbf{K}}_S & \Phi_B^t \mathbf{S} \Psi_B \\ 0 & \tilde{\mathbf{K}}_A \end{bmatrix} \begin{pmatrix} \mathbf{a}'_n \\ \mathbf{b}'_n \end{pmatrix} = 0 \quad (2.30)$$

Supposing the right and left eigenvector matrices to be \mathbf{A} and $\mathbf{\Lambda}^t$ as shown in Eq.(2.31), the orthogonality condition of mass and stiffness matrix of the coupled system can be summarized as Eq.(2.32) and Eq.(2.33).

$$\mathbf{A} = [\cdots \quad \boldsymbol{\alpha}_n \quad \cdots], \quad \boldsymbol{\alpha}_n = \begin{pmatrix} \mathbf{a}'_n \\ \mathbf{b}'_n \end{pmatrix}, \quad \mathbf{\Lambda}^t = \begin{bmatrix} \vdots \\ \boldsymbol{\beta}_r^t \\ \vdots \end{bmatrix}, \quad \boldsymbol{\beta}_r^t = \begin{pmatrix} \mathbf{a}_r^t & \frac{1}{\omega_r'^2} \mathbf{b}_r^t \end{pmatrix} \quad (2.31)$$

$$\Lambda^t \begin{bmatrix} \tilde{\mathbf{M}}_S & 0 \\ -\Psi_B^t \mathbf{S} \Phi_B & \tilde{\mathbf{M}}_A \end{bmatrix} \mathbf{A} = \begin{bmatrix} \ddots & & 0 \\ & \tilde{M}_n & \\ 0 & & \ddots \end{bmatrix} = \tilde{\mathbf{M}} \quad (2.32)$$

$$\text{where, } \tilde{M}_n = (\mathbf{a}_n^t, \frac{1}{\omega_n'^2} \mathbf{b}_n^t) \begin{bmatrix} \tilde{\mathbf{M}}_S & 0 \\ -\Psi_B^t \mathbf{S} \Phi_B & \tilde{\mathbf{M}}_A \end{bmatrix} \begin{pmatrix} \mathbf{a}'_n \\ \mathbf{b}'_n \end{pmatrix}$$

$$\Lambda^t \begin{bmatrix} \tilde{\mathbf{K}}_S & \Phi_B^t \mathbf{S} \Psi_B \\ 0 & \tilde{\mathbf{K}}_A \end{bmatrix} \mathbf{A} = \begin{bmatrix} \ddots & & 0 \\ & \tilde{M}_n \omega_n'^2 & \\ 0 & & \ddots \end{bmatrix} = \tilde{\mathbf{K}} \quad (2.33)$$

$$\text{where, } \tilde{M}_n \omega_n'^2 = (\mathbf{a}_n^t, \frac{1}{\omega_n'^2} \mathbf{b}_n^t) \begin{bmatrix} \tilde{\mathbf{K}}_S & \Phi_B^t \mathbf{S} \Psi_B \\ 0 & \tilde{\mathbf{K}}_A \end{bmatrix} \begin{pmatrix} \mathbf{a}'_n \\ \mathbf{b}'_n \end{pmatrix}$$

Presented by the coupled mode shape Φ' and Ψ' , the orthogonal conditions can be expressed as

$$\begin{aligned} [(\Phi')^t \quad \Omega(\Psi')^t] \begin{bmatrix} \mathbf{M}_S & 0 \\ -\mathbf{S} & \mathbf{M}_A \end{bmatrix} \begin{bmatrix} \Phi' \\ \Psi' \end{bmatrix} &= \begin{bmatrix} \ddots & & 0 \\ & \tilde{M}_n & \\ 0 & & \ddots \end{bmatrix} = \tilde{\mathbf{M}} \\ [(\Phi')^t \quad \Omega(\Psi')^t] \begin{bmatrix} \mathbf{K}_S & \mathbf{S} \\ 0 & \mathbf{K}_A \end{bmatrix} \begin{bmatrix} \Phi' \\ \Psi' \end{bmatrix} &= \begin{bmatrix} \ddots & & 0 \\ & \tilde{M}_n \omega_n'^2 & \\ 0 & & \ddots \end{bmatrix} = \tilde{\mathbf{K}} \end{aligned} \quad (2.34)$$

where

$$\Phi' = [\dots \quad \phi'_n \quad \dots], \quad \Psi' = [\dots \quad \psi'_n \quad \dots], \quad \Omega = \begin{bmatrix} \ddots & & 0 \\ & \frac{1}{\omega_n'^2} & \\ 0 & & \ddots \end{bmatrix} \quad (2.35)$$

(2) Dynamic response of coupled system

When exciting force $\mathbf{f} = \mathbf{f}_0 e^{j\omega t}$ acts on the structure, the equation of motion of the coupled system is

$$-\omega^2 \begin{bmatrix} \tilde{\mathbf{M}}_S & 0 \\ -\Psi_B^t \mathbf{S} \Phi_B & \tilde{\mathbf{M}}_A \end{bmatrix} \begin{pmatrix} \mathbf{a} \\ \mathbf{b} \end{pmatrix} + j\omega \begin{bmatrix} \tilde{\mathbf{C}}_S & 0 \\ 0 & \tilde{\mathbf{C}}_A \end{bmatrix} \begin{pmatrix} \mathbf{a} \\ \mathbf{b} \end{pmatrix} + \begin{bmatrix} \tilde{\mathbf{K}}_S & \Phi_B^t \mathbf{S} \Psi_B \\ 0 & \tilde{\mathbf{K}}_A \end{bmatrix} \begin{pmatrix} \mathbf{a} \\ \mathbf{b} \end{pmatrix} = \begin{pmatrix} \tilde{\mathbf{f}}_0 \\ 0 \end{pmatrix} \quad (2.36)$$

$$\tilde{\mathbf{f}}_0 = \mathbf{\Phi}^t \mathbf{f}_0 = (\dots \tilde{f}_n \dots)^t = \left(\dots \sum_q f_q \phi_{q,n} \dots \right)^t$$

where q is the excitation point of the structure, n is the mode number of the structure. The mode response of the coupled system can be expressed as the liner combination of eigenmodes of the coupled system.

$$\begin{pmatrix} \mathbf{a} \\ \mathbf{b} \end{pmatrix} = \sum_n \begin{pmatrix} \mathbf{a}'_n \\ \mathbf{b}'_n \end{pmatrix} u_n = \sum_n \boldsymbol{\alpha}_n u_n = \mathbf{A} \mathbf{u} \quad (2.37)$$

Substituting Eq.(2.37) into Eq.(2.36) and multiplying $\mathbf{\Lambda}^t$ from the left side yields

$$-\omega^2 \tilde{\mathbf{M}} \mathbf{u} + j\omega \tilde{\mathbf{C}} \mathbf{u} + \tilde{\mathbf{K}} \mathbf{u} = \begin{pmatrix} \tilde{\mathbf{f}}_0 \\ 0 \end{pmatrix} \quad (2.38)$$

The orthogonality condition of the damping matrix is assumed to be Eq.(2.39).

$$\tilde{\mathbf{C}} = \mathbf{\Lambda}^t \begin{bmatrix} \tilde{\mathbf{C}}_S & \mathbf{0} \\ \mathbf{0} & \tilde{\mathbf{D}}_A \end{bmatrix} \mathbf{A} \approx \begin{bmatrix} \ddots & & 0 \\ & 2\zeta_n \omega_n \tilde{M}_n & \\ 0 & & \ddots \end{bmatrix} \quad (2.39)$$

The dynamic response of the n-th mode of coupled system in the frequency domain can be given by Eq.(2.40).

$$u_n = \frac{\tilde{f}'_n}{\tilde{M}_n (-\omega^2 + \omega_n'^2 + 2j\zeta_n \omega \omega_n')} = \frac{\sum_m a'_{n,m} \left(\sum_q f_q \phi_{q,m} \right)}{\tilde{M}_n (-\omega^2 + \omega_n'^2 + 2j\zeta_n \omega \omega_n')} \quad (2.40)$$

where n is the mode number of coupled system, m is the uncoupled mode number of the structure. The acceleration $\ddot{\mathbf{x}}$ and pressure \mathbf{p} of the coupled system are

$$\begin{aligned} \ddot{\mathbf{x}} &= \sum_n -\omega_n'^2 \boldsymbol{\phi}'_n u_n = \sum_n -\omega_n'^2 (\mathbf{\Phi} \mathbf{a}'_n) u_n = \sum_n -\omega_n'^2 \left(\sum_{r_1} \phi_{q_a, r_1} a'_{n, r_1} \right) u_n \\ &= \sum_n \frac{-\omega_n'^2 \left(\sum_{r_1} \phi_{q_a, r_1} a'_{n, r_1} \right) \left(\sum_{r_1} a'_{n, r_1} \left(\sum_{q_e} f_{q_e} \phi_{q_e, r_1} \right) \right)}{\tilde{M}_n (-\omega^2 + \omega_n'^2 + 2j\zeta_n \omega \omega_n')} \end{aligned} \quad (2.41)$$

$$\begin{aligned}
\mathbf{p} &= \sum_n \boldsymbol{\psi}'_n u_n = \sum_n (\boldsymbol{\Psi} \mathbf{b}'_n) u_n = \sum_n \left(\sum_{r_2} \boldsymbol{\psi}_{q_p, r_2} b'_{n, r_2} \right) u_n \\
&= \sum_n \frac{\left(\sum_{r_2} \boldsymbol{\psi}_{q_p, r_2} b'_{n, r_2} \right) \left(\sum_{r_2} \mathbf{a}'_{n, r_2} \left(\sum_{q_e} f_{q_e} \phi_{q, r_2} \right) \right)}{\tilde{M}_n (-\omega^2 + \omega_n'^2 + 2j\zeta_n \omega \omega_n')}
\end{aligned} \tag{2.42}$$

where q_e is the excitation point, q_a is the response point of acceleration, q_p is the response point of pressure, r_1 is the order of coordinate in \mathbf{a}'_n , r_2 is the order of coordinate in \mathbf{b}'_n .

2.4 Dynamic response of total engine system in running condition

The equation of motion of total engine system considering water coolant passage and rotating shafts is derived. Figure 2.2 shows the engine block model which is composed of cylinder head, crankcase, front plate, gear casing and injection pump. The engine block is subject to different exciting forces such as combustion pressure, piston slap force acting on cylinder liner, fuel injection pressure, opening and closing force of the valve system, meshing force of gear train and reaction force of engine mount as shown in Fig.2.3. Fig.2.4 shows the analytical model of total engine system which contains water coolant passage and rotating shafts.

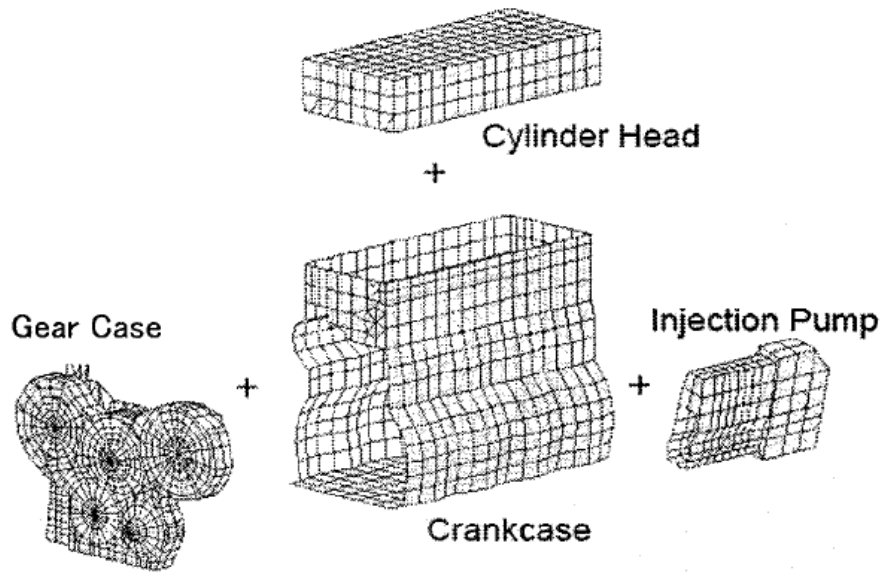


Fig.2.2 Components of engine block

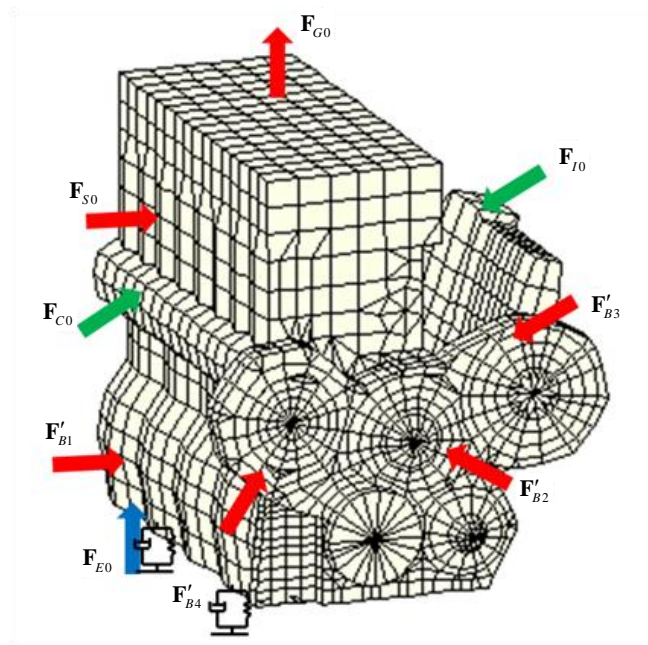


Fig.2.3 External forces acting on engine structure

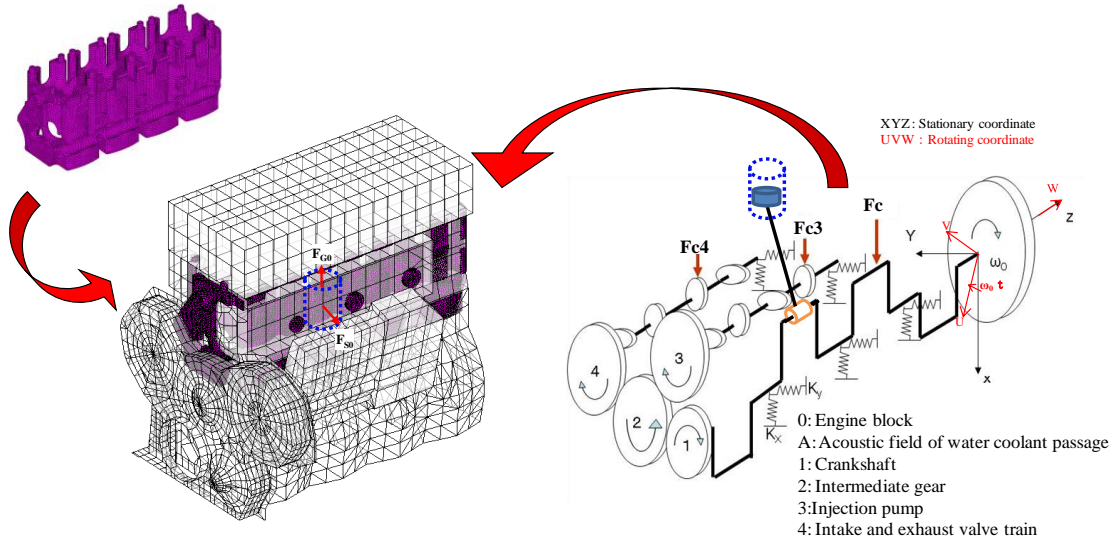


Fig.2.4 Analytical model of total engine system considering water coolant passage and rotating shafts

The equation of motion of coupled system of engine block and water coolant passage is given by the following equation [75]:

$$\begin{bmatrix} \mathbf{M}_0 & 0 \\ -\mathbf{S} & \mathbf{M}_A \end{bmatrix} \begin{bmatrix} \ddot{\mathbf{x}}_0 \\ \ddot{\mathbf{p}} \end{bmatrix} + \begin{bmatrix} \mathbf{C}_0 & 0 \\ 0 & \mathbf{D}_A \end{bmatrix} \begin{bmatrix} \dot{\mathbf{x}}_0 \\ \dot{\mathbf{p}} \end{bmatrix} + \begin{bmatrix} \mathbf{K}_0 & \mathbf{S} \\ 0 & \mathbf{K}_A \end{bmatrix} \begin{bmatrix} \mathbf{x}_0 \\ \mathbf{p} \end{bmatrix} = \begin{bmatrix} \mathbf{f}_0 \\ 0 \end{bmatrix} \quad (2.43)$$

where

$$\mathbf{f}_0 = \mathbf{F}'_{B1} + \mathbf{F}'_{B2} + \mathbf{F}'_{B3} + \mathbf{F}'_{B4} + \mathbf{F}'_{S0} + \mathbf{F}'_{G0} + \mathbf{F}'_{E0} + \mathbf{F}'_{I0} + \mathbf{F}'_{C0}$$

The displacement of engine block \mathbf{x}_0 and pressure \mathbf{p} are expressed by linear combination of mode shapes of coupled system :

$$\begin{bmatrix} \mathbf{x}_0 \\ \mathbf{p} \end{bmatrix} = \sum_{n=1}^{n_S+n_A} \begin{bmatrix} \phi'_{0n} \\ \psi'_{0n} \end{bmatrix} a_{0n} = \begin{bmatrix} \Phi'_0 \\ \Psi'_0 \end{bmatrix} \mathbf{a}_0 \quad (2.44)$$

Substituting Eq.(2.44) into Eq.(2.43) and multiplying the eigenvector $\begin{bmatrix} (\Phi'_0)^t & \Omega(\Psi'_0)^t \end{bmatrix}$ from left side, one can obtain the equation of motion of engine block and water acoustic field coupled system expressed by modal coordinates:

$$\tilde{\mathbf{M}}_{0A} \ddot{\mathbf{a}}_0 + \tilde{\mathbf{C}}_{0A} \dot{\mathbf{a}}_0 + \tilde{\mathbf{K}}_{0A} \mathbf{a}_0 = \begin{bmatrix} (\Phi'_0)^t & \Omega(\Psi'_0)^t \end{bmatrix} \begin{bmatrix} \mathbf{f}_0 \\ 0 \end{bmatrix} = (\Phi'_0)^t \mathbf{f}_0 = \begin{bmatrix} \vdots \\ (\phi'_{0n})^t \mathbf{f}_0 \\ \vdots \end{bmatrix} \quad (2.45)$$

Eq.(2.45) is the orthogonalized equation of motion of coupled system between engine

block and water coolant passage, which is a part of the equation of motion of the engine total system considering the acoustic characteristics of water coolant passage. The equation of motion of total engine system is described in the reference [75][76],

$$\mathbf{M}\ddot{\mathbf{x}} + \mathbf{C}\dot{\mathbf{x}} + \mathbf{K}\mathbf{x} = \mathbf{F} \quad (2.46)$$

where

$$\mathbf{x} = (\mathbf{x}_0, \mathbf{p}, \mathbf{u}_1, \mathbf{x}_2, \mathbf{x}_3, \mathbf{x}_4)^t$$

$$\begin{aligned}
\mathbf{M} &= \begin{bmatrix} \mathbf{M}_0 & & & & 0 \\ -\mathbf{S}' & \mathbf{M}_A & & & \\ & \mathbf{M}_1 & & & \\ & & \mathbf{M}_2 & & \\ & & & \mathbf{M}_3 & \\ 0 & & & & \mathbf{M}_4 \end{bmatrix} & \mathbf{F} &= \begin{bmatrix} \mathbf{F}_{S0} + \mathbf{F}_{G0} + \mathbf{F}_{E0} + \mathbf{F}_{I0} + \mathbf{F}_{C0} \\ 0 \\ \mathbf{F}_c + \mathbf{F}_M \\ 0 \\ \mathbf{F}_{c3} \\ \mathbf{F}_{c4} \end{bmatrix} \\
\mathbf{C} &= \begin{bmatrix} \mathbf{C}_0 + \mathbf{C}_{00}^B + \mathbf{C}_E & 0 & & & \\ 0 & \mathbf{C}_A & & & \\ -\mathbf{C}_{10}^B & 0 & \mathbf{C}_1 + \Delta\mathbf{C}_1 + \mathbf{C}_{11}^B + \mathbf{C}_{11}^G & & \\ -\mathbf{C}_{20}^B & 0 & -\mathbf{C}_{21}^G & \mathbf{C}_2 + \mathbf{C}_{22}^B + \mathbf{C}_{22}^G & \\ -\mathbf{C}_{30}^B & 0 & 0 & -\mathbf{C}_{32}^G & \mathbf{C}_3 + \mathbf{C}_{33}^B + \mathbf{C}_{33}^G \\ -\mathbf{C}_{40}^B & 0 & 0 & -\mathbf{C}_{42}^G & 0 \\ & & & & \mathbf{C}_4 + \mathbf{C}_{44}^B + \mathbf{C}_{44}^G \end{bmatrix} & & (2.47) \\
\mathbf{K} &= \begin{bmatrix} \mathbf{K}_0 + \mathbf{K}_{00}^B + \mathbf{K}_E & 0 & & & \\ 0 & \mathbf{K}_A & & & \\ -\mathbf{K}_{10}^B & 0 & \mathbf{K}_1 + \Delta\mathbf{K}_1 + \mathbf{K}_{11}^B + \mathbf{K}_{11}^G & & \\ -\mathbf{K}_{20}^B & 0 & -\mathbf{K}_{21}^G & \mathbf{K}_2 + \mathbf{K}_{22}^B + \mathbf{K}_{22}^G & \\ -\mathbf{K}_{30}^B & 0 & 0 & -\mathbf{K}_{32}^G & \mathbf{K}_3 + \mathbf{K}_{33}^B + \mathbf{K}_{33}^G \\ -\mathbf{K}_{40}^B & 0 & 0 & -\mathbf{K}_{42}^G & 0 \\ & & & & \mathbf{K}_4 + \mathbf{K}_{44}^B + \mathbf{K}_{44}^G \end{bmatrix}
\end{aligned}$$

The part in red frame represents the coupled system of engine block and water coolant passage. Using the eigenvectors of each part of the total engine system, the equation of motion can be orthogonalized, which is able to be numerically solved by iterative method such as Runge-Kutta-Merson methods [77][78]. The displacement and pressure of the system can be expressed by linear combination of mode shapes.

$$\begin{pmatrix} \mathbf{x}_0 \\ \mathbf{p} \end{pmatrix} = \sum_{n=1}^{n_s+n_A} \begin{pmatrix} \phi'_{on} \\ \psi'_{0n} \end{pmatrix} a_{0n} = \begin{bmatrix} \Phi'_0 \\ \Psi'_0 \end{bmatrix} \mathbf{a}_0 \quad \text{Engine block and Water coolant passage}$$

$$\mathbf{u}_1 = \sum_{n=1}^{n_1} \phi_{1n} a_{1n} = \Phi_1 \mathbf{a}_1 \quad \text{Crank shaft} \quad (2.48)$$

$$\mathbf{x}_q = \sum_{n=1}^{n_q} \phi_{qn} a_{qn} = \Phi_q \mathbf{a}_q \quad \text{Gear trains and shafts } (q=2,3,4)$$

Substituting Eq.(2.48) into Eq.(2.49) and multiplying $\left[(\Phi')^t \quad \Omega(\Psi')^t \right]$ and $\Phi_1^t \sim \Phi_4^t$ from the left side, one can obtain the equation of motion of the total engine system including water coolant passage represented by mode coordinates:

$$\tilde{\mathbf{M}}\ddot{\mathbf{a}} + \tilde{\mathbf{C}}\dot{\mathbf{a}} + \tilde{\mathbf{K}}\mathbf{a} = \tilde{\mathbf{F}} \quad (2.49)$$

where,

$$\mathbf{a} = (\mathbf{a}_0, \mathbf{a}_1, \mathbf{a}_2, \mathbf{a}_3, \mathbf{a}_4)^t$$

$$\begin{aligned}
\tilde{\mathbf{M}} &= \begin{bmatrix} \tilde{\mathbf{M}}_{0A} & & & & 0 \\ & \tilde{\mathbf{M}}_1 & & & \\ & & \tilde{\mathbf{M}}_2 & & \\ & & & \tilde{\mathbf{M}}_3 & \\ 0 & & & & \tilde{\mathbf{M}}_4 \end{bmatrix} & \tilde{\mathbf{F}} &= \begin{bmatrix} \tilde{\mathbf{F}}_{S0} + \tilde{\mathbf{F}}_{G0} + \tilde{\mathbf{F}}_{E0} + \tilde{\mathbf{F}}_{I0} + \tilde{\mathbf{F}}_{C0} \\ & \tilde{\mathbf{F}}_c + \tilde{\mathbf{F}}_M \\ & 0 \\ & \tilde{\mathbf{F}}_{c3} \\ & \tilde{\mathbf{F}}_{c4} \end{bmatrix} \\
\tilde{\mathbf{C}} &= \begin{bmatrix} \tilde{\mathbf{C}}_{0A} + \tilde{\mathbf{C}}_{00}^B + \tilde{\mathbf{C}}_E & -\tilde{\mathbf{C}}_{01}^B & -\tilde{\mathbf{C}}_{02}^B & -\tilde{\mathbf{C}}_{03}^B & -\tilde{\mathbf{C}}_{04}^B \\ -\tilde{\mathbf{C}}_{10}^B & \tilde{\mathbf{C}}_1 + \Delta\tilde{\mathbf{C}}_1 + \tilde{\mathbf{C}}_{11}^B + \tilde{\mathbf{C}}_{11}^G & -\tilde{\mathbf{C}}_{12}^G & 0 & 0 \\ -\tilde{\mathbf{C}}_{20}^B & -\tilde{\mathbf{C}}_{21}^G & \tilde{\mathbf{C}}_2 + \tilde{\mathbf{C}}_{22}^B + \tilde{\mathbf{C}}_{22}^G & -\tilde{\mathbf{C}}_{23}^G & -\tilde{\mathbf{C}}_{24}^G \\ -\tilde{\mathbf{C}}_{30}^B & 0 & -\tilde{\mathbf{C}}_{32}^G & \tilde{\mathbf{C}}_3 + \tilde{\mathbf{C}}_{33}^B + \tilde{\mathbf{C}}_{33}^G & 0 \\ -\tilde{\mathbf{C}}_{40}^B & 0 & -\tilde{\mathbf{C}}_{42}^G & 0 & \tilde{\mathbf{C}}_4 + \tilde{\mathbf{C}}_{44}^B + \tilde{\mathbf{C}}_{44}^G \end{bmatrix} & (2.50) \\
\tilde{\mathbf{K}} &= \begin{bmatrix} \tilde{\mathbf{K}}_{0A} + \tilde{\mathbf{K}}_{00}^B + \tilde{\mathbf{K}}_E & -\tilde{\mathbf{K}}_{01}^B & -\tilde{\mathbf{K}}_{02}^B & -\tilde{\mathbf{K}}_{03}^B & -\tilde{\mathbf{K}}_{04}^B \\ -\tilde{\mathbf{K}}_{10}^B & \tilde{\mathbf{K}}_1 + \Delta\tilde{\mathbf{K}}_1 + \tilde{\mathbf{K}}_{11}^B + \tilde{\mathbf{K}}_{11}^G & -\tilde{\mathbf{K}}_{12}^G & 0 & 0 \\ -\tilde{\mathbf{K}}_{20}^B & -\tilde{\mathbf{K}}_{21}^G & \tilde{\mathbf{K}}_2 + \tilde{\mathbf{K}}_{22}^B + \tilde{\mathbf{K}}_{22}^G & -\tilde{\mathbf{K}}_{23}^G & -\tilde{\mathbf{K}}_{24}^G \\ -\tilde{\mathbf{K}}_{30}^B & 0 & -\tilde{\mathbf{K}}_{32}^G & \tilde{\mathbf{K}}_3 + \tilde{\mathbf{K}}_{33}^B + \tilde{\mathbf{K}}_{33}^G & 0 \\ -\tilde{\mathbf{K}}_{40}^B & 0 & -\tilde{\mathbf{K}}_{42}^G & 0 & \tilde{\mathbf{K}}_4 + \tilde{\mathbf{K}}_{44}^B + \tilde{\mathbf{K}}_{44}^G \end{bmatrix}
\end{aligned}$$

2.5 Chapter summary

In this chapter, the equation of motion of structure coupled with water acoustic field was derived and the modal analysis technique was applied to determine the pressure response induced by impact force acting on the structure. In this analysis, the right and left eigenvectors were used to diagonalize the coupled mass and stiffness matrix for the convenience of the calculation in time domain. Moreover, the equation of motion of the total engine system including acoustic field of water coolant passage and the rotating shafts was formulated to evaluate the water pressure response in the running condition.

The FEM formulations of structural-acoustic coupled system and the orthogonal conditions of left and right eigenvectors are employed by following the previous study[74]. The application of modal analysis technique for engine and water coolant passage coupled system and its incorporation to the equation of motion of fully assembled engine system are newly conducted by author.

Chapter 3

EVALUATION OF NUMERICAL METHOD BY USE OF RECTANGULAR TANK MODEL

As water coolant passage is embraced by crankcase, vibration of cylinder liner will give rise to the pressure fluctuation in the water coolant passage when piston slap forces act on cylinder liner. In this chapter, a rectangular tank model containing water inside is used for evaluating the validity of the numerical procedure to determine the water pressure fluctuation induced by the structural impact vibration. The pressure fluctuation inside the water tank is measured when impact force acts on the bottom plate. The measured results of structural vibration and water pressure are compared with the calculated ones to confirm the applicability of this numerical procedure to the coupled system of engine structure and acoustic field in water coolant passage.

Cavitation occurrence criteria that water pressure falls to the vapor pressure or less is examined by the large impact vibration test. Furthermore, as water pressure fluctuation induced by the structural vibration is supposed to be changed by the coupled vibration characteristics of structure and acoustic field, variation of water pressure response is calculated by changing the sound speed of water.

3.1 Rectangular tank model

The natural frequencies of the water acoustic field in rectangular tank change with the water height. Rectangular tank is designed to be one end open in order to change water height easily. The thickness of the bottom plate (3mm) is thinner than that of side wall (10mm) to be excited more easily and two rib-stiffeners are welded to the side wall as shown in Fig.3.1.

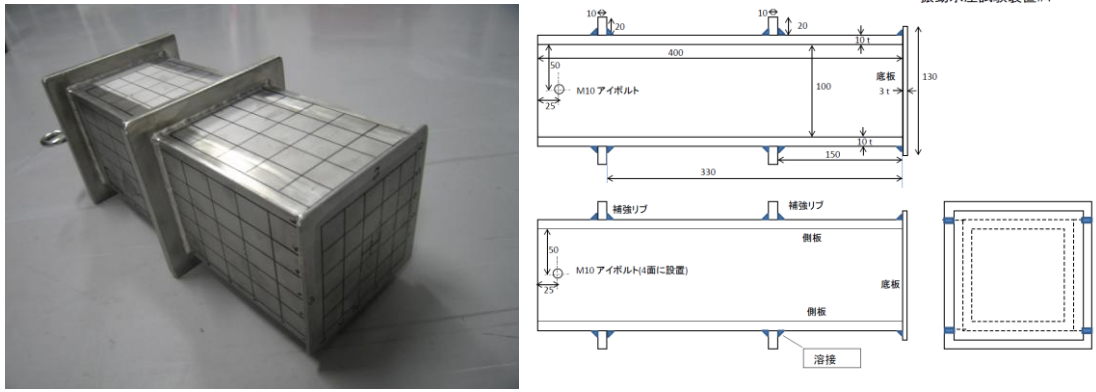


Fig.3.1 Rectangular tank model

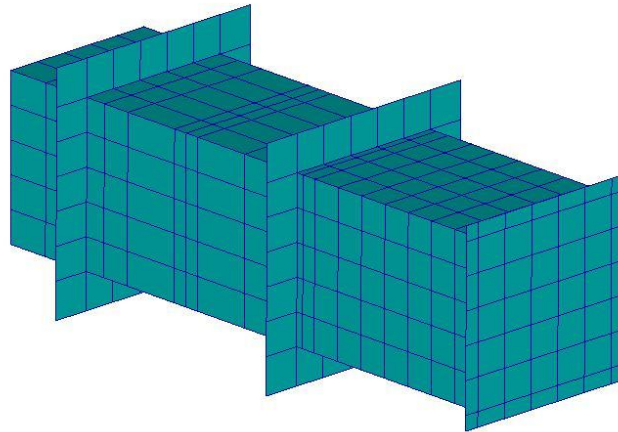


Fig.3.2 FEM model of rectangular tank structure

Table.3.1 Calculation parameters of tank model

Number of Grid	520
Number of element	497
Material	Carbon Steel (S35C)
Density	7.8 kg/m ³
Poisson's Ratio	0.3
Elastic modulus	210 GPa

Figure 3.2 shows the FEM model of rectangular tank which is created by shell elements. The calculation parameters of tank models are shown in Table.3.1. Eigenvalue analysis is carried out to obtain natural frequencies and mode shapes which are compared with the measured ones in air. The mode shapes and natural frequencies calculated by FEM agree with measured results as shown in Fig.3.4 [79][80]. Fig.3.3 shows that the error of natural frequencies is within $\pm 7\%$. In order to compare the calculation results of coupled system with experimental results, the measured natural frequency and damping of rectangular tank model are used in the calculation.

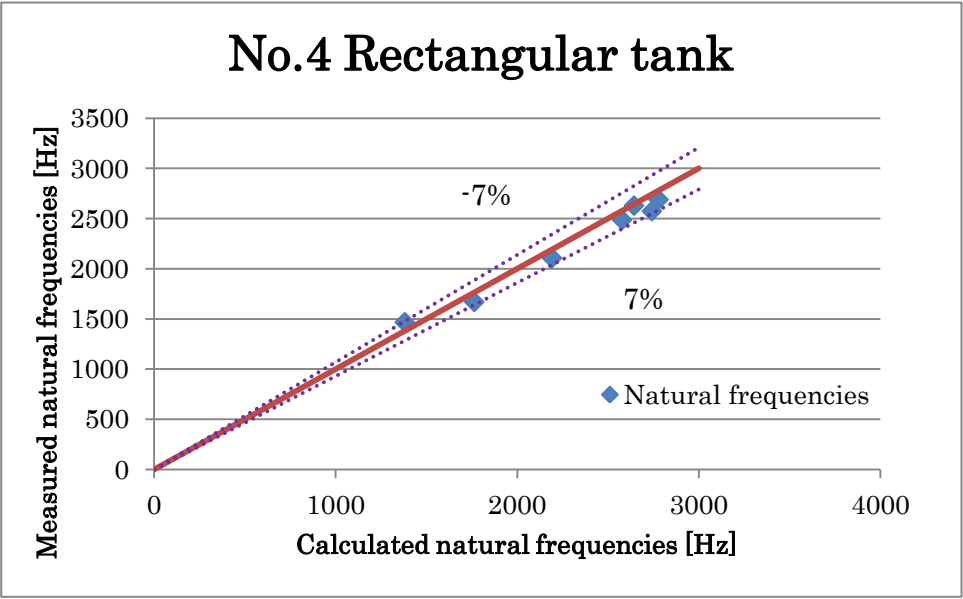


Fig.3.3 Comparison between measured and calculated natural frequencies of rectangular tank model

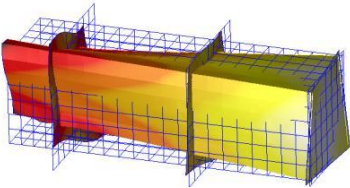
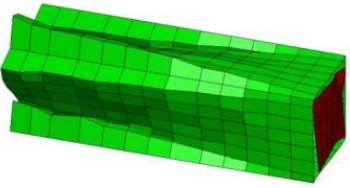
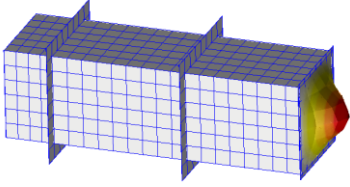
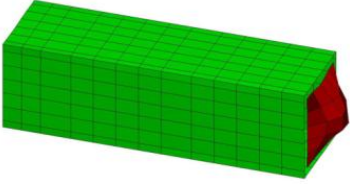
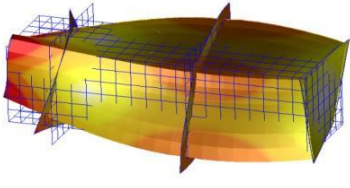
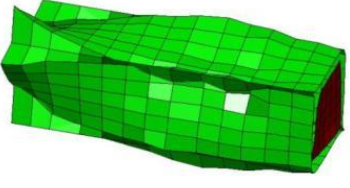
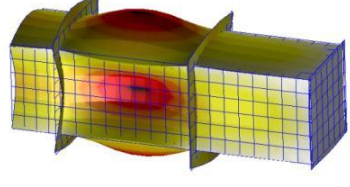
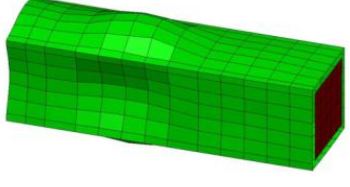
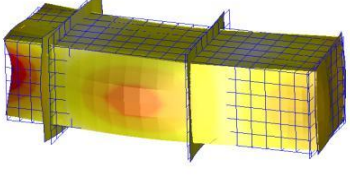
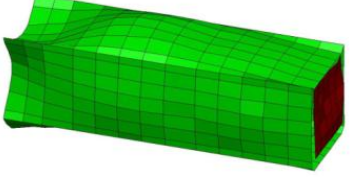
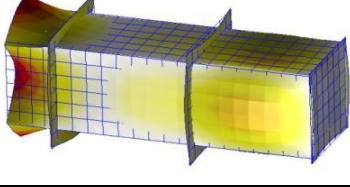
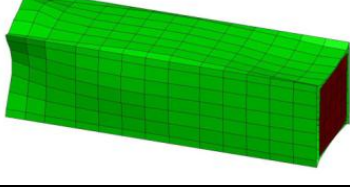
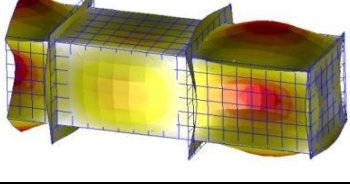
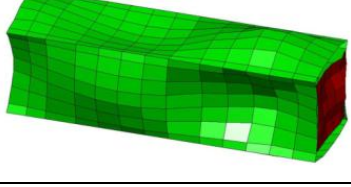
mode No.		Calculated		Measured
1	1381.0 Hz		1467.5 Hz	
2	1764.4 Hz		1670 Hz	
3	2191.9 Hz		2107.5 Hz	
4	2577.9Hz		2487.5 Hz	
5&6	2644.0 Hz		2630.0 Hz	
7	2742.4Hz		2575.0 Hz	
8	2779.3Hz		2690.0 Hz	

Fig.3.4 Calculated and measured natural frequencies and mode shapes of rectangular tank model

3.2 FEM model of acoustic field

Figure 3.5 shows the FEM model of acoustic field inside the rectangular tank, which is created by solid elements. By use of the similarity of equation of motion between structure and acoustic field, shown in Appendix B(1), dynamic characteristic of the acoustic field can be numerically analyzed by NASTRAN with changing the density and Young's modulus. The medium of the acoustic field is tap water and its density is set to be $\rho=1000\text{kg/m}^3$. The speed of sound in water is measured through experiments, which changes in the range of 500~1100 m/s due to the variation of air void ratio [79][80][81]. The relationship between sound speed and void fraction can be seen in Appendix B (3). The sound speed of acoustic field is assumed to be 850m/s for this rectangular tank [79].

Figure 3.6 shows the calculated mode shapes and natural frequencies of the water acoustic field calculated by NASTRAN. As the configuration of the acoustic field is cuboid with one open end, acoustic mode shape along the depth is like a cosine wave with one end open and other sides are closed. In this model, natural frequencies are theoretically determined, of which the detailed procedure are shown in Appendix B(2). FEM analysis coincides with theoretical results as shown in Fig.3.6.

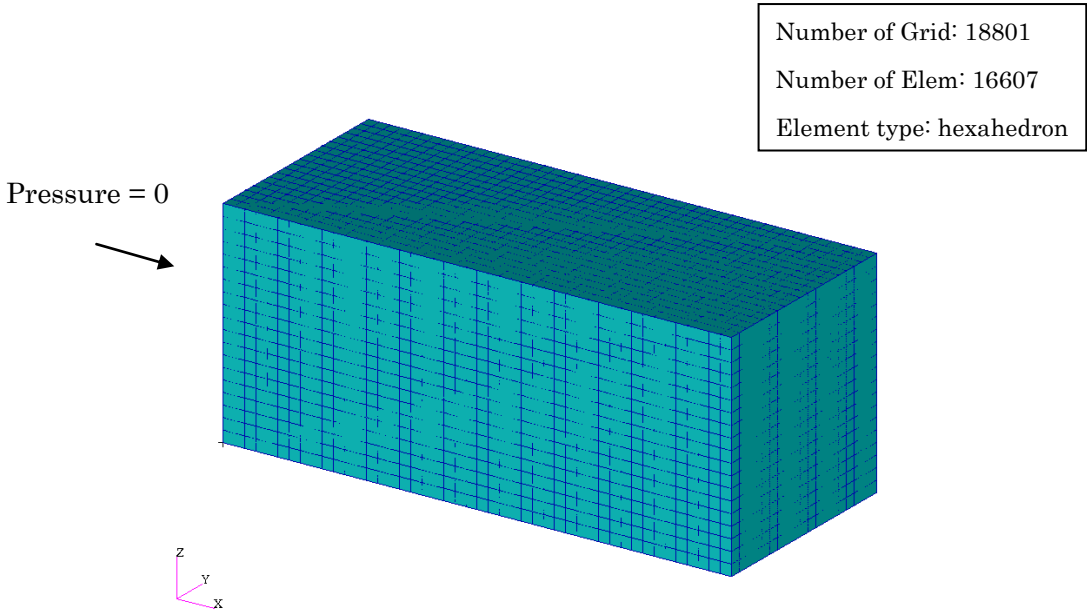


Fig.3.5 FEM model of acoustic field inside rectangular tank

Mode number	Mode shape (FEM)	Mode shape (Theory)	FEM frequency(Hz)	Analytical frequency(Hz)
1			699.999	700
2			2099.8	2100
3			3374.2	3375
4			3374.2	3375
5			3498.9	3500
6			4897.1	4900

Fig.3.6 Acoustic model analyzed by Nastran at Hw=250mm

3.3 Pressure fluctuation and structure vibration induced by impact force

(1) Frequency response and natural frequencies and mode shapes

Figure 3.7 shows the rectangular tank model and experimental setup to measure the water pressure and structural vibration. Impact force was applied on bottom plate of rectangular tank model. The frequency response of acceleration and pressure of the structural-acoustic coupled system and the corresponding mode shapes were measured.

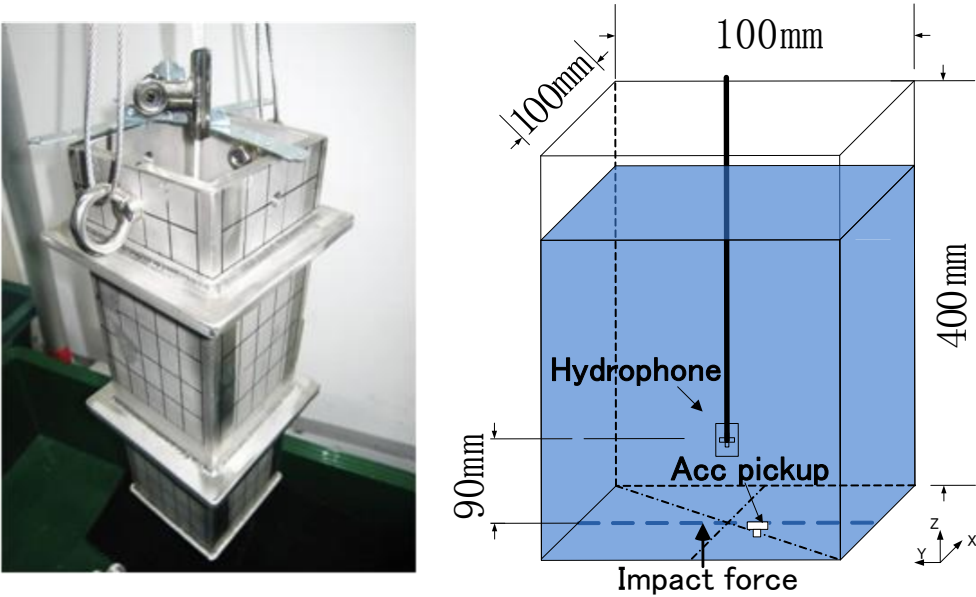


Fig.3.7 Experiment set up of rectangular tank

Fig.3.8 shows measured and calculated frequency response function of bottom plate acceleration and water pressure induced by impact force at water depth $H_w=250\text{mm}$. Hydrophone was located 90mm above the bottom plate ($H_p=90\text{mm}$). Peaks in the frequency response are seen at 600Hz and 1600Hz.

Fig.3.9 shows measured and calculated frequency response of acceleration and water pressure induced by impact force at water depth $H_w=350\text{mm}$ and hydrophone location $H_p=90\text{mm}$, peak frequencies are seen at 500Hz and 1300Hz, and these frequencies are lower compared with those of the case in $H_w=250\text{mm}$.

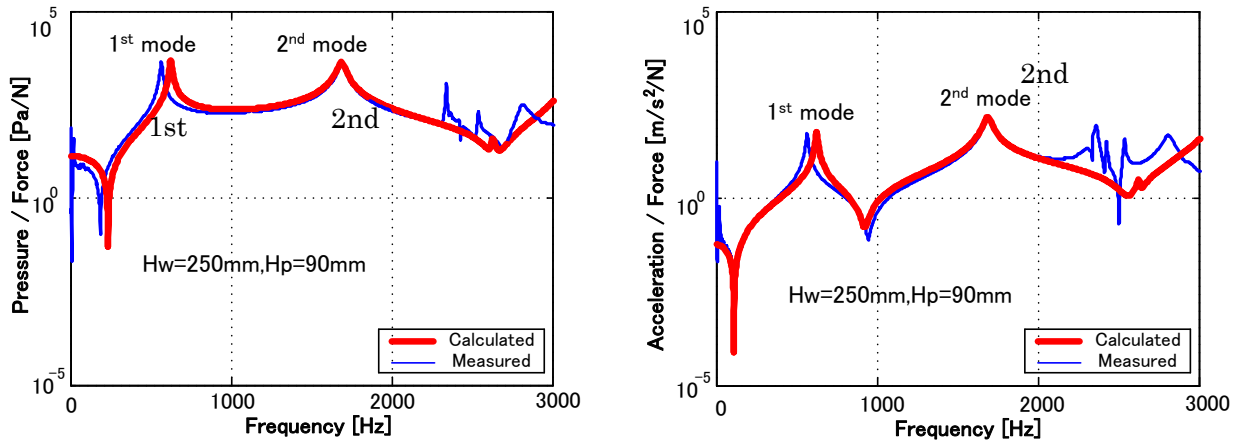


Fig.3.8 Measured and calculated acceleration and pressure at water depth 250mm

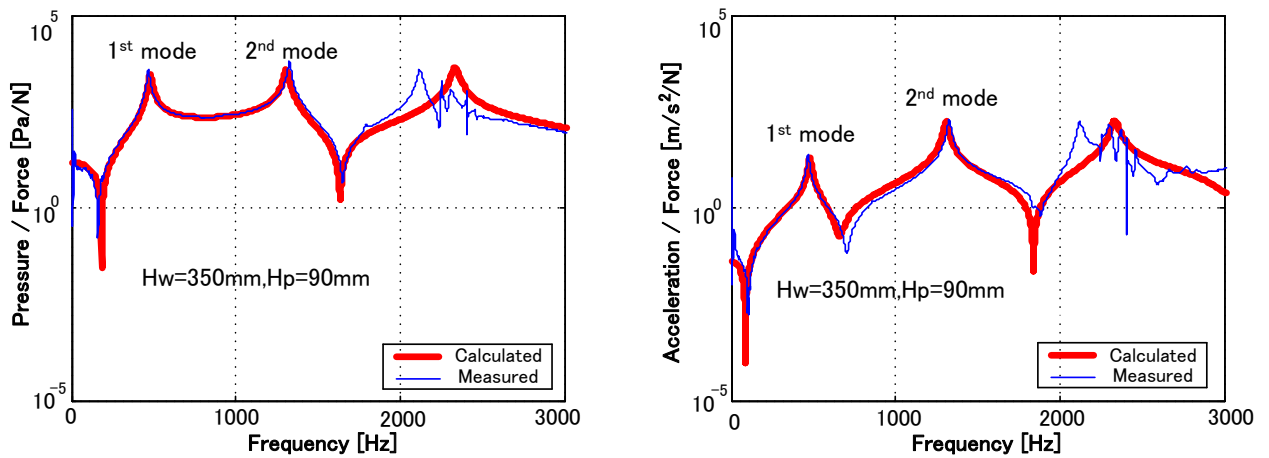
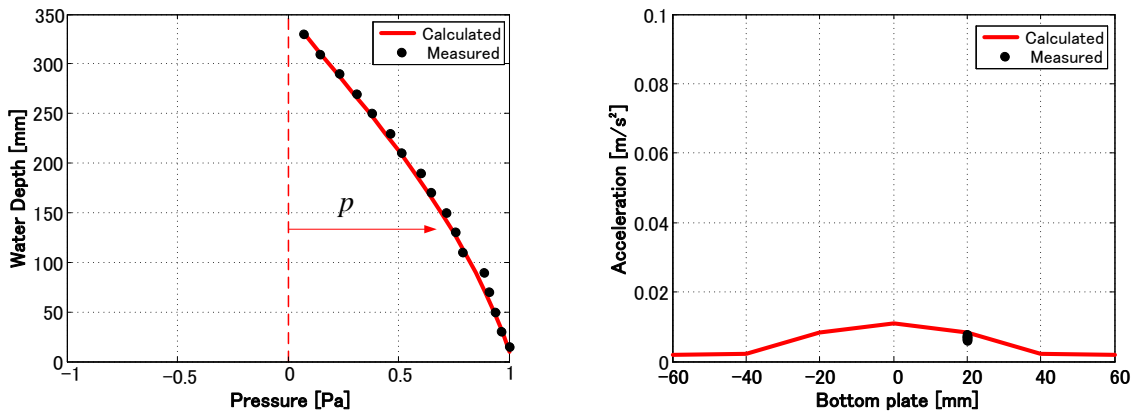
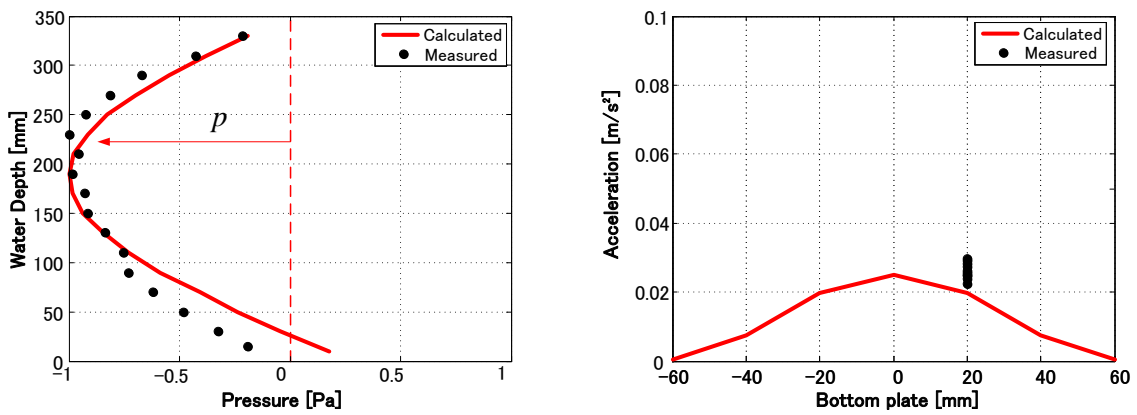


Fig.3.9 Measured and calculated acceleration and pressure at water depth 350mm

Figure 3.10 shows the pressure mode shape in the vertical direction and acceleration mode shape of the bottom plate at the first and second resonance frequencies when the water height is $H_w=350\text{mm}$. The acoustic mode shapes were measured by changing the height of hydrophone vertically from 20mm to the near surface. The first acoustic resonance mode of quarter wavelength is observed. In the first mode shown Fig.3.10(a), positive acceleration of the bottom plate results in positive pressure near the bottom plate, which shows the added mass effect of the fluid. In the second mode, bottom plate vibration is relatively larger than that of the first mode, and the pressure does not have maximum amplitude at the bottom boundary. The added mass or stiffness effect of the fluid is not clear, since the second mode of pressure has small value at the bottom plate. Measured mode shape of the pressure for the first and second mode closely coincides with the calculated ones.



(a) First mode of water pressure and bottom plate vibration at $H_W = 350\text{mm}$



(b) Second mode of water pressure and bottom plate vibration at $H_W = 350\text{mm}$

Fig.3.10 Measured and calculated mode shape of pressure and acceleration

Fig.3.11 shows the comparison of measured and calculated first and second coupled natural frequencies at different water depths. Coupled natural frequencies increase when the water depth decreases.

The second resonance frequency changes with water depth greater than the first resonance. When the water depth decreases, the second resonance frequency crosses the in-air natural frequency (1670Hz) of the second mode of bottom plate as shown in Fig.3.4, the added mass effect of fluid changes to added stiffness effect. This means the pressure near the bottom plate changes from positive to negative when the bottom plate acceleration is positive.

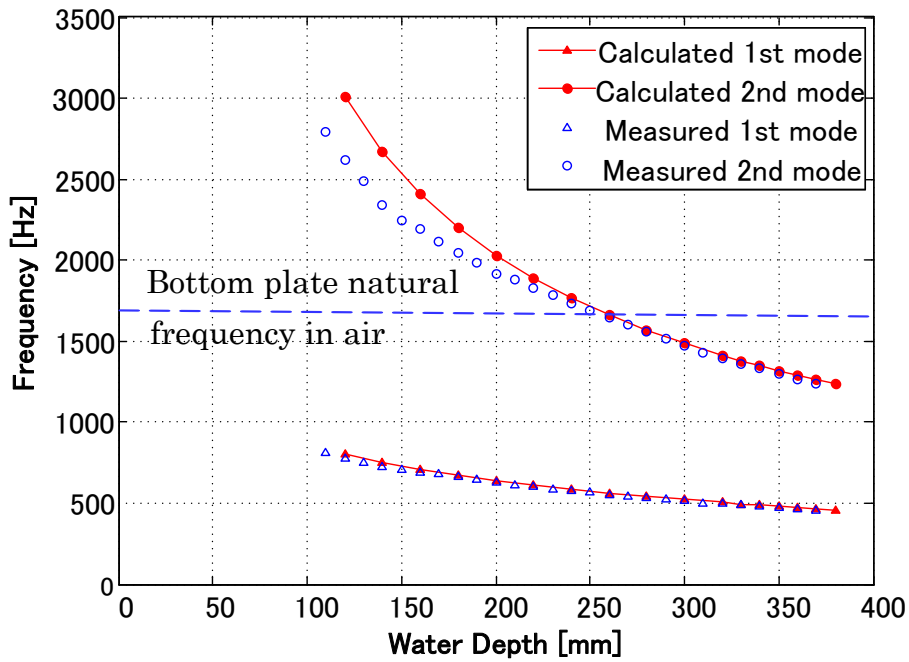


Fig.3.11 Measured and calculated coupled frequencies changing with water depth

(2) Response in time domain and occurrence of cavitation

As cavitation occurs when the water pressure fluctuations reaches or goes below the saturated vapor pressure and repeats in accordance with the period of oscillation, it is essential to predict the water pressure time history to perform a cavitation prevent design. Figure 3.12 shows the comparison of measured and calculated water pressure waveform at a water depth $H_w=350\text{mm}$ and hydrophone height $H_p=90\text{mm}$. The maximum amplitudes of negative pressure is $9.5 \times 10^4 \text{ Pa}$ in calculation and $9.2 \times 10^4 \text{ Pa}$ in measurement and these difference is within 3.3%. The decay time of 90% off are also compared between calculation (0.0515s) and experiment (0.0508s) and its difference is within 1.4%. The calculated waveform is in good agreement with the measured one and the validity of the present method has been confirmed.

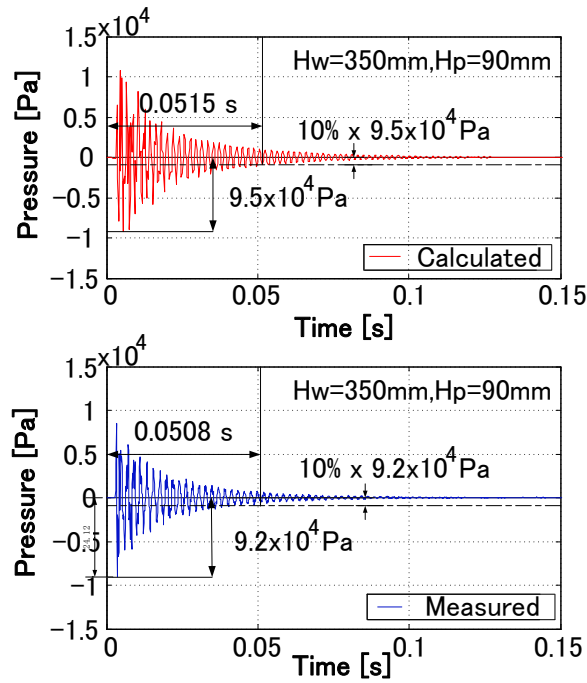
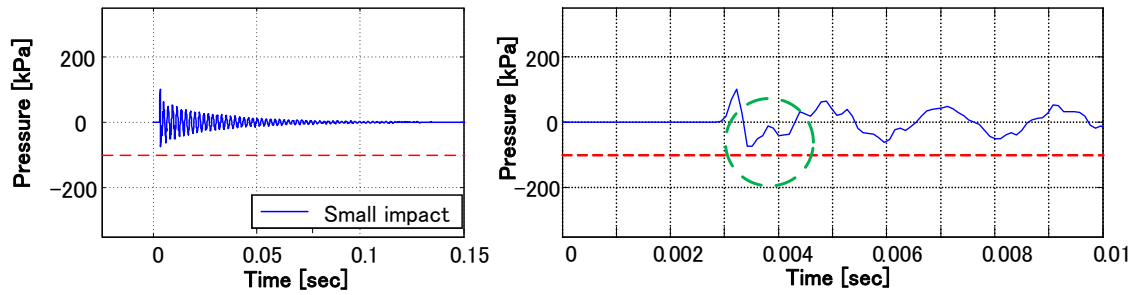
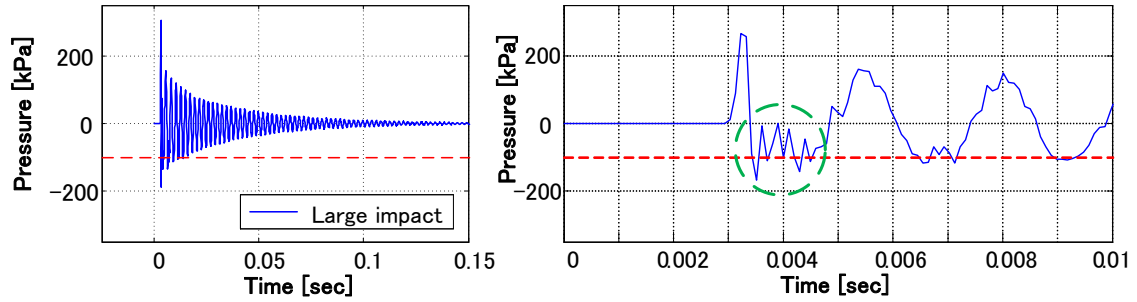


Fig.3.12 Measured and calculated water pressure at water depth 350mm

The measured water pressure waveforms caused by small and large impact force are shown in Fig.3.13. The measurement is carried out at water depth $H_w=350\text{mm}$ and hydrophone height from the bottom $H_p=10\text{mm}$. At 20°C of standard atmosphere (101.4kPa), the vapor pressure is 2.3kPa [82], cavitation will happen when negative pressure reaches to -99.1kPa ($2.3\text{kPa}-101.4\text{kPa}$) or less. When the impact force is small, the negative pressure does not reach -99.1kPa indicated by the red dotted line which dictates the onset of cavitation. When the impact force is large enough, the pressure can reach -99.1kPa or less. In small impact vibration, pressure fluctuation waveform is almost vertically symmetric. In the large impact vibration, as shown in the enlarged view of pressure just after the impact excitation, pressure fluctuation of the negative side reaches the saturated vapor pressure and high frequency components are seen there. These high frequency components seem to come from the occurrence of cavitation.



(a) Pressure response by small impact force



(b) Pressure response by large impact force

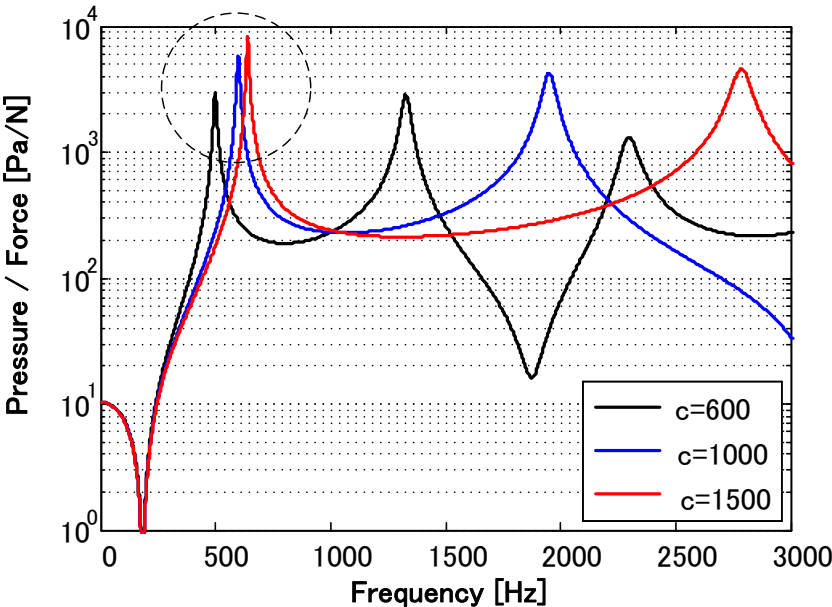
Fig.3.13 Measured waveform of water pressure at the water depth $H_w=350\text{mm}$

3.4 Effect of variation of sound speed

The natural frequencies of water coolant passage are affected by the configuration of water coolant passage and the sound speed of coolant which is influenced by the void ratio [77][78]. In real engines, when natural frequencies of cylinder liners get close to the natural frequencies of water coolant passage, the piston slap induced water pressure fluctuation is expected to be larger. In this section, by use of rectangular tank model, the effect of variation of sound speed (variation of natural frequency of acoustic field) on the water pressure fluctuation is to be numerically investigated. When water height is $H_w = 250\text{mm}$, natural frequency of first mode of acoustic field will change from $f_w=600\text{Hz}$ to $f_w=1500\text{Hz}$ with sound speed changing from $c=600\text{m/s}$ to $c=1500\text{m/s}$, which gets close to the natural frequency of bottom plate vibration mode ($f_p=1670\text{Hz}$).

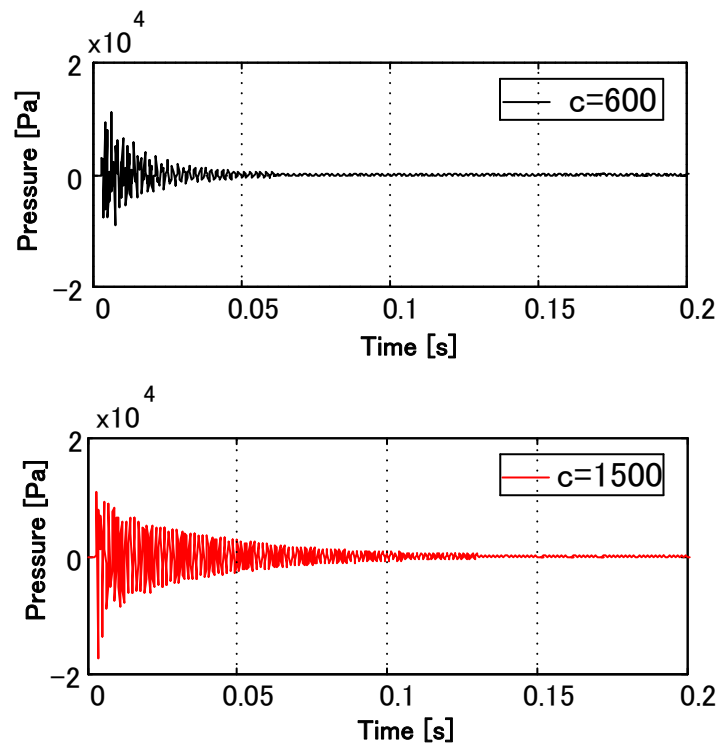
When sound speed changes from 600m/s to 1500m/s , the pressure frequency response near

the bottom plate becomes larger as can be seen in Fig.3.14(a). In time domain, the pressure waveform of sound speed $c=1500\text{m/s}$ is also larger than that of $c=600\text{m/s}$ as can be seen in Fig.3.14(b). Both the frequency response and waveform suggest that when the natural frequency f_w of the first mode of acoustic field gets close to the natural frequency f_p of the bottom vibration mode, larger pressure fluctuation is prospected.



(a) Frequency response of water pressure at bottom plate

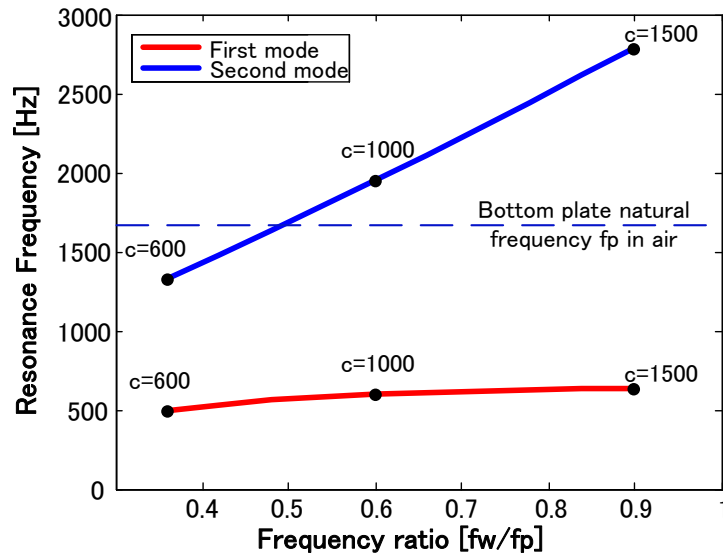
Fig.3.14 Pressure at the water depth $H_w=350\text{mm}$ of different sound speed



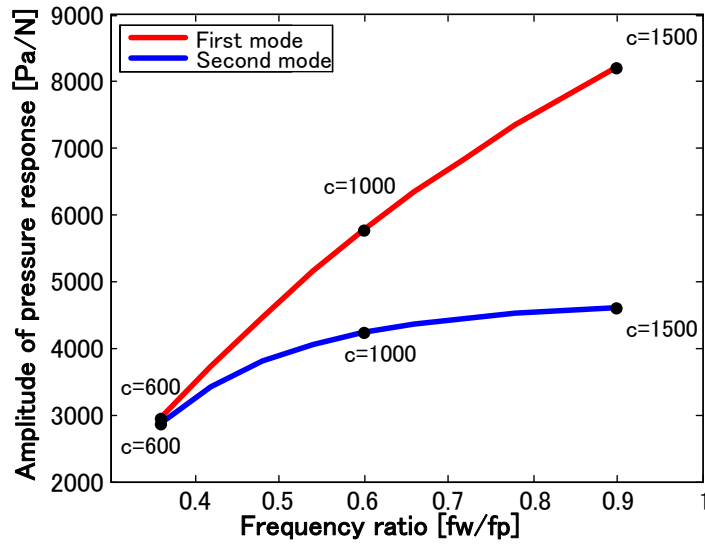
(b) Waveform of water pressure at bottom plate

Fig.3.14 Pressure at the water depth $H_w=350\text{mm}$ of different sound speed

Figure 3.15 (a) shows the trend of the coupled natural frequencies changing with frequency ratio between the first mode of acoustic field f_w and bottom plate vibration mode f_p . Peak values of water pressure at coupled resonance frequencies are shown in Fig.3.15 (b). When the frequency ratio f_w/f_p gets close to 1, the water pressure peak value of the first mode increases to almost 3 times than the peak value of $f_w/f_p = 0.35$.



(a) Coupled natural frequencies of structure and acoustic field

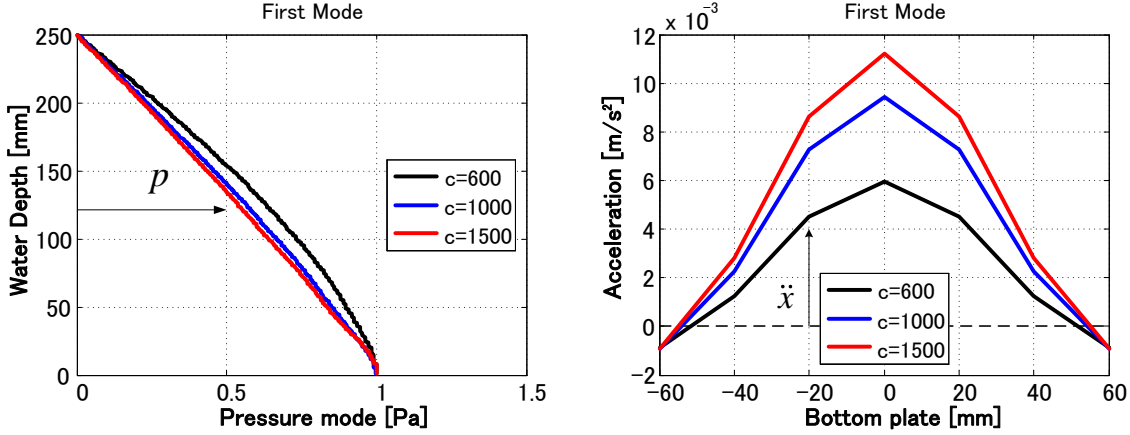


(b) Resonance amplitude of water pressure

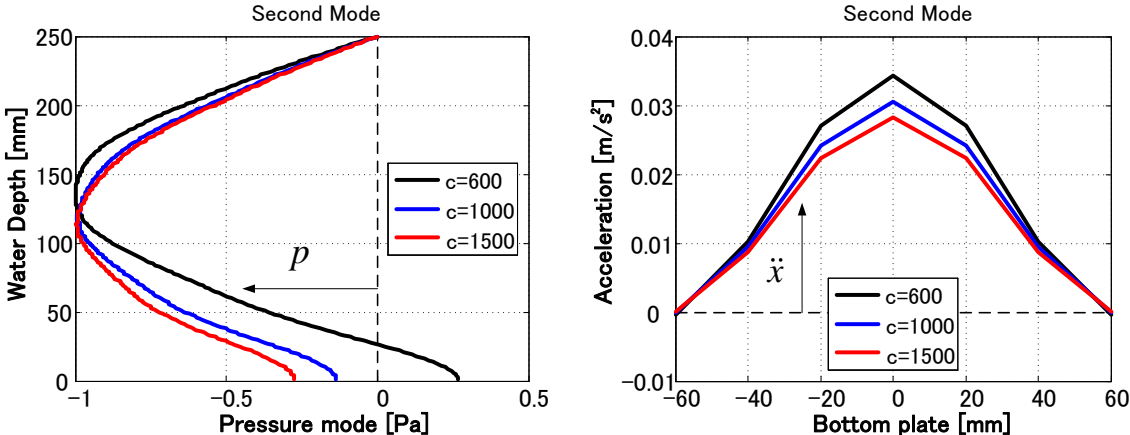
Fig3.15 Effect of the frequency ratio of structure and water acoustic field

Figure 3.16 shows the pressure mode shapes and bottom vibration mode shapes at two resonance peaks changing with different sound speed. As to the first mode, when the acceleration of bottom is positive, the pressure acting on the bottom plate is also positive, from the view point of bottom, the acoustic field acts as added mass. As to the second mode, when the acceleration of bottom is positive, the pressure acting on the bottom plate at 600m/s is positive, while at 1000m/s and 1500m/s is negative, which indicated the effect of acoustic field becomes from added mass to added stiffness. Therefore, the second coupled natural frequency

becomes larger than structural natural frequency f_p of bottom plate in air. The process of analysis at different sound speed demonstrates the coupled effect between acoustic field and structure, which is critical to analyze cavitation occurrence from the perspective of coupled effect between engine and water coolant passage.



(a) Structural and acoustic mode shape of the first mode at different sound speed



(b) Structural and acoustic mode shape of the second mode at different sound speed

Fig.3.16 Structural and acoustic mode shape of rectangular tank at different sound speed

3.5 Chapter summary

In this chapter, FEM models of rectangular tank and the acoustic field inside were created and the coupled system between rectangular tank and acoustic field inside were analyzed. Through experiment, the validity of the numerical method proposed in Chapter 2 has been verified. The method considers the coupling effect on the interaction boundary between structural vibration and pressure fluctuation of acoustic field. The effect of variation of sound speed has been discussed. As the natural frequency of acoustic field approaches to the natural frequency of structure, larger pressure fluctuation is expected.

Chapter 4

APPLICATION OF THE NUMERICAL METHOD TO THE INTERNAL COMBUSTION ENGINE

Liner cavitation erosion is caused by water coolant pressure fluctuation which is mainly induced by engine structure vibration, especially liner vibration. As piston slap is deemed as the main factor of liner vibration, prediction of pressure fluctuation induced by piston slap forces is crucial to relieve liner cavitation erosion. In this chapter, the numerical model of coupled system of water acoustic field and engine structure is established by FEM and modal analysis technique. Pressure fluctuation in water coolant passage induced by piston slap forces is predicted and influences of the change of natural frequencies of acoustic field and different cylinder's piston slap are discussed. Moreover, the contribution of piston slap on the water pressure fluctuation in running condition, in which all exciting forces are considered, is investigated.

4.1 Vibration characteristics of water acoustic field

(1) FEM models of crankcase and water coolant passage

The numerical analysis is carried out based on FEM models of real engine structure and the acoustic field inside. The engine is 4 cycles and 4 cylinders industrial use diesel engine with displacement of 3.5L as shown in Fig.4.1 and its FEM model with shell and beam elements is created. FEM model of water coolant passage with tetrahedral elements is created according to a sand mold as shown in Fig.4.2. There are 13 holes at the top of crankcase through which coolant water flows into the cylinder head and 3 holds at anti thrust side for incoming coolant from water pump. The boundary condition of pressure at the 16 holes is assumed to be zero in this analysis to compare the measured result.

The dynamic characteristics of crankcase and acoustic field in water coolant passage are

obtained by FEM analysis and these results are used in the coupled analysis. The calculated mode shapes of crankcase are shown in Fig.4.3.

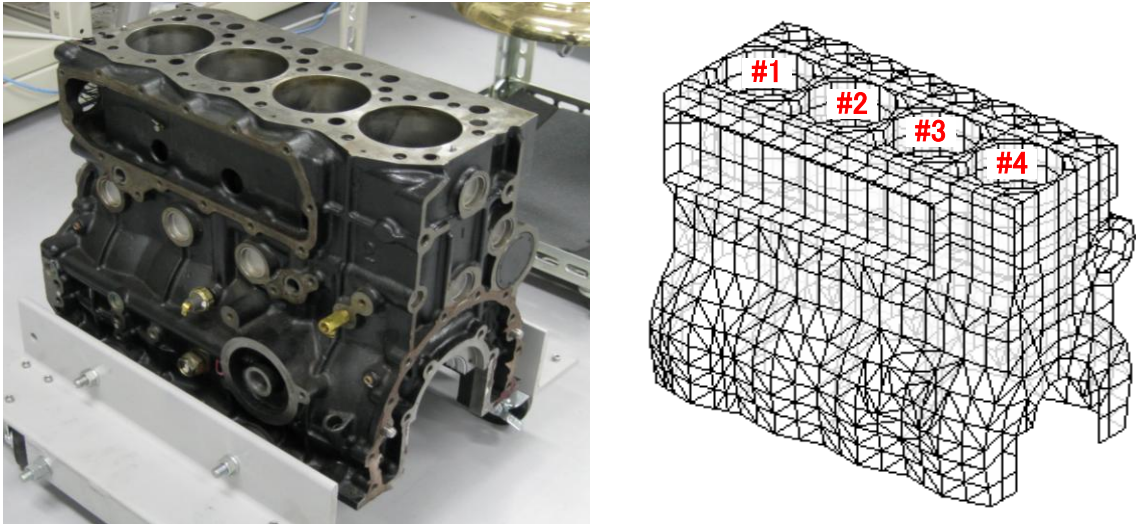


Fig.4.1 Engine crankcase and its FEM model

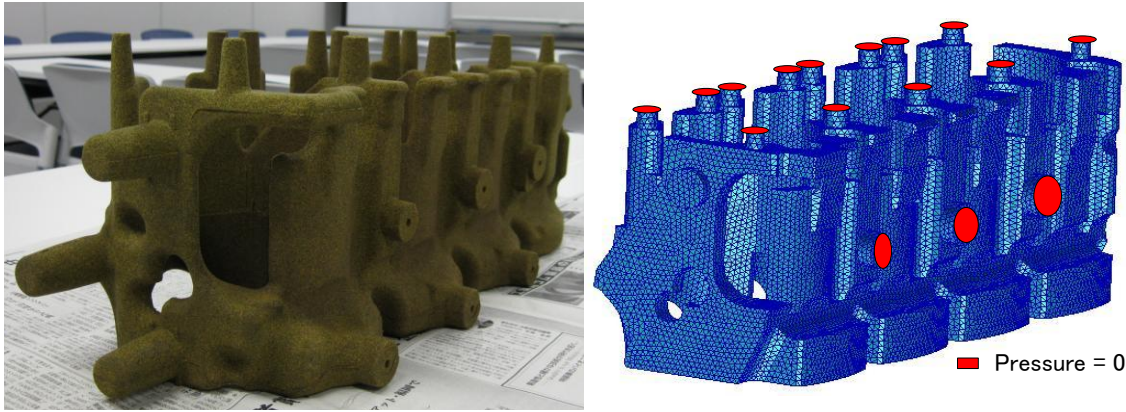


Fig.4.2 Sand mold and FEM models of water coolant passage without covers

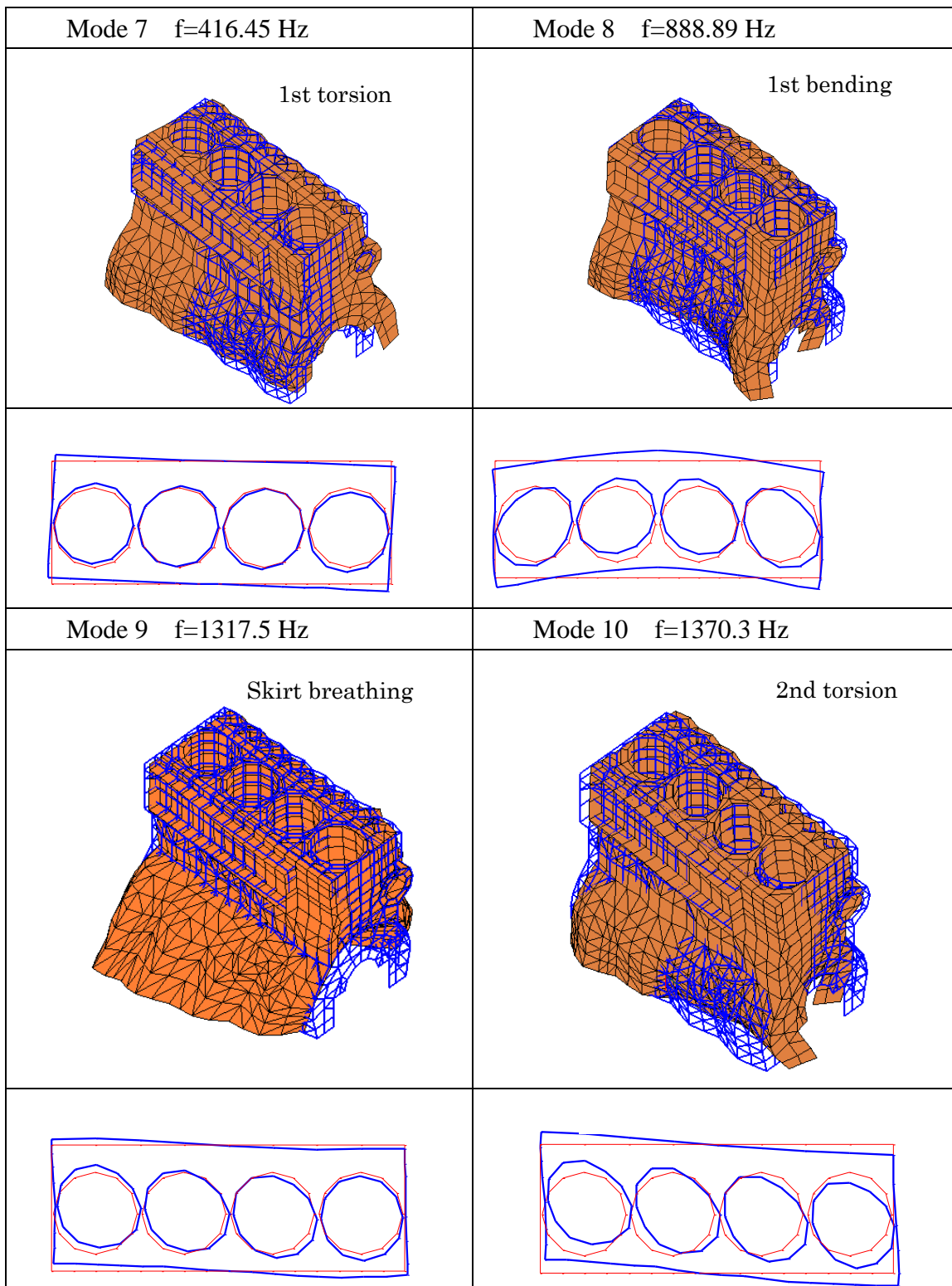


Fig.4.3 Calculated mode shapes of crankcase

The calculated mode shapes of acoustic field are shown in Fig.4.4 when the speed of sound is $c=340\text{m/s}$ (in air). The first mode shape of acoustic field shows that sign of the pressure is all the same, which indicates the Helmholtz resonance mode. In the second mode, pressure mode shapes of #1 and #2 cylinder side are positive, while the pressure mode shapes of #3 and #4 cylinder side are negative. The third mode suggests that pressure mode of anti thrust side is negative, while the pressure mode of thrust side is positive. In the fourth mode, pressure mode of anti thrust side of #1 and #2 cylinders and thrust side of #3 and #4 cylinders are negative, while pressure mode of thrust side of #1 and #2 cylinders and anti thrust side of #3 and #4 cylinders are positive. These first four modes have large influence to the coupled dynamic properties of engine structure and acoustic field of water coolant passage as discussed later.

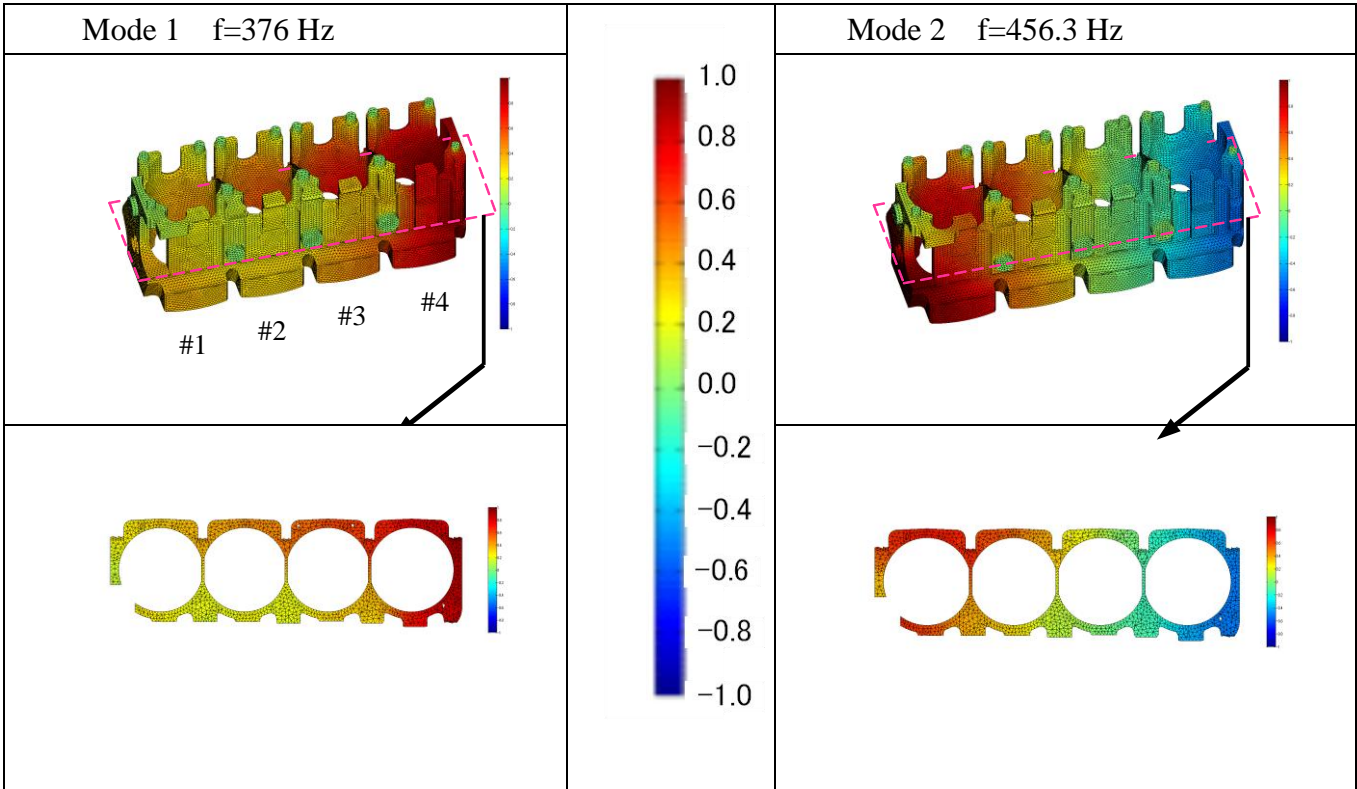


Fig.4.4 (a) Calculated pressure mode shapes of water coolant passage ($c=340\text{m/s}$)

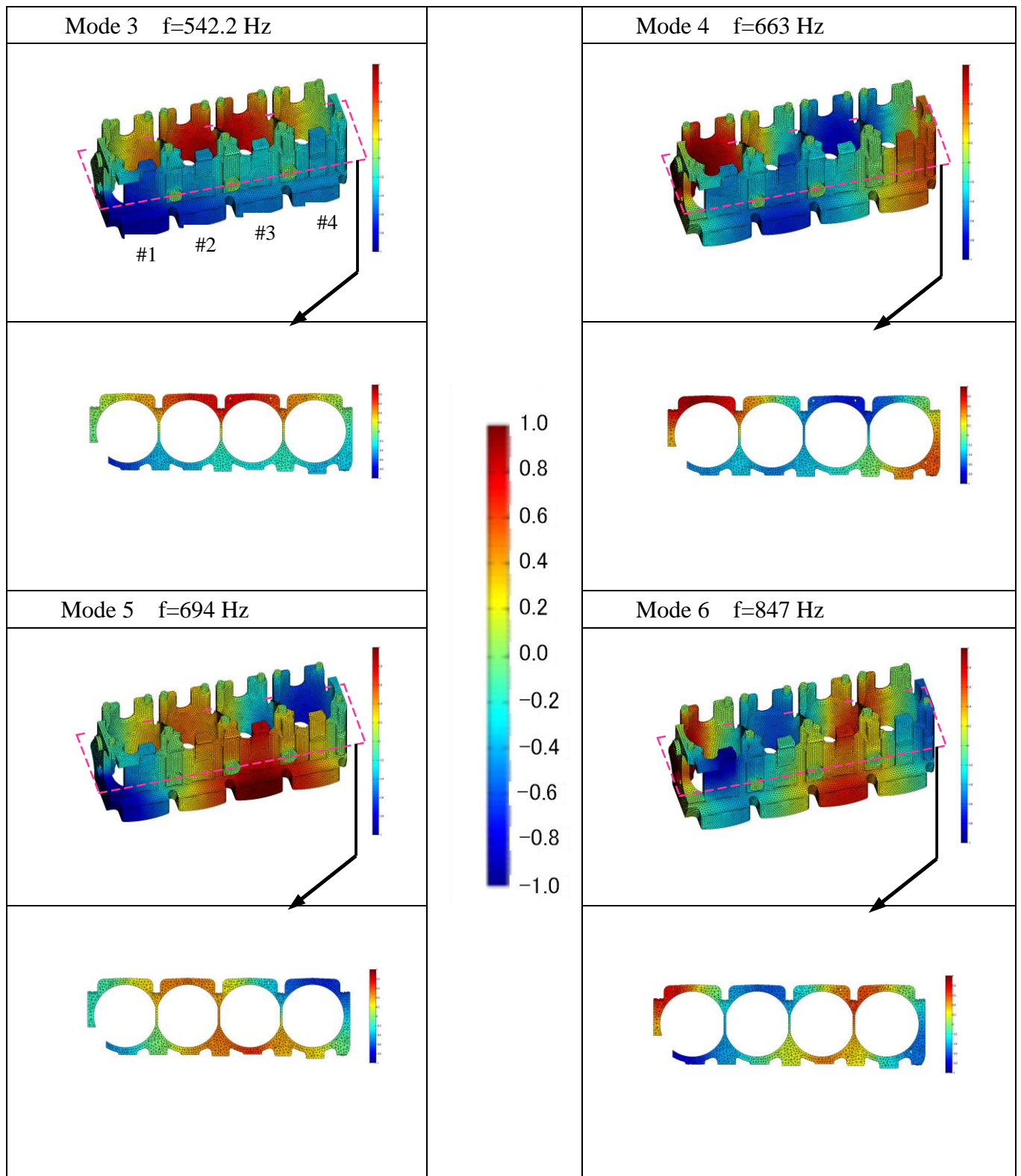


Fig.4.4 (b) Calculated pressure mode shapes of water coolant passage ($c=340$ m/s)

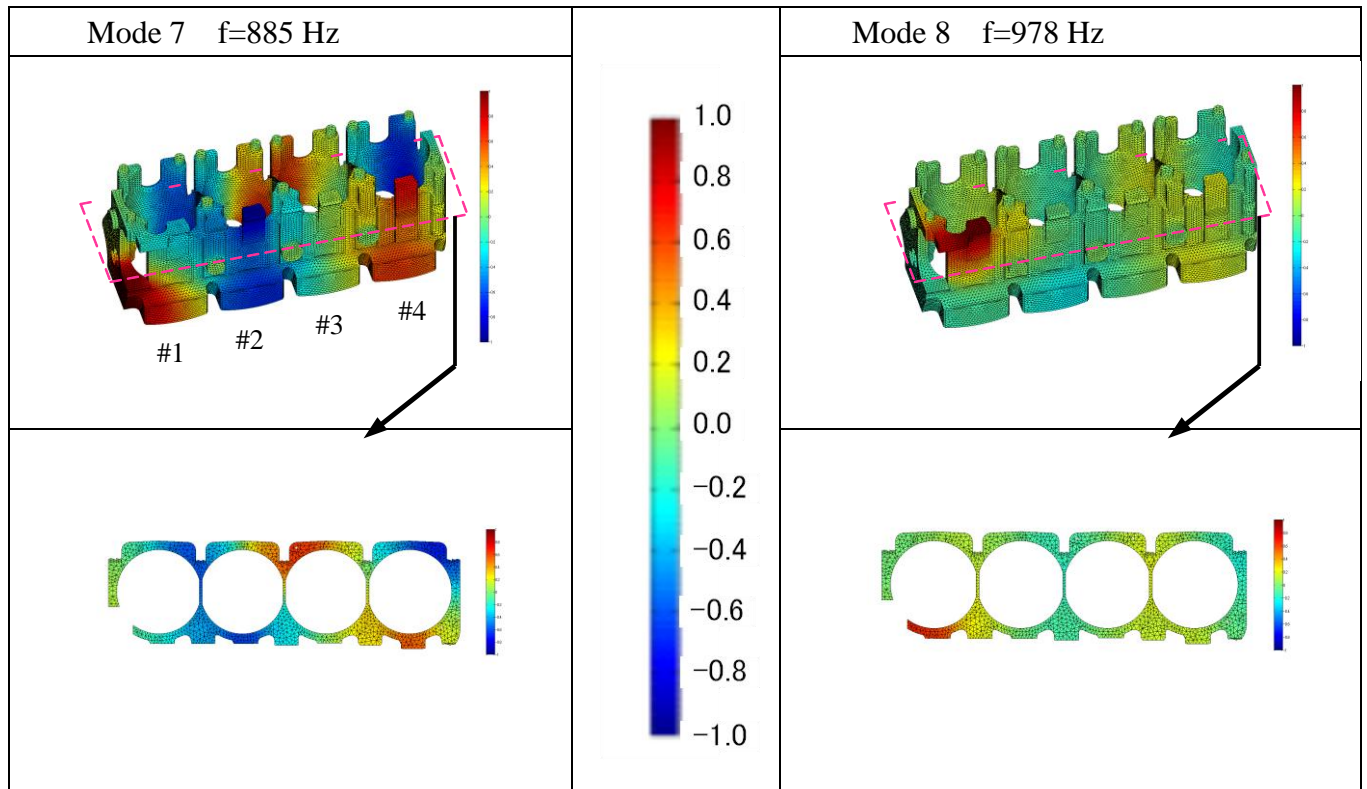


Fig.4.4 (c) Calculated pressure mode shapes of water coolant passage ($c=340\text{m/s}$)

(2) Experimental verification of acoustic numerical model of water coolant passage

Since the mass and stiffness of crankcase is much larger than that of acoustic field in air, the coupling effect between the two systems is not significant; the pressure fluctuation of the acoustic field in air induced by structural vibration can be viewed as the forced response of acoustic field without mutual interaction. The measured and calculated resonance frequencies of acoustic field and the corresponding mode shape are compared simultaneously to evaluate the accuracy of FEM model of acoustic field.

The pressure resonance frequencies are measured through hammer impact test. Acceleration pickup is attached on the surface of crankcase and microphone is inserted into the water coolant passage in the crankcase as shown in Fig.4.5. The mode shapes of acoustic field are measured by two microphones, one is fixed at No.2 hole as reference point, the other microphone moves

sequentially among the rest holes as shown in Fig.4.6. The diameter of circle and clock hand represent the relative amplitude and phase with respect to that of No.2 hole. The comparison of mode shapes between experiment and calculation are shown in Fig.4.7. The resonance frequencies corresponding to the same mode shape are compared in Fig.4.8 and the difference between experiment and calculation is within 6%.



Fig.4.5 Hammer impact test to measure vibration and pressure in air

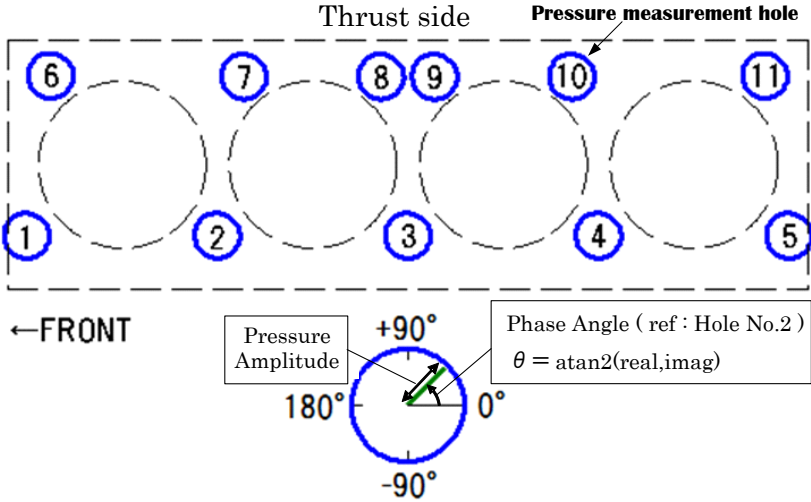


Fig.4.6 Display of amplitude and phase of measured pressure

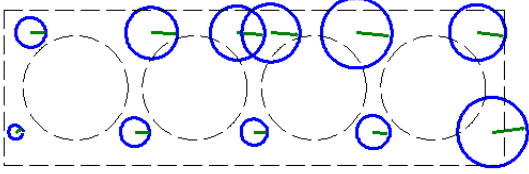
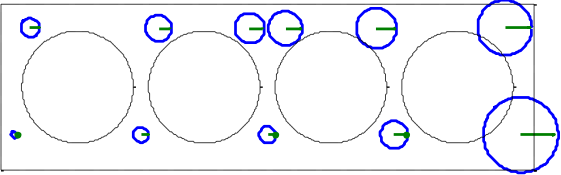
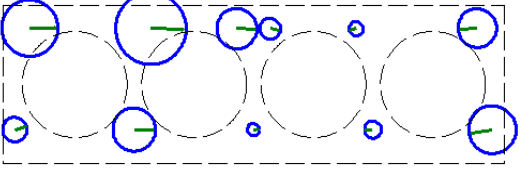
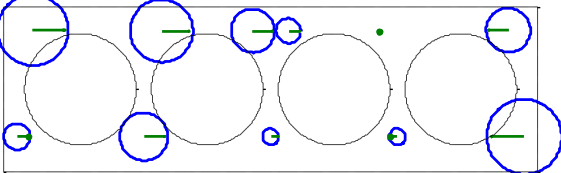
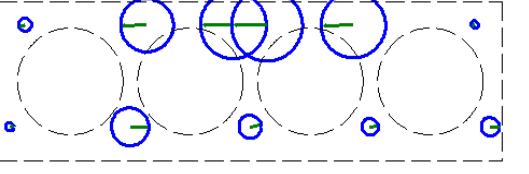
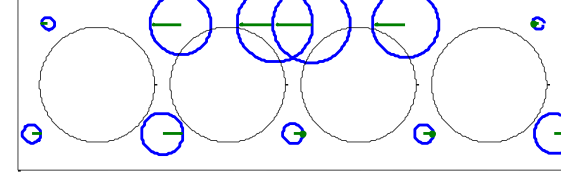
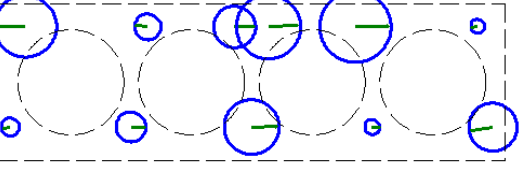
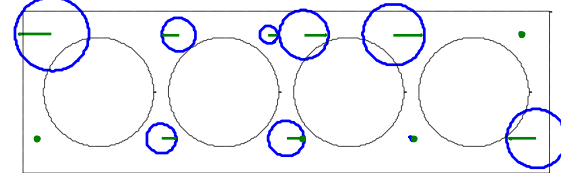
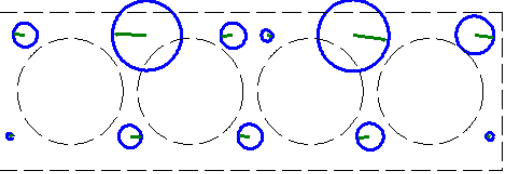
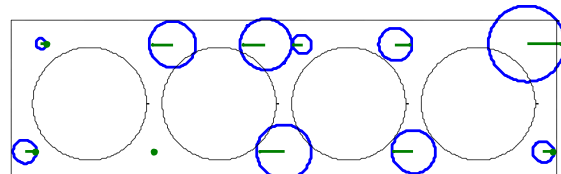
Experiment	Calculation
<p data-bbox="363 241 627 275">Mode 1 $f=350$ Hz</p> 	<p data-bbox="970 241 1217 275">Mode 1 $f=375$Hz</p> 
<p data-bbox="363 595 627 629">Mode 2 $f=440$ Hz</p> 	<p data-bbox="970 573 1217 607">Mode 2 $f=456.3$ Hz</p> 
<p data-bbox="363 931 627 965">Mode 3 $f=530$ Hz</p> 	<p data-bbox="970 931 1217 965">Mode 3 $f=542.2$ Hz</p> 
<p data-bbox="363 1267 627 1301">Mode 4 $f=650$ Hz</p> 	<p data-bbox="970 1267 1217 1301">Mode 4 $f=663$ Hz</p> 
<p data-bbox="363 1570 627 1603">Mode 5 $f=680$ Hz</p> 	<p data-bbox="970 1570 1217 1603">Mode 5 $f=694$ Hz</p> 

Fig.4.7 (a) Comparison of mode shapes of water coolant passage without covers

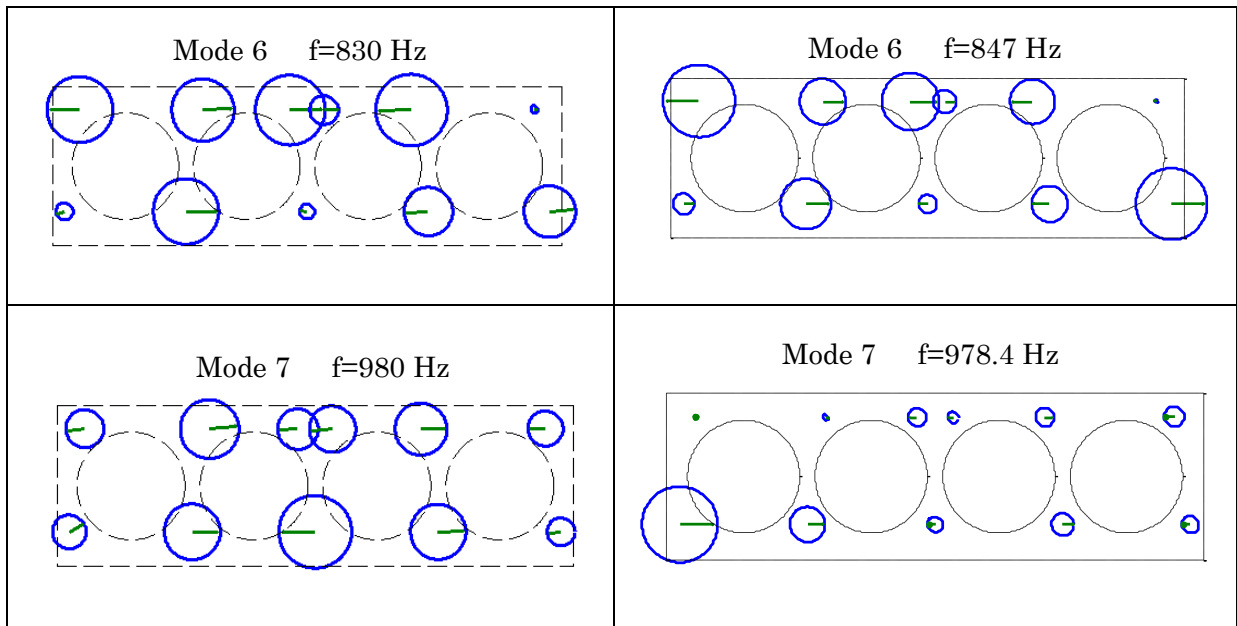


Fig.4.7 (b) Comparison of mode shapes of water coolant passage without covers

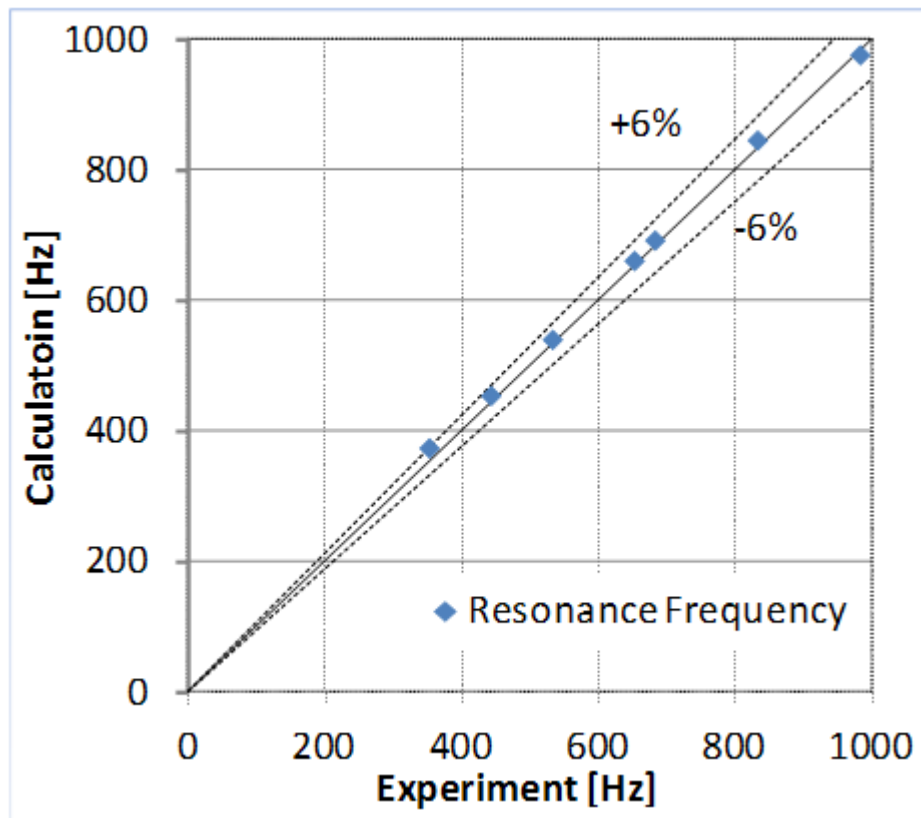


Fig.4.8 Comparison of resonance frequencies between experiment and calculation

The FEM model of coupled system of crankcase and water coolant passage is shown in Fig.4.9. The equation of motion of this coupled system is established considering the mutual interaction on the boundary. In Eq.(2.36), the modal mass and modal stiffness are obtained from the results of modal analysis of FEM models and the coupling terms are calculated by the mode shapes of crankcase and water coolant passage on the boundary. The boundary contains side walls of crankcase and four cylinders. The correspondence of interaction area of boundary between crankcase and water coolant passage is shown in Fig.4.10 (a) (b).

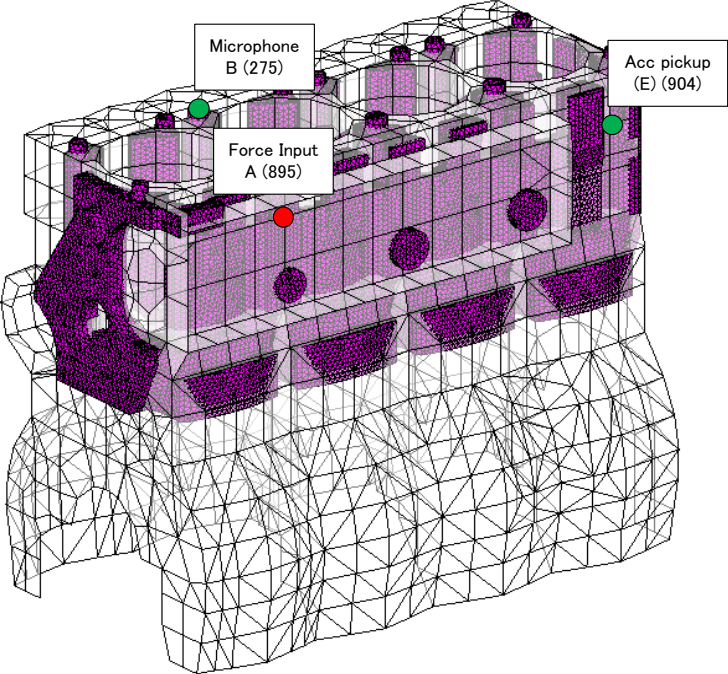


Fig.4.9 Coupled numerical model of crankcase and water coolant passage

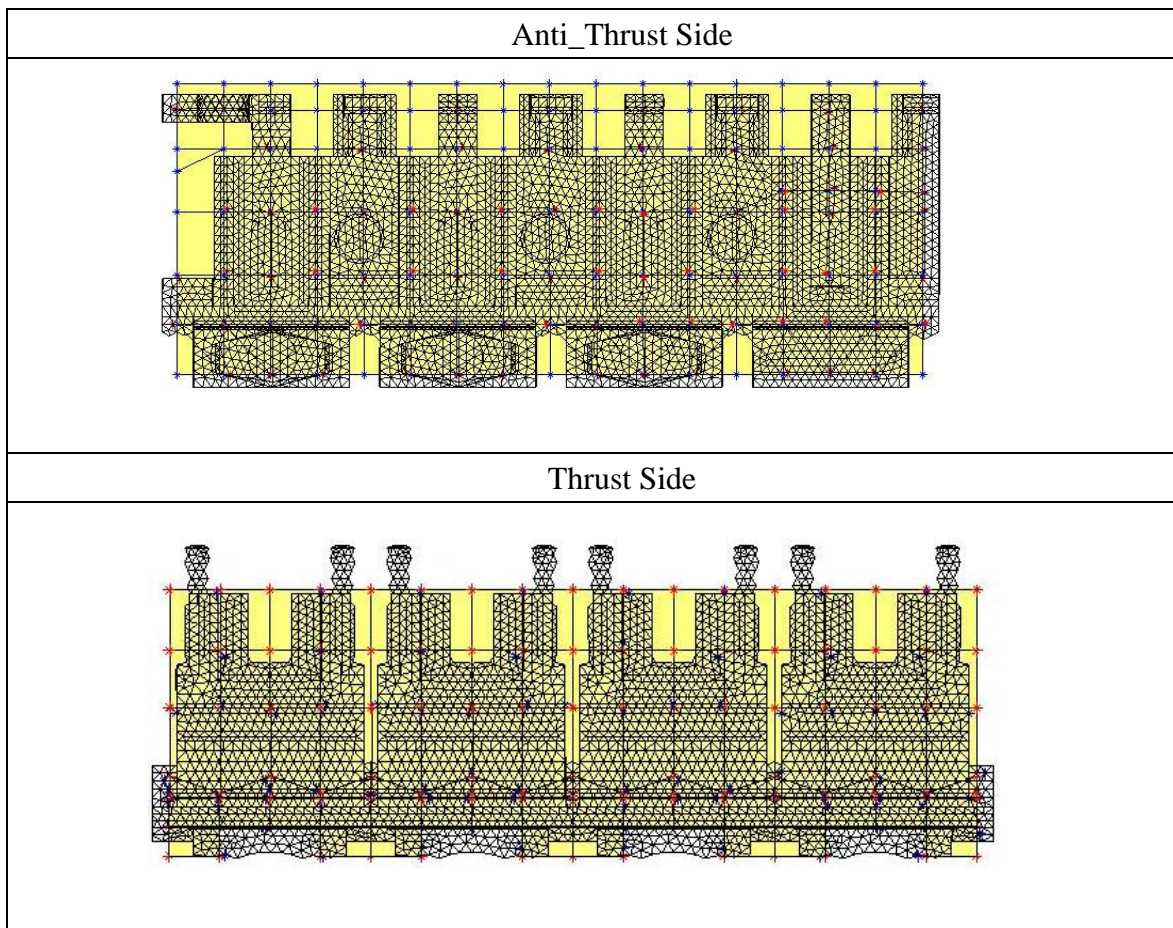


Fig.4.10 (a) Interaction area between crankcase and water coolant passage model

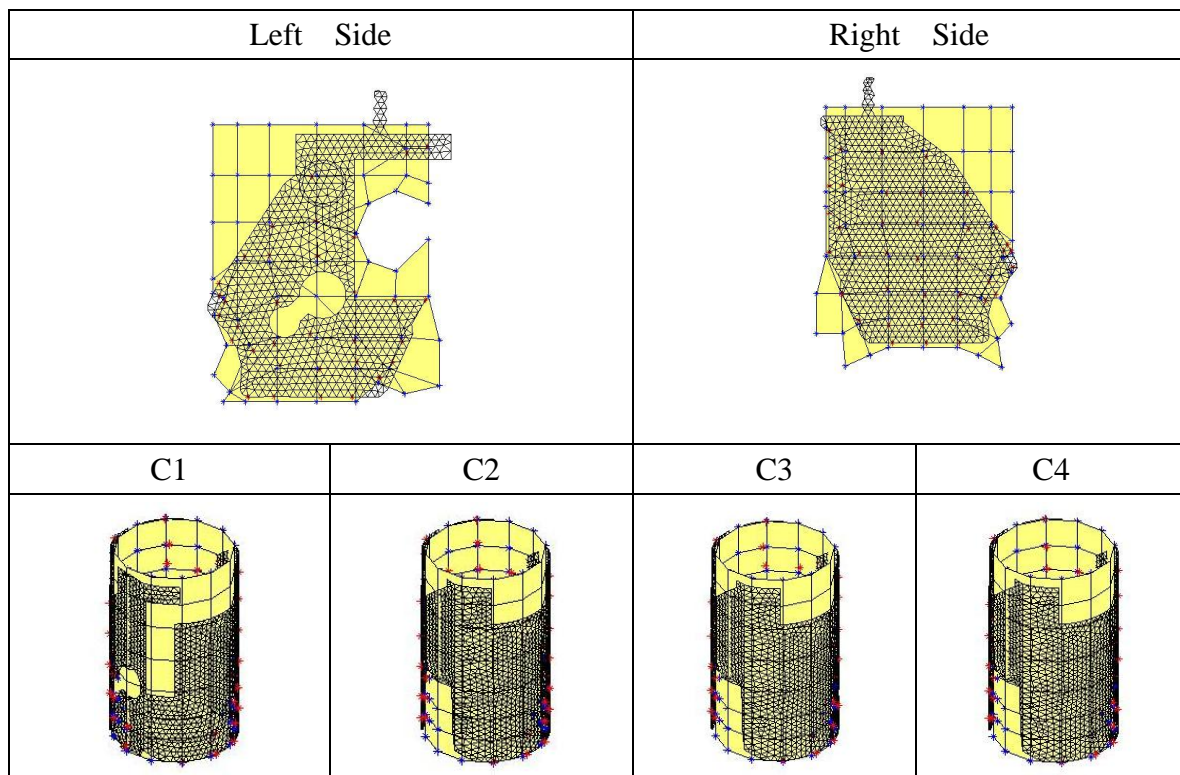
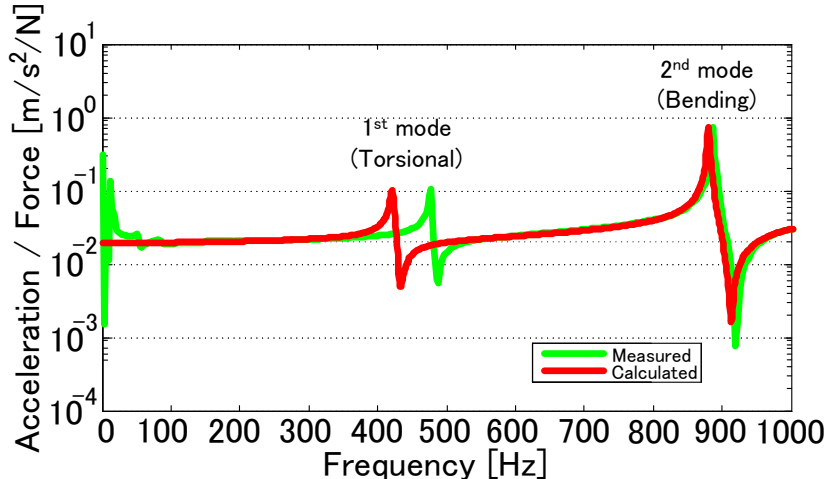
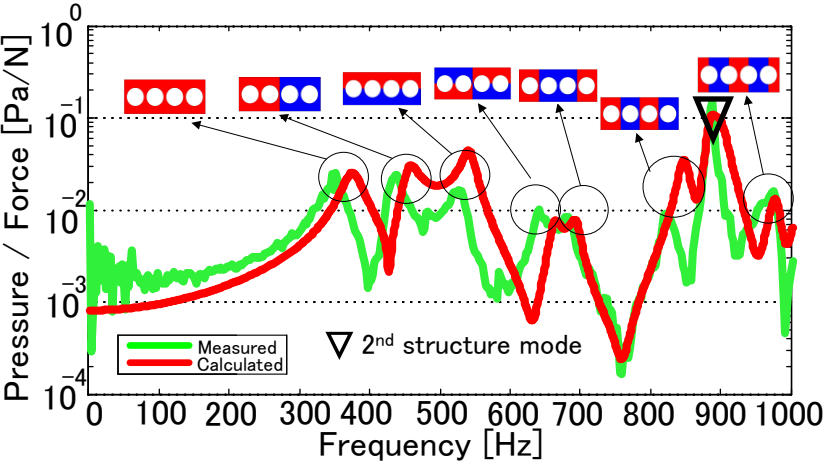


Fig.4.10 (b) Interaction area between crankcase and water coolant passage model

The comparison of measured and calculated frequency response of acceleration and pressure are shown in Fig.4.11. In the acceleration response, two dominant modes can be recognized in the frequency range of 1kHz or less, the first mode of crankcase (450Hz) is torsional deformation and the second mode of crankcase (870Hz) is bending deformation, which can be recognized in Fig.4,3. There is no peak associated with the natural frequency of the acoustic field, which implies that the effect of the acoustic field on the structural vibration is little in air. In the pressure frequency response, the seven natural frequencies of acoustic field of water coolant passage can be recognized below the frequency of 1kHz. Among the peaks, there is a peak indicating the bending mode of structure (870Hz). The analytical results of the acoustic field in water coolant passage fairly agree with the measured ones and the validity of the numerical model is confirmed.



(a) Acceleration response



(b) Pressure response

Fig.4.11 Frequency response of pressure and acceleration without covers

(3) Water coolant passage FEM model filled with water

In real conditions, the water coolant passage is filled with water coolant. The density and sound speed of acoustic field should be changed accordingly from air to water. From the equation of motion of acoustic field as shown in Appendix C, natural frequencies and modal mass of water acoustic field are converted from those of air acoustic field by changing the density ρ_A and speed of sound c_A . Mode shapes do not change in air or water medium.

Since sound speed in water varies dramatically depending on the void fraction [84], the sound speed is assumed to be in a range from 700m/s to 1500m/s based on the measurement result of speed of sound in water [85]. The natural frequencies and modal masses of water coolant passage change with sound speed and fluid density as shown in Table.4.1.

Table.4.1 Calculated natural frequencies and modal masses of water coolant passage

Air Density = 1.3kg/m ³		Water Density = 1000kg/m ³								
C= 340m/s		C=700m/s		C=1000m/s		C=1100m/s		C=1500m/s		
Mode	Frequency (Hz)	Modal mass (kg)	Frequency (Hz)	Modal mass (kg)	Frequency (Hz)	Modal mass (kg)	Frequency (Hz)	Modal mass (kg)	Frequency (Hz)	Modal mass (kg)
No.1	376	5.54525e-09	774	1.70086e-12	1106	8.33346e-13	1216	6.88718e-13	1658	3.70381e-13
No.2	456	4.42064e-09	939	1.35592e-12	1342	6.64338e-13	1476	5.49042e-13	2013	2.95265e-13
No.3	542	4.57304e-09	1163	1.40266e-12	1595	6.87241e-13	1754	5.67970e-13	2392	3.05444e-13
No.4	663	4.96867e-09	1365	1.52401e-12	1950	7.46696e-13	2145	6.17107e-13	2925	3.31869e-13
No.5	694	4.52061e-09	1429	1.38658e-12	2042	6.79362e-13	2246	5.61458e-13	3063	3.01942e-13
No.6	847	3.74268e-09	1745	1.14797e-12	2493	5.62453e-13	2742	4.64840e-13	3739	2.49982e-13
No.7	885	4.02728e-09	1822	1.23526e-12	2603	6.05224e-13	2863	5.00187e-13	3905	2.68992e-13
No.8	978	6.29610e-10	2014	1.93116e-13	2878	9.46184e-14	3166	7.81974e-14	4317	4.20532e-14
No.9	1024	1.52104e-09	2108	4.66539e-13	3012	2.28583e-13	3313	1.88913e-13	4518	1.01594e-13

4.2 Vibration characteristics of coupled system of crankcase and water coolant passage

(1) Coupled natural frequencies

The eigenvalue analysis is carried out to investigate the characteristics of coupled system. The distribution of natural frequencies of crankcase structure, acoustic field of water coolant passage (WCP) and the coupled system at different sound speed of water are compared in Fig.4.12~Fig.4.14. Vertical circle of the coupled system is the peak frequency of the water pressure fluctuation induced by piston slap force as discussed in §4.3. The mode shapes of coupled system ϕ'_n and ψ'_n are calculated by Eq.(2.21) as linear combination of uncoupled mode shapes ϕ_n and ψ_n .

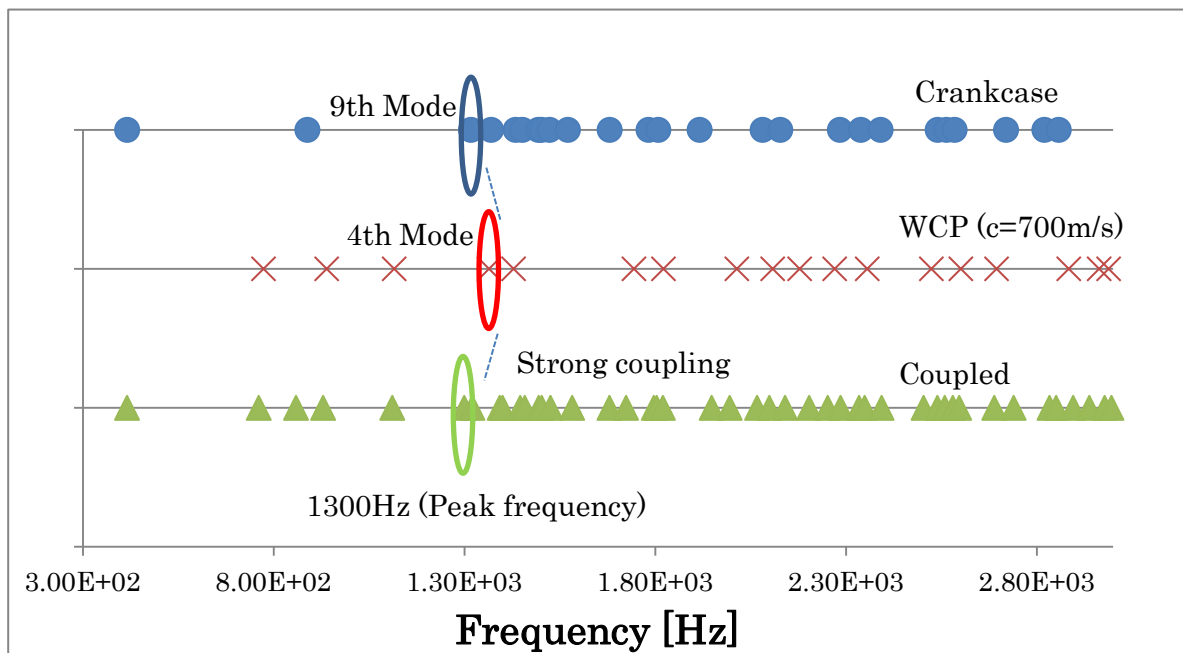


Fig.4.12 Frequency distribution of crankcase, acoustic field (c=700m/s) and coupled system

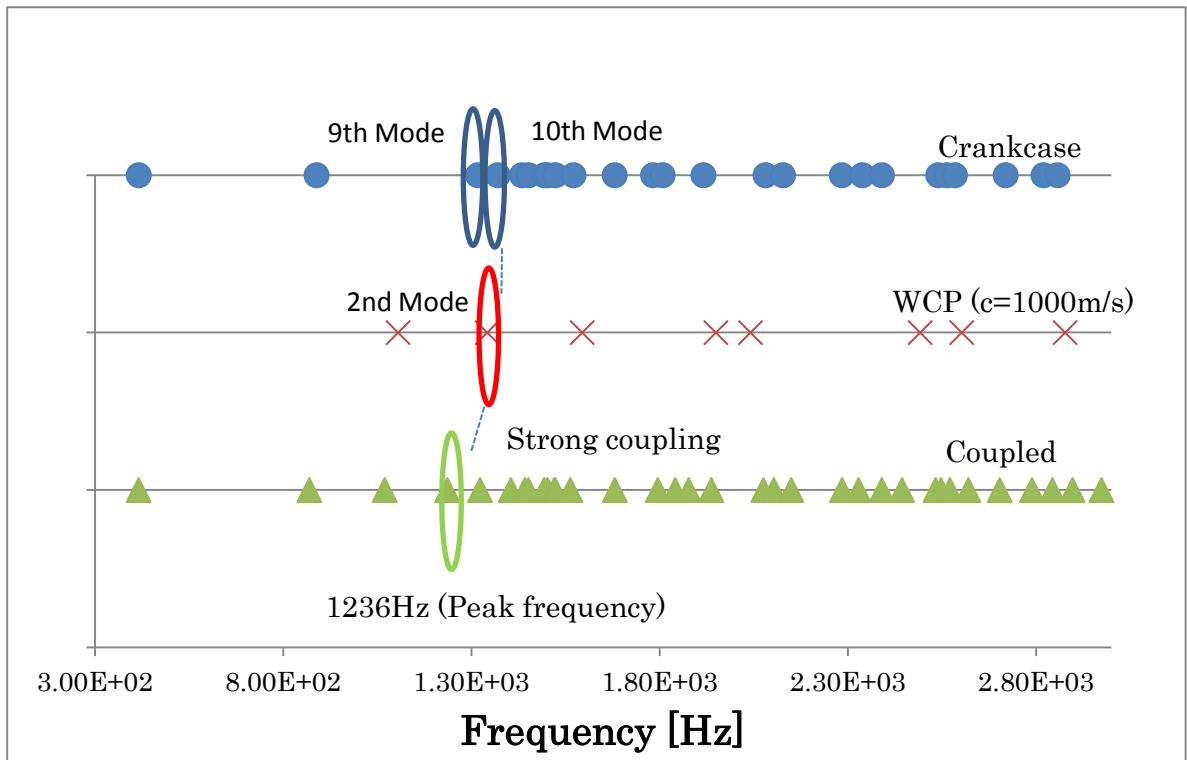


Fig.4.13 Frequency distribution of crankcase, acoustic field ($c=1000\text{m/s}$) and coupled system

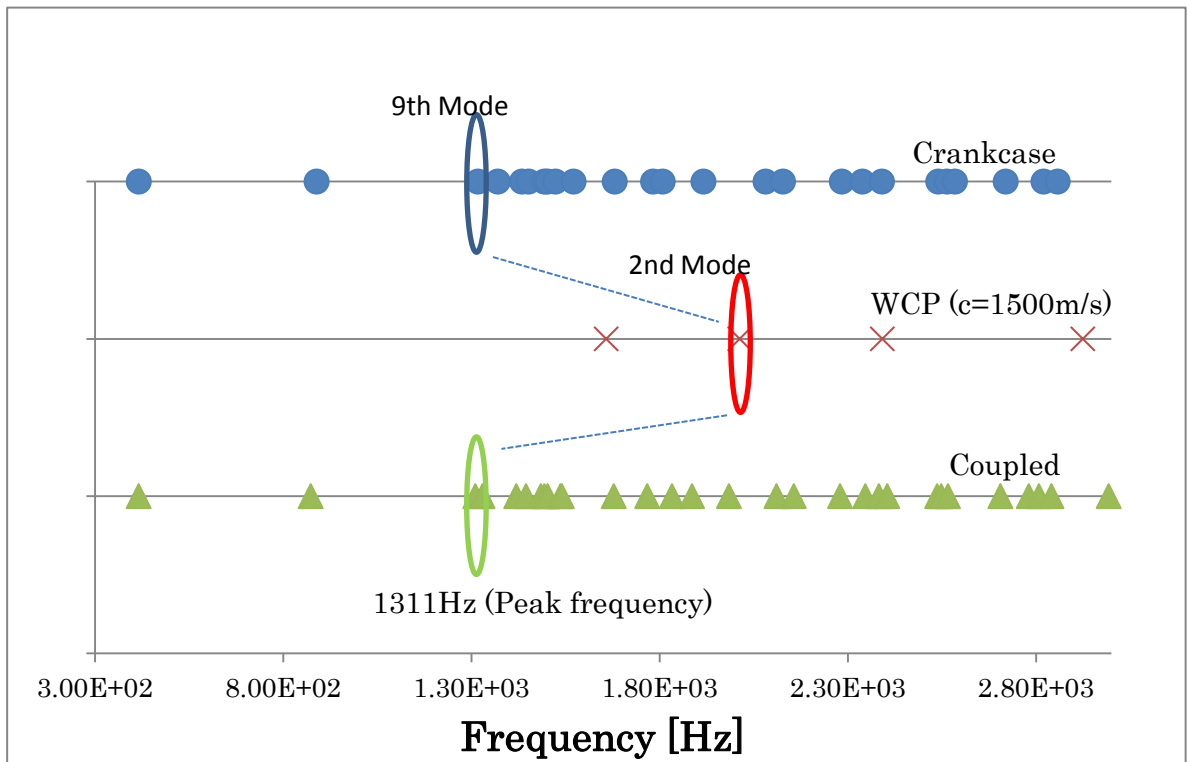


Fig.4.14 Frequency distribution of crankcase, acoustic field ($c=1500\text{m/s}$) and coupled system

(2) Coupled mode shapes

The coupled mode shapes are calculated as combination of eigenmode shapes as shown in Eq.(2.21). Fig.4.15, Fig.4.17 and Fig.4.19 show overall view and a cross-sectional view of the coupled mode shape of crankcase and water acoustic field at the frequency of around 1300Hz when the speed of sound changes $c= 700, 1000, 1500$ m/s. These frequencies are the peak frequency of piston slap induced water pressure at each sound speed of water, which are discussed in §4.3.

Certain eigenmode shapes of crankcase and water acoustic field dominate the coupled mode shapes of crankcase and water acoustic field, respectively. Fig.4.16 shows that at sound speed 700m/s the 9-th crankcase eigenmode and 4-th water acoustic field eigenmode contribute mostly to the pressure fluctuation. Fig.4.18 shows that at sound speed 1000m/s the 9-th and 10-th crankcase eigenmodes and 2nd water acoustic field eigenmode contribute mostly to the pressure fluctuation. Fig.4.20 shows that at sound speed 1500m/s the 9-th crankcase eigenmode and 2nd water acoustic field eigenmode contribute mostly to the pressure fluctuation. Among all the eigenmode shapes, the 9-th, 10-th crankcase modes and the 2nd, 4-th water acoustic field modes contribute mostly.

Acceleration mode shape of crankcase

Pressure mode shape of W.C.P.

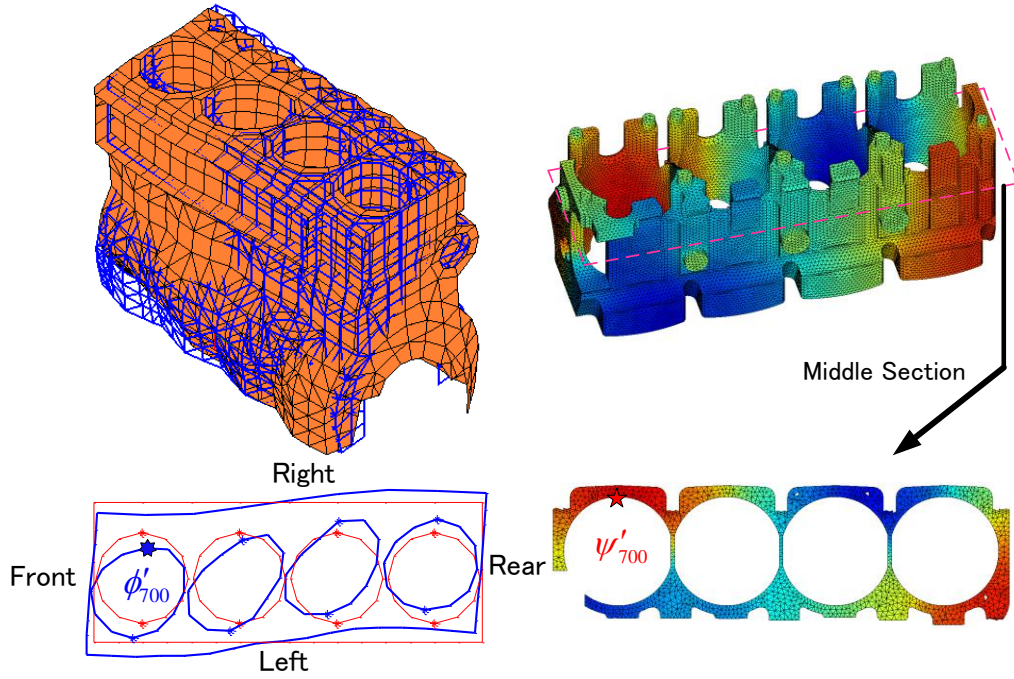


Fig.4.15 Coupled mode shapes at $f=1300\text{Hz}$ ($c=700\text{m/s}$)

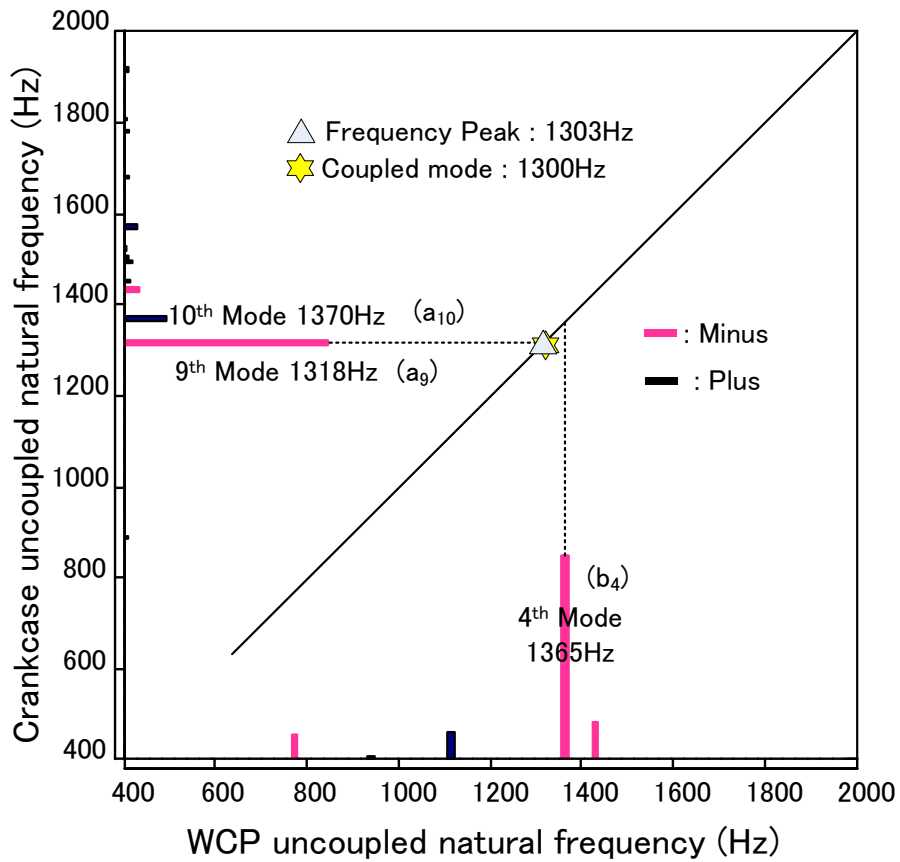


Fig.4.16 Contribution of uncoupled modes to coupled mode of 1300Hz ($c=700\text{m/s}$)

Acceleration mode shape of crankcase

Pressure mode shape of W.C.P.

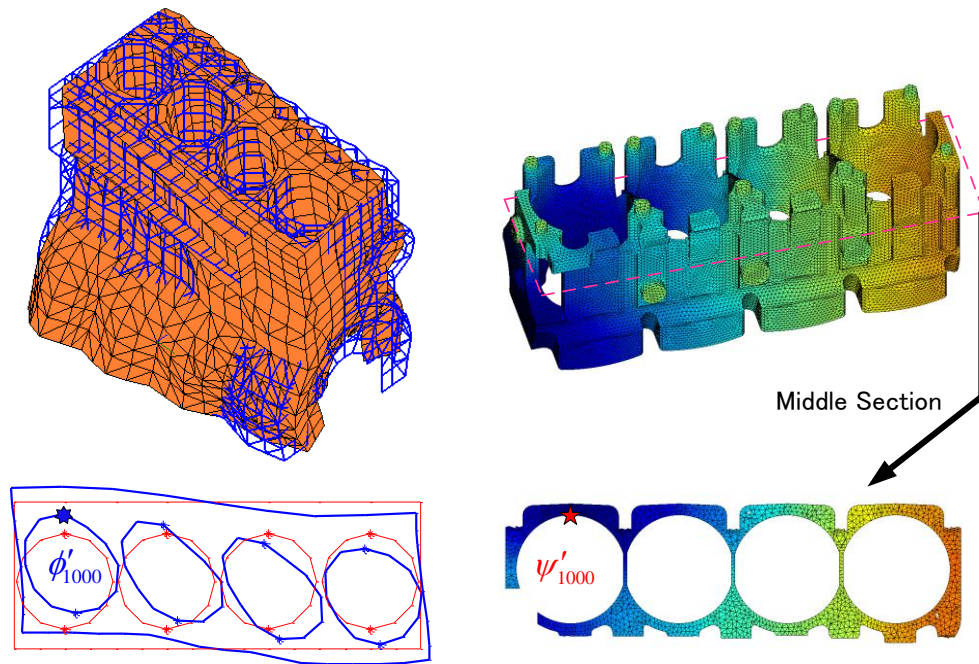


Fig.4.17 Coupled mode shapes at $f=1236\text{Hz}$ ($c=1000\text{m/s}$)

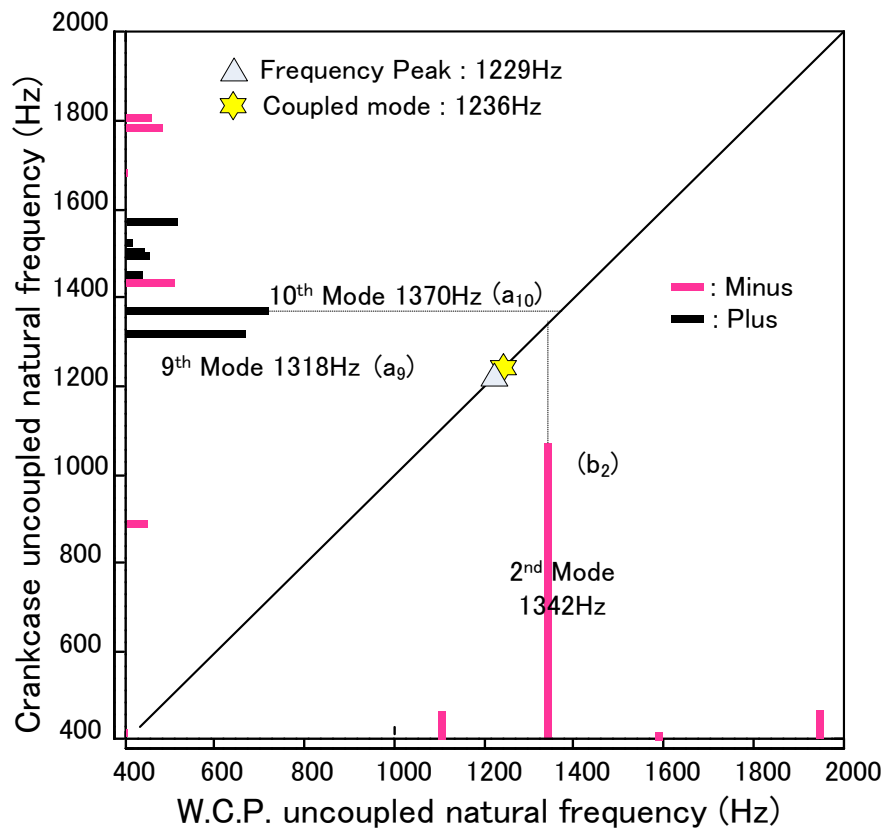


Fig.4.18 Contribution of uncoupled modes to coupled mode of 1236.3Hz ($c=1000\text{m/s}$)

Acceleration mode shape of crankcase

Pressure mode shape of W.C.P.

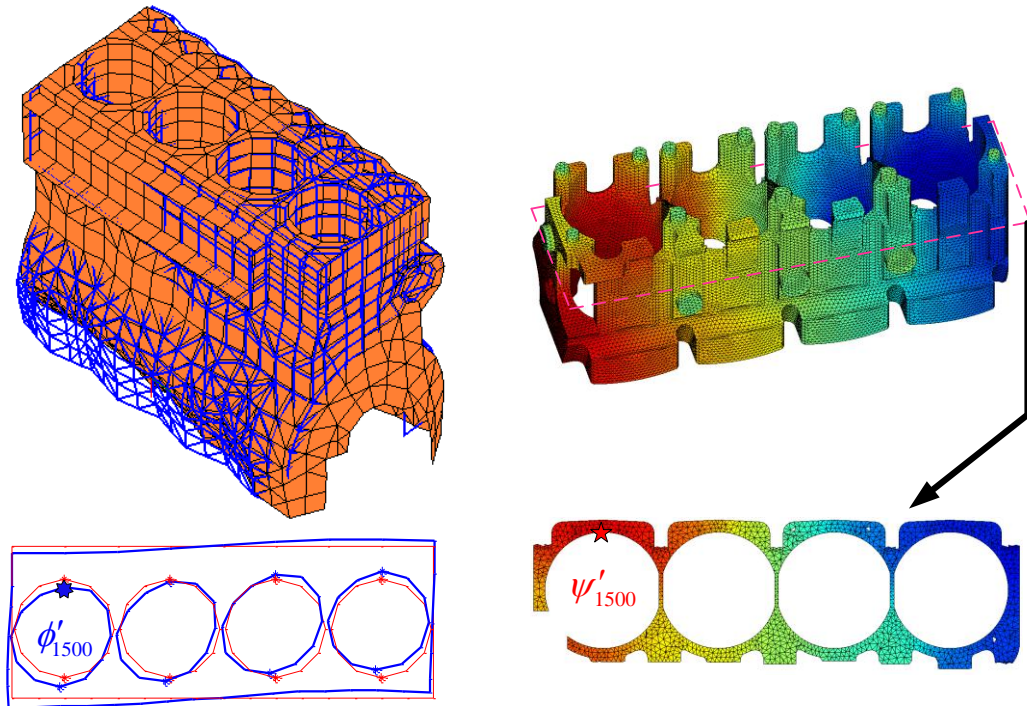


Fig.4.19 Coupled mode shapes at $f=1311\text{Hz}$ ($c=1500\text{m/s}$)

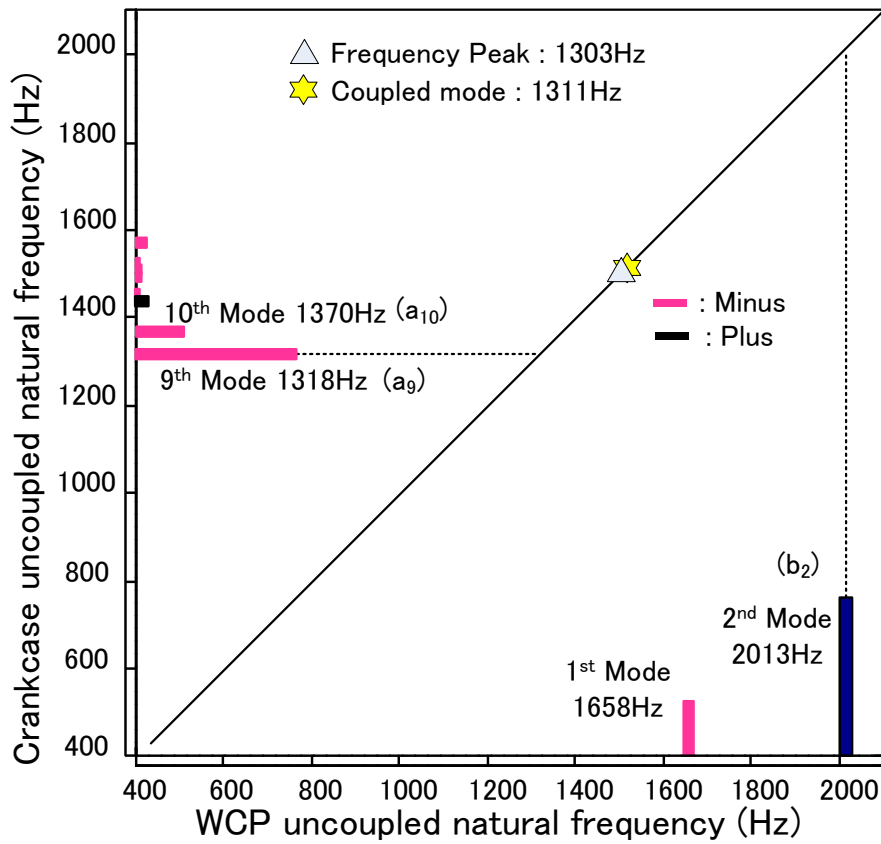


Fig.4.20 Contribution of uncoupled modes to coupled mode of 1311Hz ($c=1500\text{m/s}$)

4.3 Calculation of pressure fluctuation induced by piston slap force

The degrees of cavitation erosion of different cylinders in the same internal combustion engine are not in same level. This phenomenon is considered from the perspective of vibration characteristics of engine structure containing cylinders and the pressure mode shapes of water coolant passage. As discussed in the last chapter, the sound speed of water changes with the void fraction of the coolant. The natural frequencies of water acoustic field vary with the sound speed and the pressure fluctuation is affected by the natural frequencies of water acoustic field.

In this section, the vibration characteristics of coupled system and the amplitude of pressure fluctuation induced by piston slap force are calculated at different sound speed in water. The piston slap force is applied on each cylinder respectively and the differences of the amplitude of pressure fluctuation are discussed.

(1) Piston profile and clearance

The numerical procedure of determining piston slap forces has been developed by K. Ohta [83][84]. The amplitude of piston slap forces is determined by factors such as piston and liner clearance, combustion pressure, etc. Piston slap force is calculated on the full load in which maximum cylinder pressure is 104 atm and clearance between piston and liner is 0.2mm. Figure 4.21 (a) shows forces acting on the piston and Fig.4.21 (b) shows piston profile and liner clearance. Fig.4.22 shows the calculated piston slap forces of each cylinder determined by combustion sequence #1—#3—#4—#2.

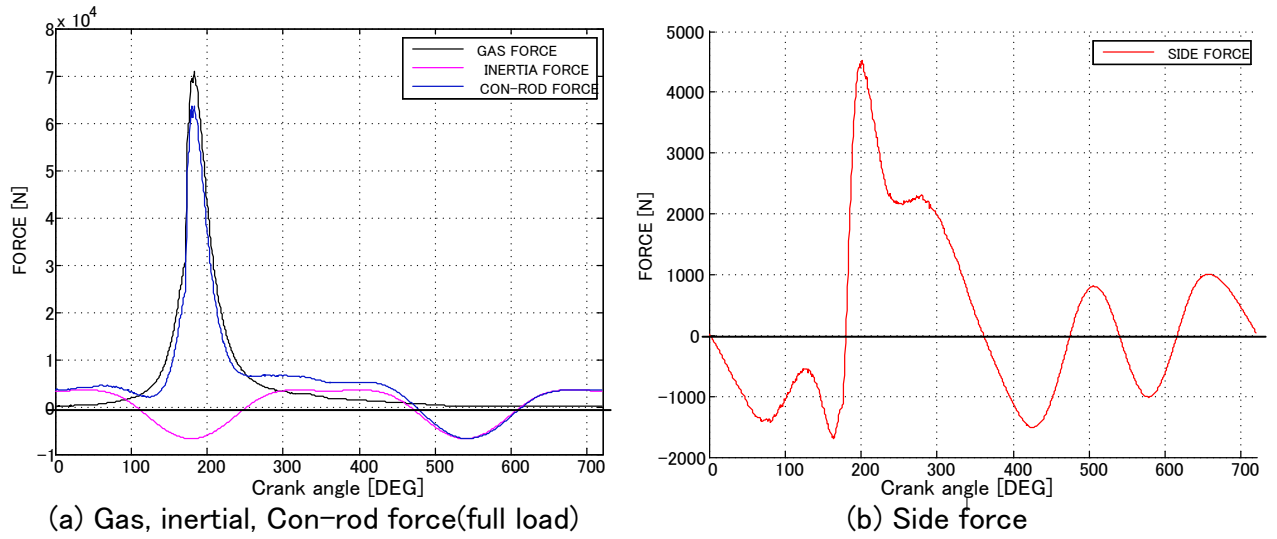


Fig.4.21 (a) Forces acting on piston

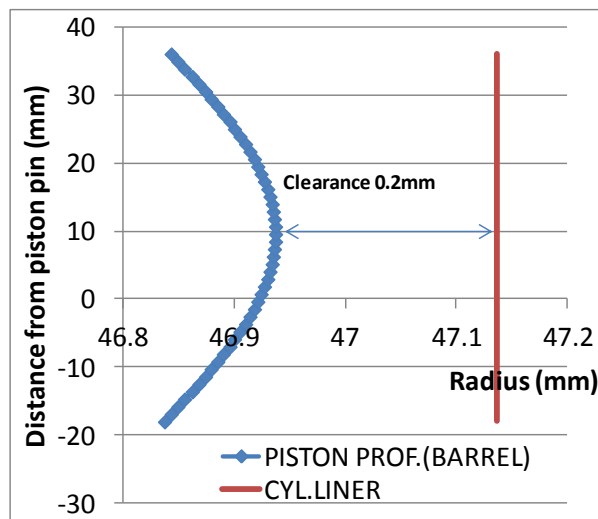


Fig.4.21 (b) Piston profile and clearance

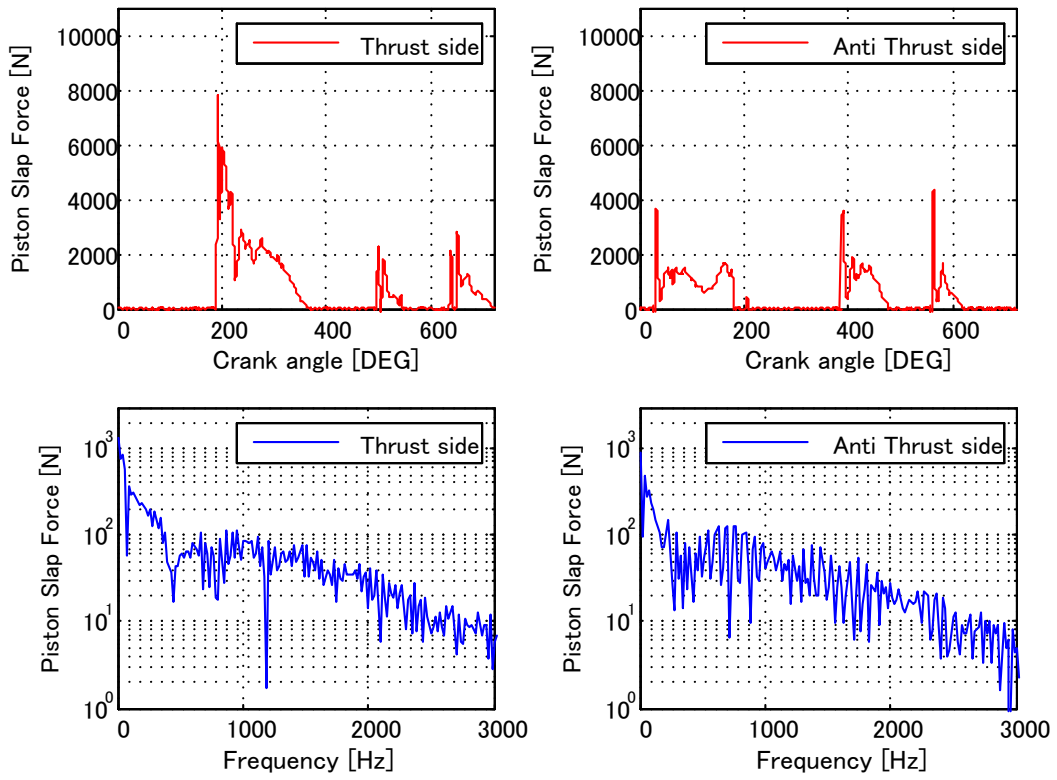


Fig.4.22 (a) Piston slap forces of #1 cylinder

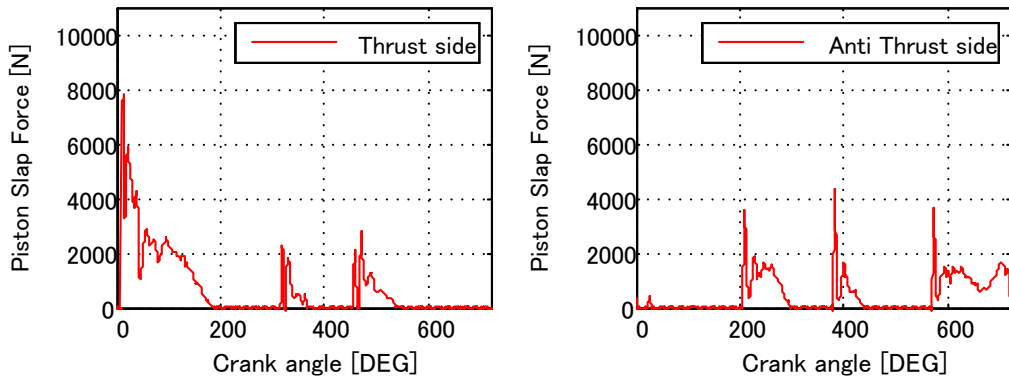


Fig.4.22 (b) Piston slap forces of #2 cylinder

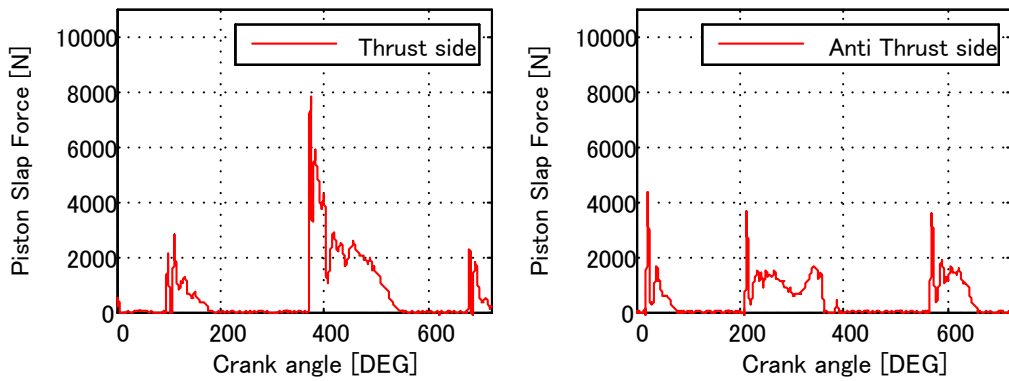


Fig.4.22 (c) Piston slap forces of #3 cylinder

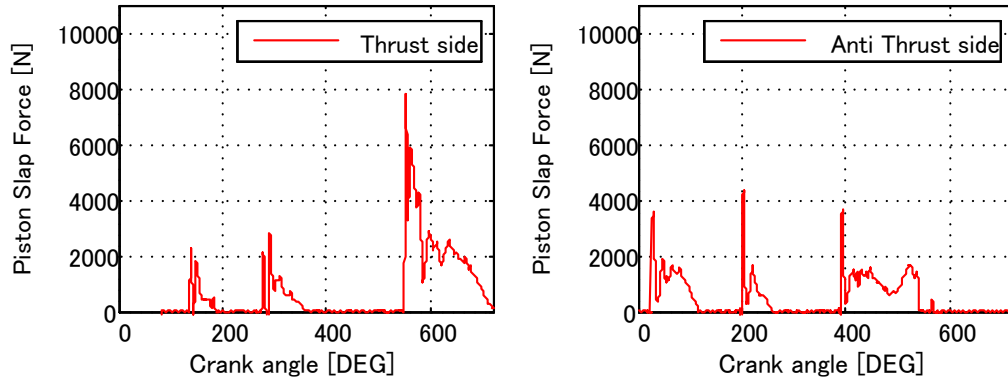


Fig.4.22 (d) Piston slap forces of #4 cylinder

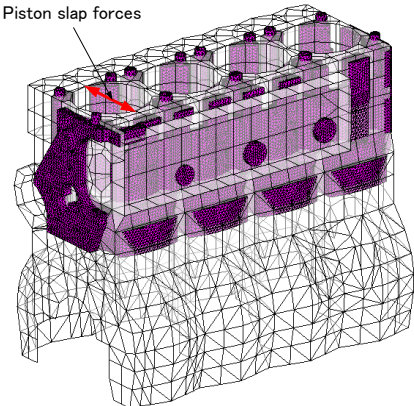
(2) Water pressure fluctuation induced by piston slap force at #1 cylinder

When piston slap force acts on #1 cylinder of the coupled system as shown in Fig.4.23, pressure fluctuation and acceleration at thrust and anti-thrust side of #1 cylinder wet surface are calculated at different water sound speed as shown in Fig.4.24~Fig.4.26. Figures shows the waveform and frequency spectrum. The maximum amplitudes of negative pressure at thrust side $|P_{\max}|$ changing with sound speed are shown in Fig.4.27. Figure 4.28 represents time averaged mean squared pressure $\langle P^2 \rangle$ at different sound speed. The maximum negative pressure is seen in the case of water sound speed $c=1000\text{m/s}$.

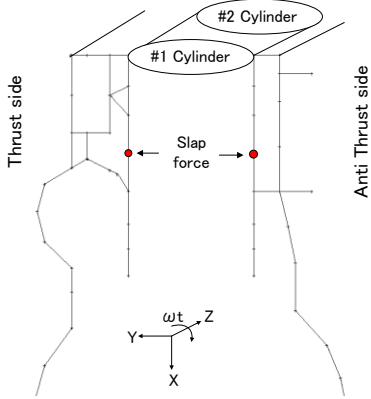
As described in Fig.4.24~Fig.4.26, the peak frequency of pressure spectrum changes with sound speed. The frequency spectrum is calculated based on the coupled modes. The peak of frequency spectrum reflects the coupled mode with maximum influence. The frequency peaks at sound speed $c=700\text{m/s}$, 1000m/s and $c=1500\text{m/s}$ are 1303Hz , 1229Hz and 1303Hz , respectively. Figure 4.15, Figure 4.17 and Figure 4.19 shows the corresponding coupled mode shapes of the frequency peaks at different sound speed. Generally, the 9-th and 10-th crankcase eigenmodes and the 2nd and 4-th water acoustic field eigenmodes have the largest influence. At sound speed $c=700\text{m/s}$, the contributions of 9-th crankcase eigenmode and 4-th water acoustic field eigenmode are the largest to the pressure fluctuation. At sound speed $c=1000\text{m/s}$, the contributions of 9-th and 10-th crankcase eigenmodes and 2nd water acoustic field eigenmode

are the largest to the pressure fluctuation. At sound speed $c=1500\text{m/s}$, the contributions of 9-th crankcase eigenmode and 2nd water acoustic field eigenmode are the largest to the pressure fluctuation.

The 9-th crankcase eigenmode (natural frequency 1318Hz) is twisted mode as shown in Fig.4.3, which indicates that the #1 and #2 cylinders vibrate oppositely to #3 and #4 cylinders in left and right direction. The 2nd water acoustic field eigenmode suggests that the phase of pressure of #1 and #2 cylinders is opposite to those of #3 and #4 cylinders. The natural frequency of 2nd water acoustic field mode is 939Hz at $c=700\text{m/s}$, 1342Hz at $c=1000\text{m/s}$ and 2013Hz at $c=1500\text{m/s}$. The 4th water acoustic field mode shows that the half wavelength mode of standing wave can be recognized both in front-rear direction and left-right direction. The natural frequency of 4th mode is 1365Hz at $c=700\text{m/s}$, 1950Hz at $c=1000\text{m/s}$ and 2925Hz at $c=1500\text{m/s}$.

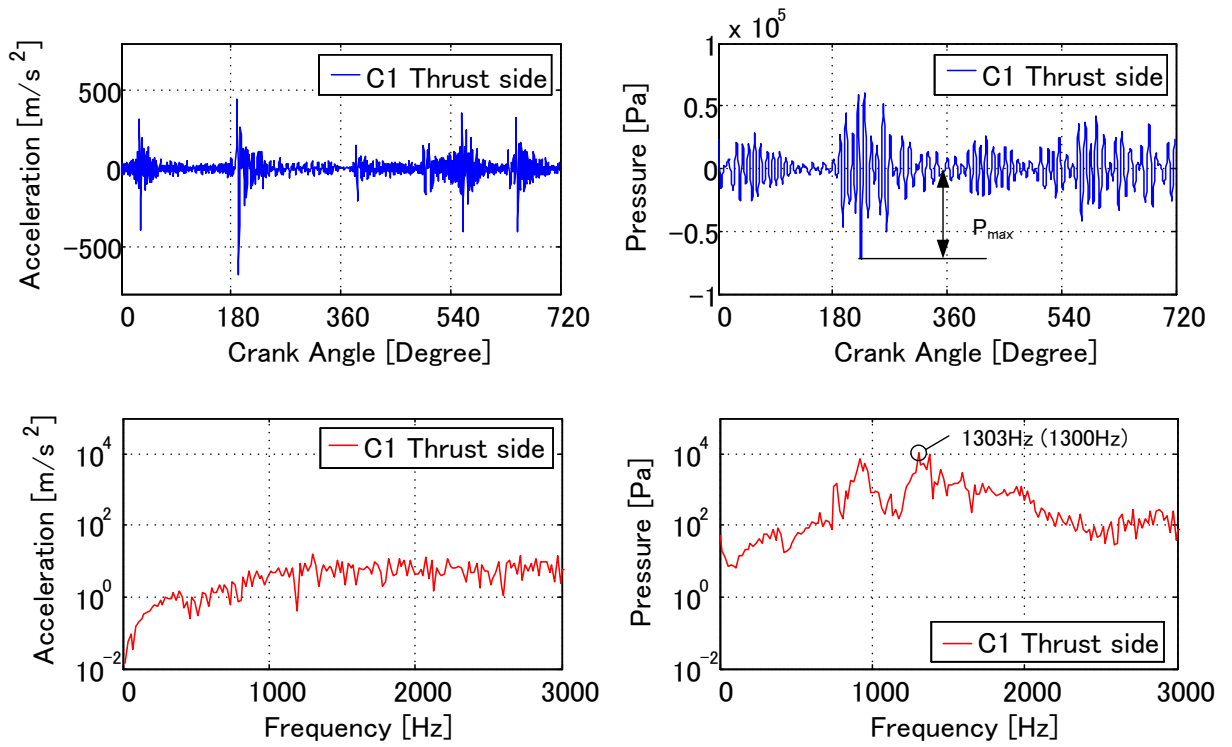


(a) Coupled system of crankcase and water coolant passage

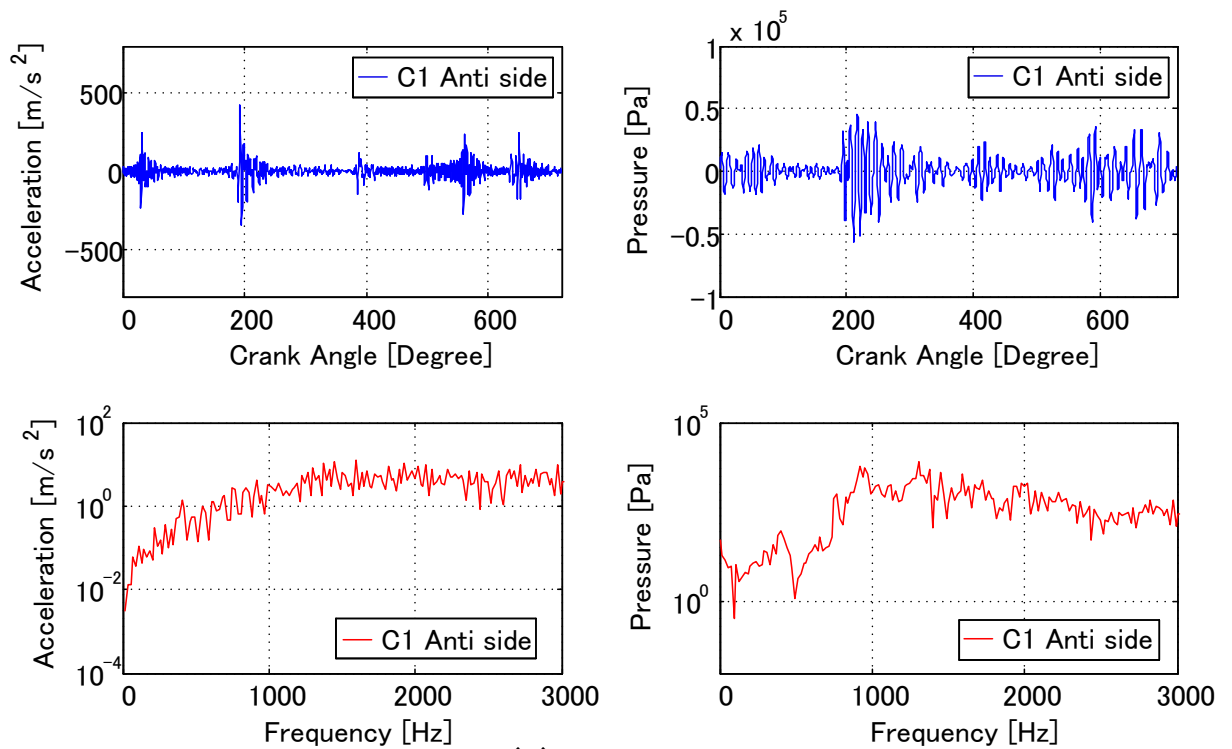


(b) Application points of slap forces

Fig.4.23 Application points of piston slap forces (Thrust and Anti Thrust side of cylinders)

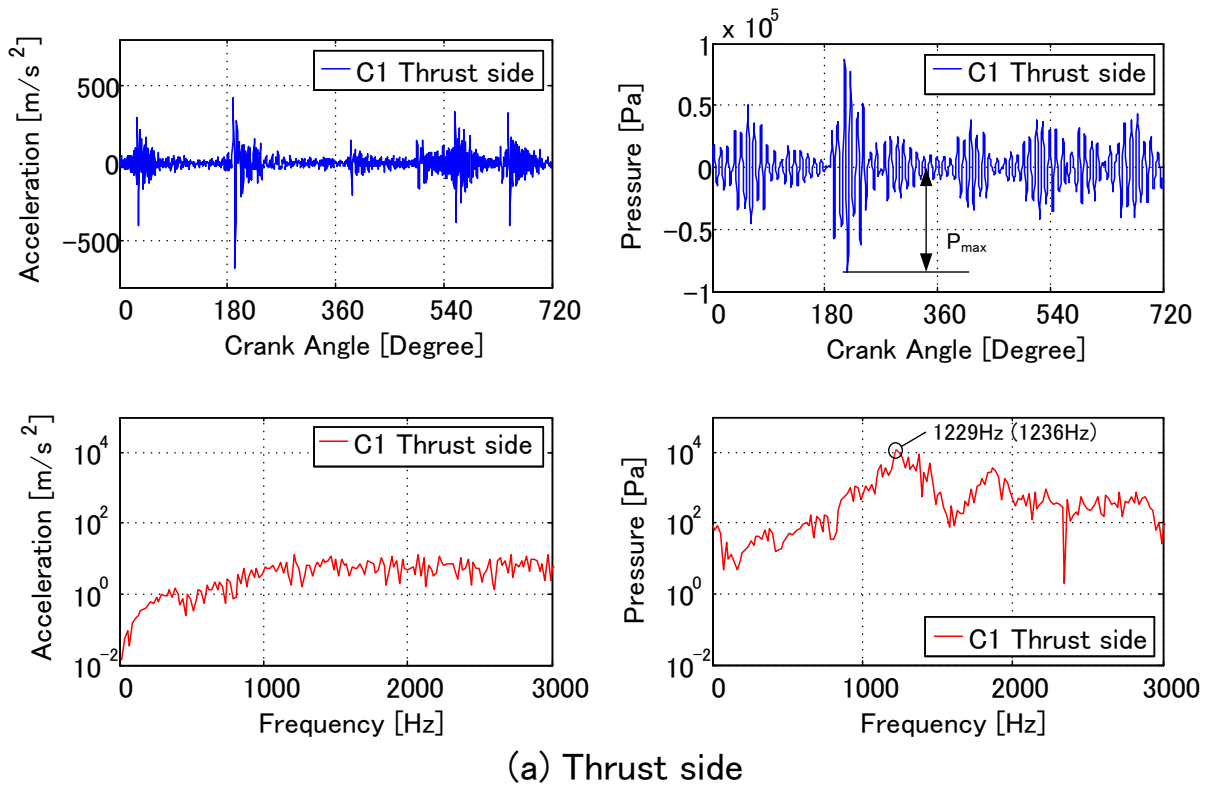


(a) Thrust side

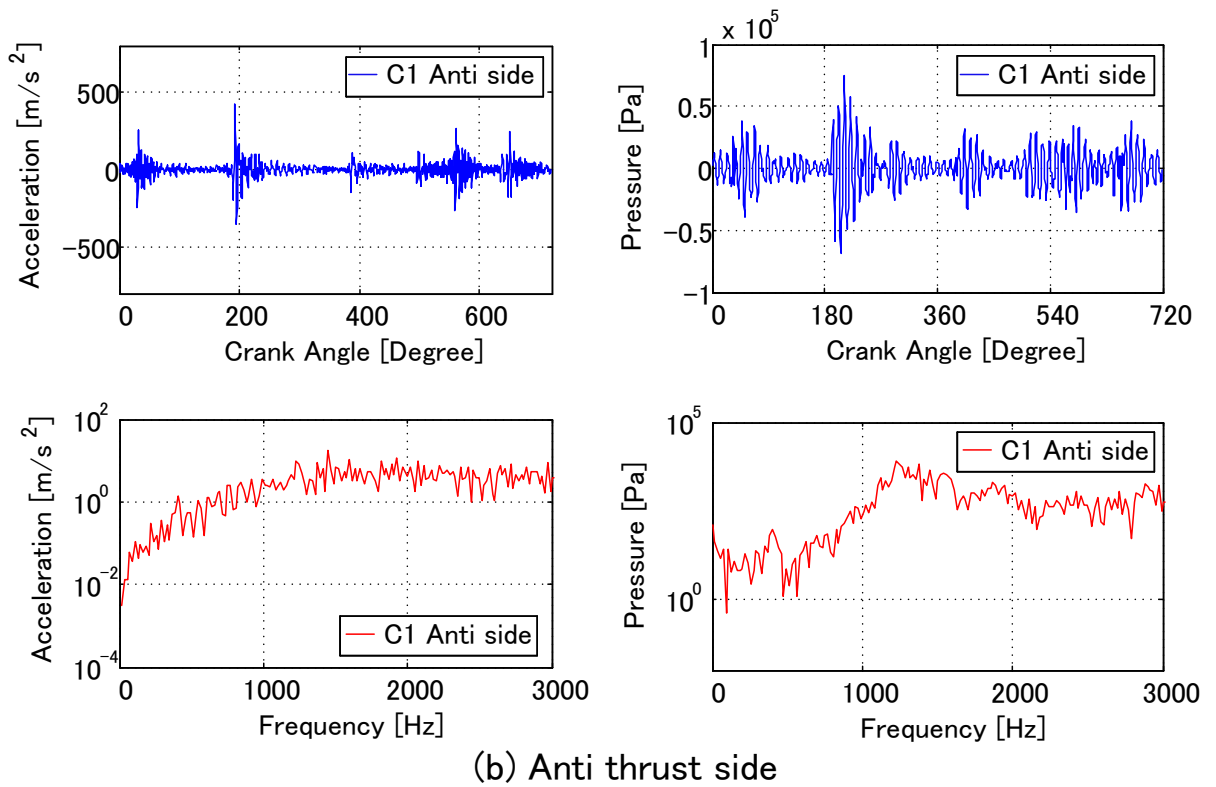


(b) Anti thrust side

Fig.4.24 Waveform and frequency spectrum of pressure and acceleration at $c=700m/s$

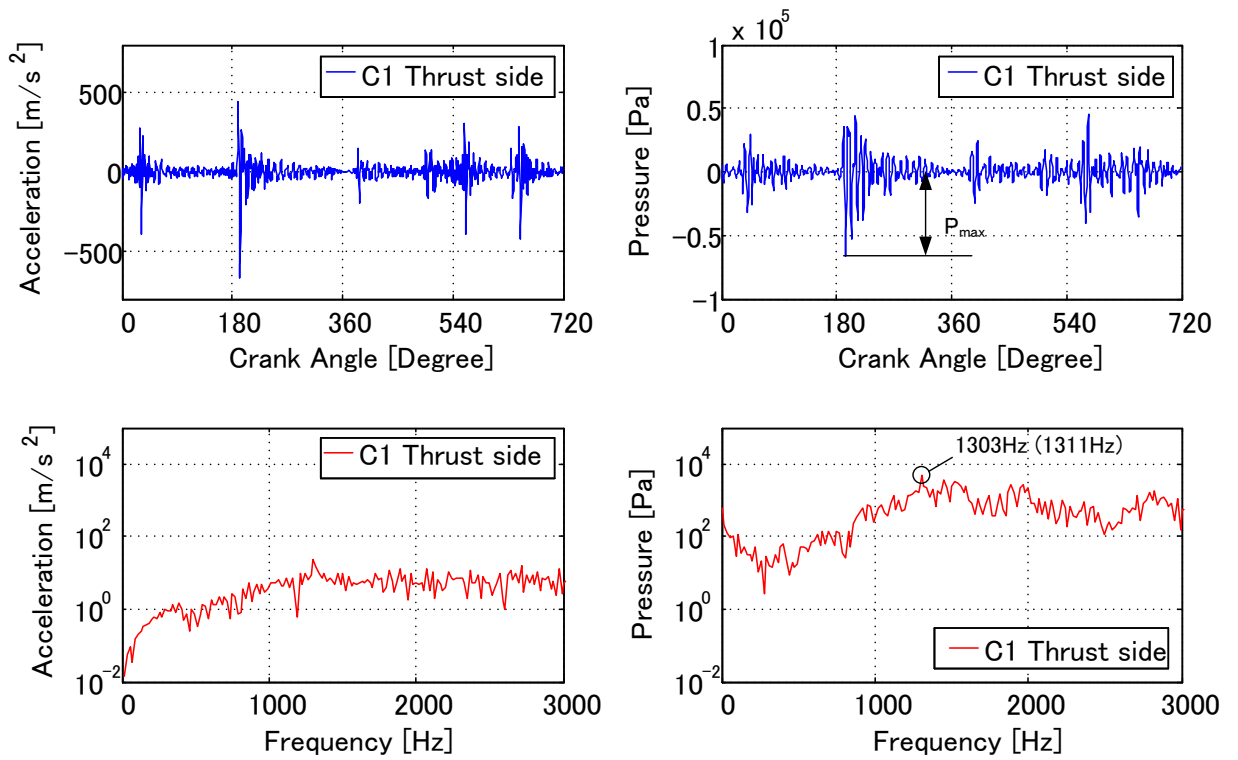


(a) Thrust side

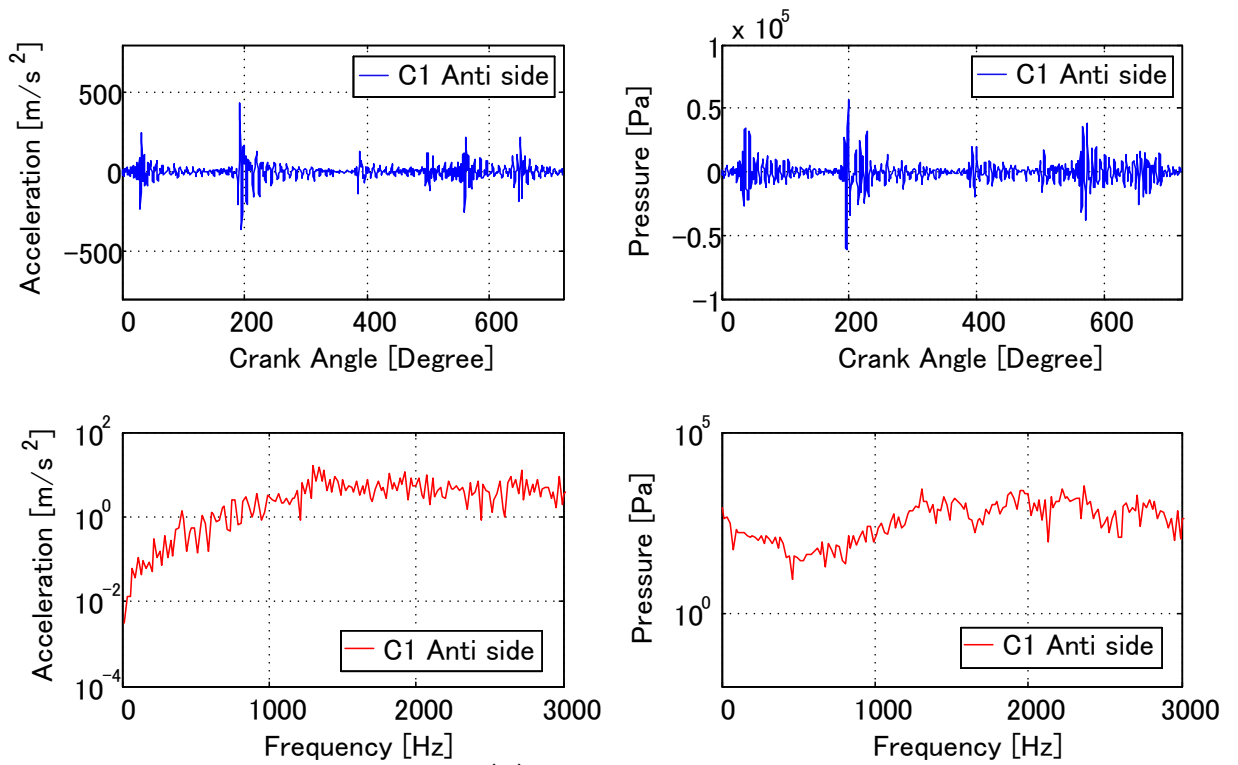


(b) Anti thrust side

Fig.4.25 Waveform and spectrum of pressure and acceleration at 1000m/s



(a) Thrust side



(b) Anti thrust side

Fig.4.26 Waveform and spectrum of pressure and acceleration at 1500m/s

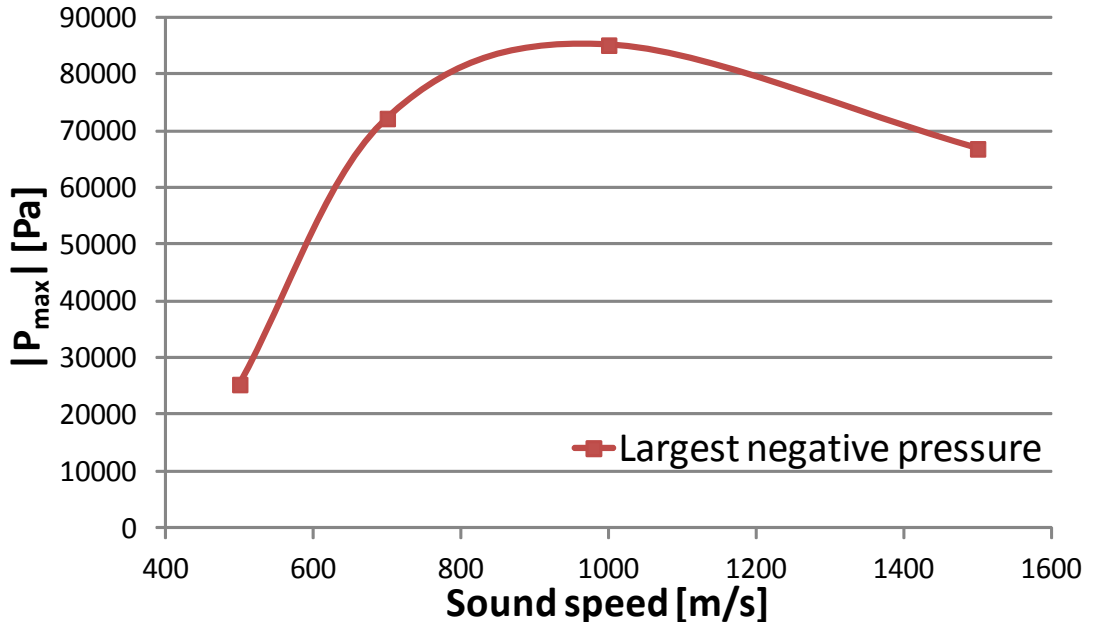


Fig.4.27 Maximum pressure fluctuation under different sound speed

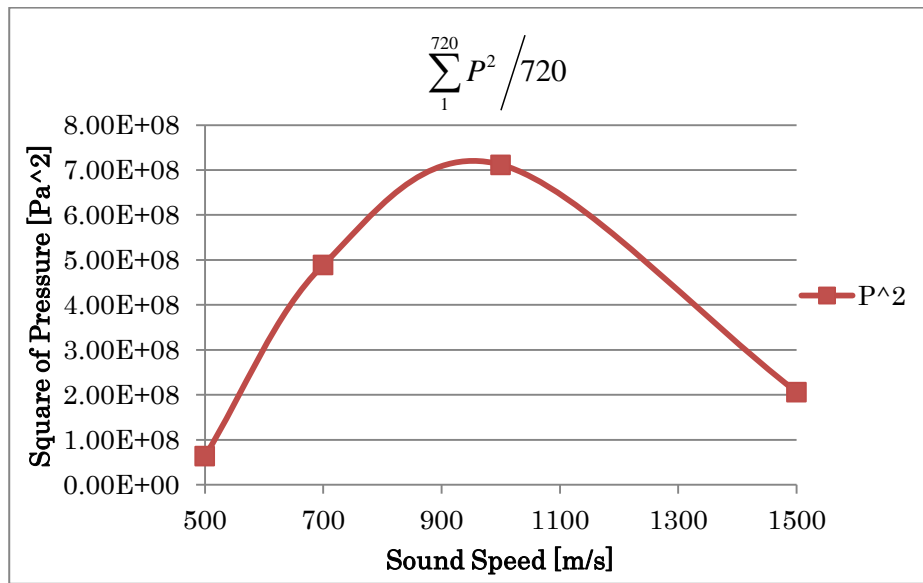


Fig.4.28 Square of pressure fluctuation under different sound speed

Assuming that the external force f_q equals 1N and vibration frequency equals the natural frequency of coupled system $(\omega = \omega'_n)$, the pressure of n-th coupled mode at the liner wet surface induced by unit force is obtained by Eq.(2.42). Figure 4.29 shows comparison of the water pressure amplitude, driven by unit force, at the peak frequencies shown in

Fig.4.24~Fig.4.26, when the sound speed of water changed. At sound speed 1000m/s, the pressure induced by unit force is largest.

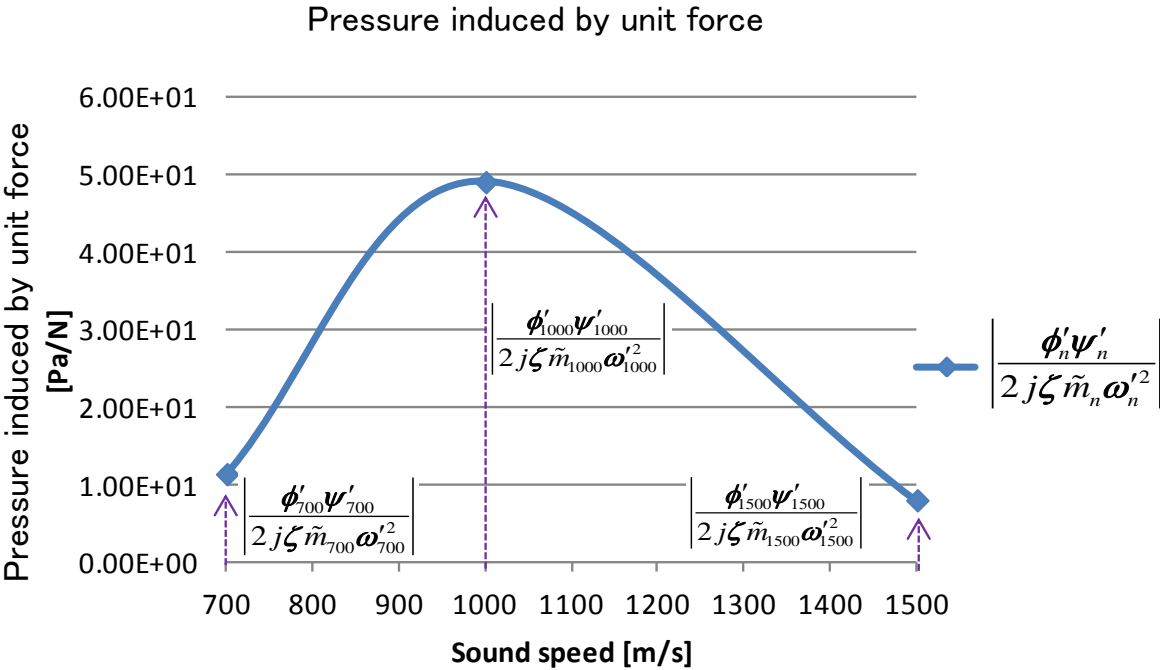


Fig.4.29 Pressure of crankcase induced by unit force

From frequency spectra shown in Fig.4.24~Fig.4.26, the frequency peaks are 1303Hz at $c=700\text{m/s}$, 1229Hz at $c=1000\text{m/s}$ and 1303Hz at $c=1500\text{m/s}$, which correspond to the natural frequency of the coupled modes of 1300Hz, 1236.3Hz and 1311Hz, respectively, as shown in Fig.4.15, Fig.4.17 and Fig.4.19. The amplitude of negative pressure is mainly determined by these coupled modes. The modal responses of a'_n and b'_n in Eq.(2.21) represent the contribution of uncoupled modes to the n -th coupled mode. The contributions of uncoupled modes to the coupled modes of 1300Hz at $c=700\text{m/s}$, 1236.3Hz at $c=1000\text{m/s}$ and 1311Hz at $c=1500\text{m/s}$ are shown in Fig.4.16, Fig.4.18 and Fig.4.20. Figure 4.18 shows that at $c=1000\text{m/s}$ the 9-th and 10-th crankcase mode and the 2nd water coolant passage mode contribute mostly to the coupled mode of 1236.3Hz. For the pressure fluctuation has maximum amplitude at sound speed 1000m/s, the 9-th and 10-th crankcase mode and 2nd water coolant passage mode are also most influential to the amplitude of pressure fluctuation. In Eq.(2.18) the coupling term

$\Psi_B^t S \Phi_B$ represents the degree of coupling between a certain structure vibration mode and a certain acoustic mode. The larger the coupling term, the higher the potential of large pressure fluctuation will exist. Figure 4.30 shows that the coupling term between 10-th crankcase mode and 2nd water coolant passage mode is largest, which indicates that the coupling effect between 10-th crankcase mode and 2nd water coolant passage mode is the most significant. Another factor that affects pressure fluctuation is the proximity of natural frequencies of crankcase and acoustic field of water coolant passage. When the natural frequency of water acoustic field approaches to the natural frequency of crankcase mode, larger pressure fluctuation is anticipated, just as the case of 2nd water coolant passage mode at sound speed 1000m/s (1342Hz) coupled with 10-th crankcase mode (1370Hz). The natural frequency of 2nd water coolant passage mode at sound speed 1000m/s is closest to the natural frequency of 10-th crankcase mode comparing with other sound speeds as shown in Fig.4.12~Fig.4.14. The larger coupling terms combining with the proximity of natural frequencies of crankcase and water coolant passage result in larger pressure fluctuation as shown in Fig4.27 and Fig.4.28.

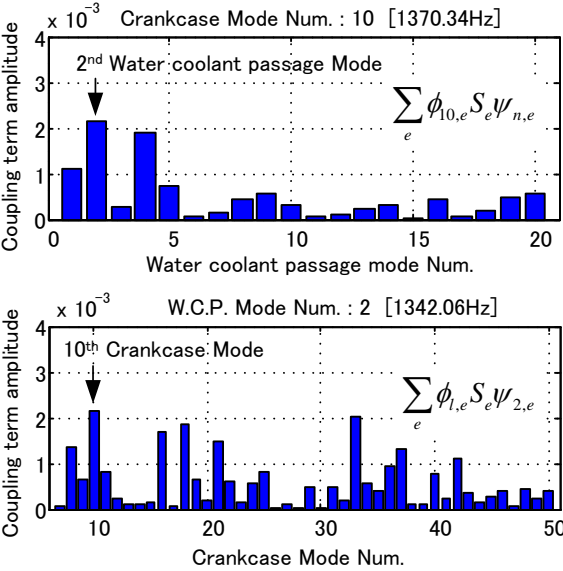


Fig.4.30 Coupling terms between 10-th crankcase mode and water coolant passage modes

(3) Pressure fluctuation at different cylinders

In reality, the degree of cavitation erosion varies from cylinder to cylinder within the same

engine, which suggests that pressure fluctuations at different cylinders are not in same level. Cylinders are supposed to be under the action of same piston slap forces with different ignition timing as shown in Fig.4.22. When piston slap forces act on each cylinder, respectively, the pressure fluctuation at the thrust side of the corresponding cylinder is calculated as shown in Fig.4.31. The largest negative pressure of four cylinders appears at different ignition timing. The absolute values of largest negative pressure $|P_{\max}|$ of four cylinders are shown in Fig.4.32. The pressure fluctuation at #1 cylinder is largest followed by #4 cylinder, which implies that cavitation erosion is easier to happen on #1 and #4 cylinders in this engine.

As shown in Eq.(2.42), the pressure fluctuation is determined by the coupled mode shape of water coolant passage ψ'_n and modal response u_n . The modal response u_n is also determined by coupled mode shape of crankcase ϕ'_n as shown in Eq.(2.40). The difference of pressure fluctuation at different cylinders can be explained by the difference of coupled mode shapes of water coolant passage and crankcase. Figure 4.33 shows comparison of the coupled mode shapes of crankcase at thrust side of four cylinders. The coupled mode shape of crankcase of #1 cylinder is the largest followed by #4 cylinder, which coincides with 1236.3Hz coupled mode shape cross section of crankcase shown in Fig.4.17. Figure 4.34 shows the coupled pressure mode shapes of water coolant passage at thrust side of four cylinders. The largest coupled mode shapes of water coolant passage are seen at #1 and #4 cylinders, which agree with the 1236.3Hz coupled mode shape in the cross section of water coolant passage in Fig.4.17. The larger amplitude of coupled pressure mode shapes of water coolant passage and crankcase of #1 and #4 cylinders leads to the larger pressure fluctuation of these two cylinders as shown in Fig.4.31.

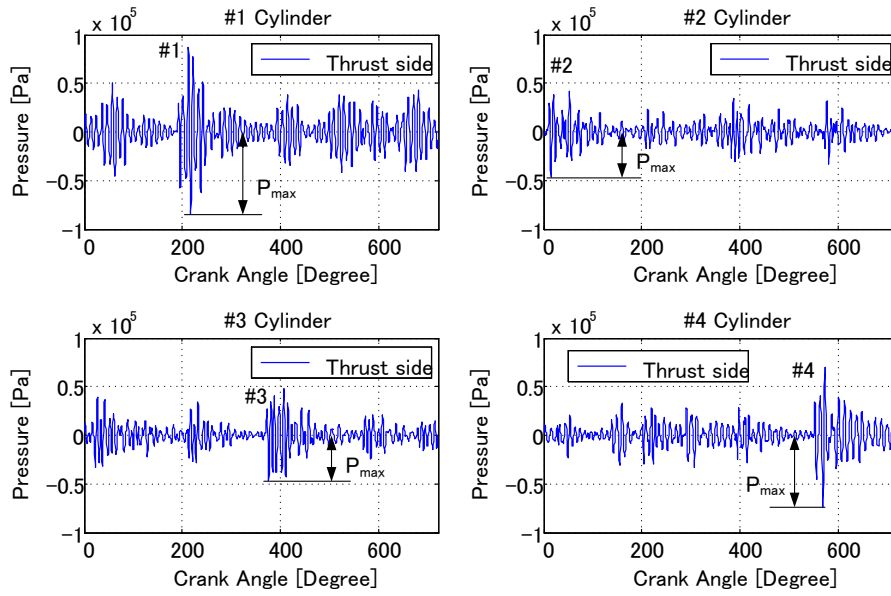


Fig.4.31 Pressure fluctuation at thrust side of four cylinders

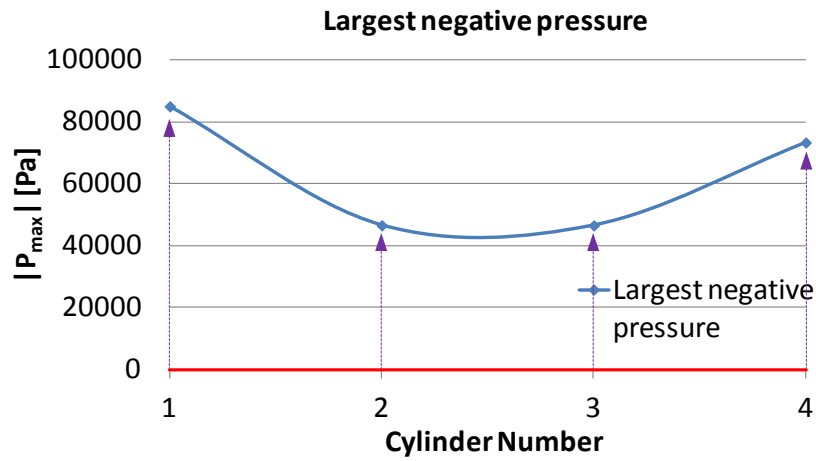


Fig.4.32 Largest negative pressure fluctuation at thrust side of four cylinders

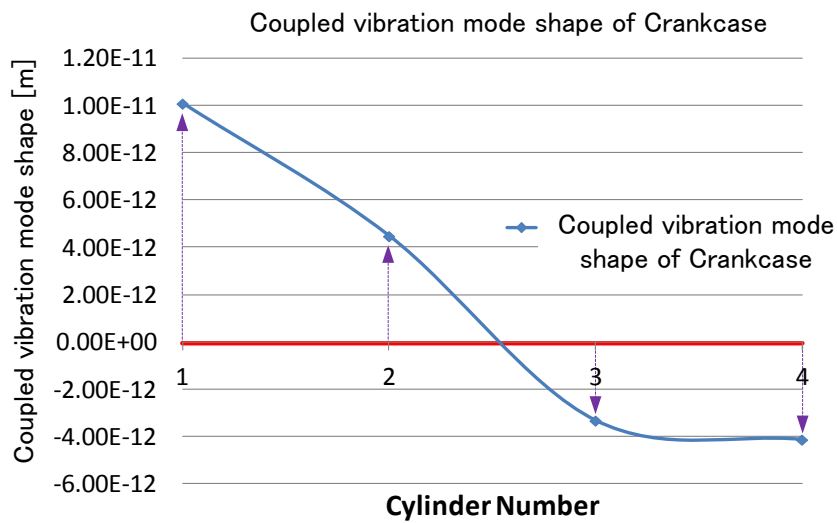


Fig.4.33 Coupled structural mode shapes of crankcase of four cylinders

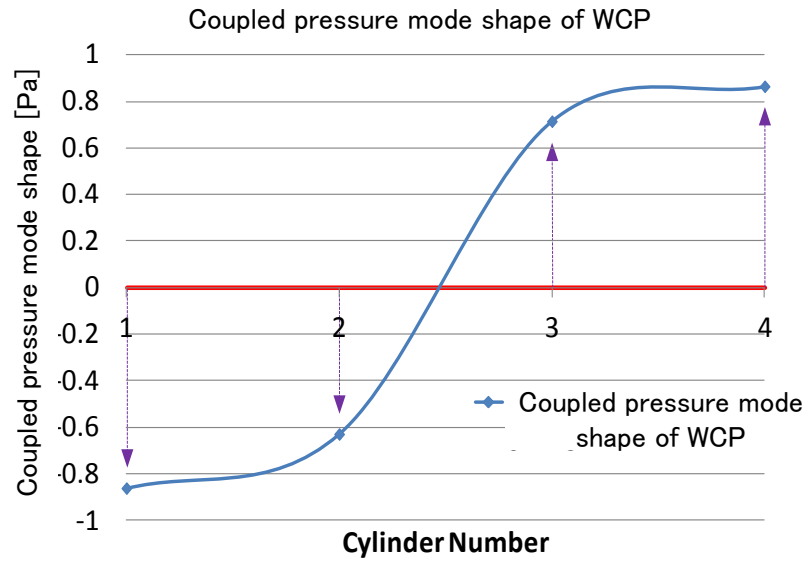
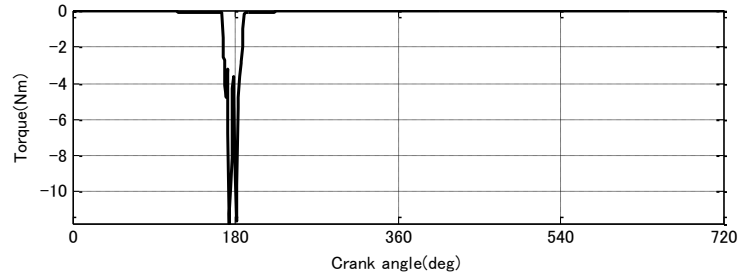
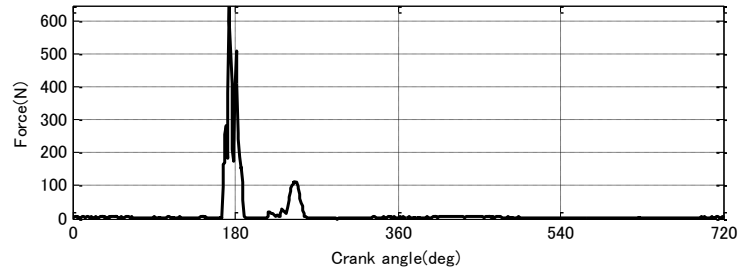


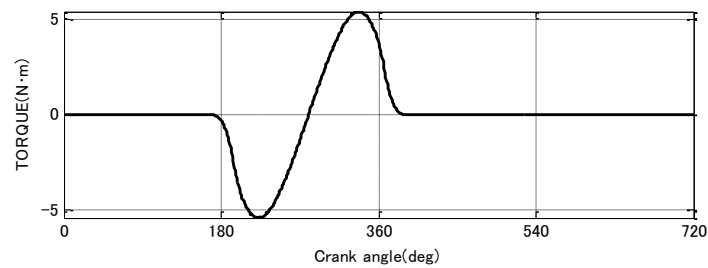
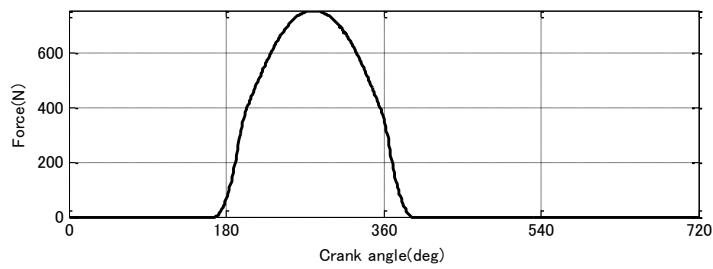
Fig.4.34 Coupled pressure mode shapes of water coolant passage of four cylinders

4.4 Pressure fluctuation in running condition

The pressure fluctuation of the coupled system between water coolant passage and assembled engine model under the running condition is calculated according to Eq.(2.49). The coupled system of assembled engine and water coolant passage is shown in Fig.2.4. The input forces include combustion pressure and piston slap force shown in Fig.4.21, injection forces and torques, valve train forces and torques shown in Fig.4.35. Main bearing impact force and gear impact forces are automatically considered in the equation of motion of the engine total structure described in Eq.(2.49).



(a) Injection



(b) Valve train

Fig.4.35 Injection forces and valve train forces

(1) Contribution of piston slap on water pressure fluctuation

The contribution of piston slap forces on pressure fluctuation is examined. The pressure fluctuation induced by excitation forces except piston slap force is calculated as Pre_{-1} . The pressure fluctuation induced by all excitation is calculated as Pre_{-2} . The pressure fluctuation

induced by only piston slap Pre_3 can be calculated as

$$Pre_3 = Pre_2 - Pre_1 \quad (4.1)$$

Fig.4.36 shows comparison of pressure fluctuation and acceleration at thrust side of #1 cylinder liner induced by only piston slap forces and induced by all excitation forces.

The difference between the pressure fluctuations induced by only piston slap forces and all excitation forces is not apparent especially at the ignition timing. Through the comparison, the amplitude of pressure fluctuation can be deemed as mainly induced by piston slap forces

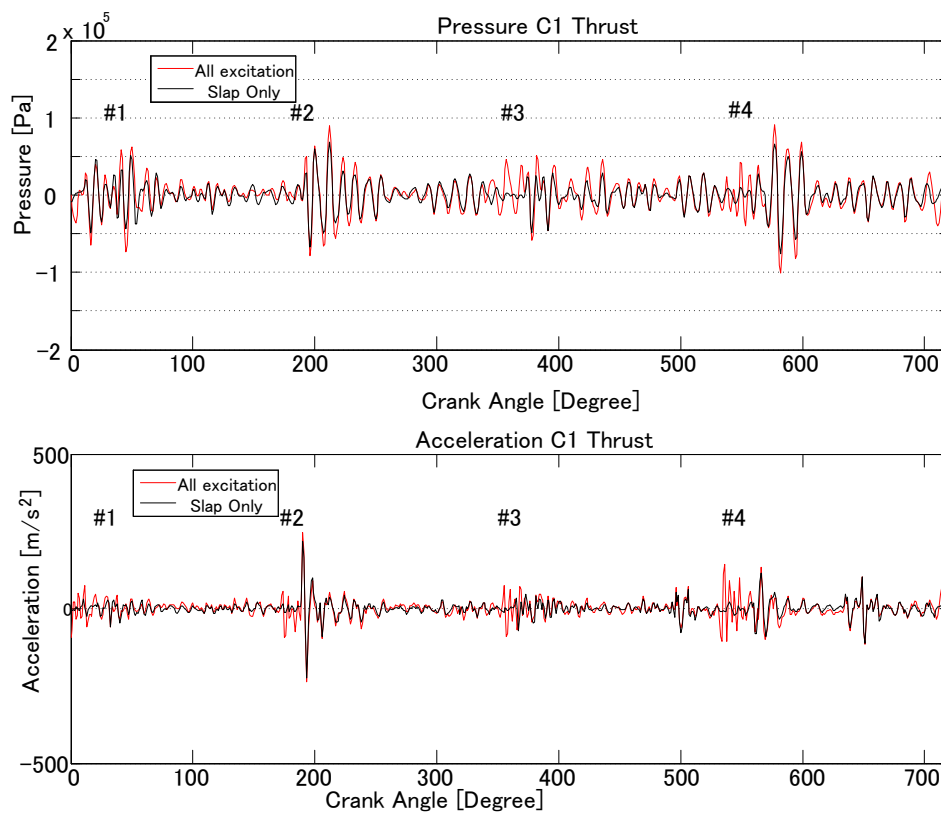


Fig.4.36 Comparison of pressure fluctuation and acceleration at #1 cylinder between all excitation and only piston slap force

(2) Effect of variation of water sound speed

Pressure fluctuations and liner accelerations are calculated at different water sound speed. Figure 4.37 shows the comparison of pressure fluctuation and acceleration at thrust side of #1 cylinder between sound speed $c=700\text{m/s}$ and $c=1000\text{m/s}$. Figure 4.38 shows the comparison between sound speed $c=1000\text{m/s}$ and $c=1500\text{m/s}$. The cylinder liner accelerations at different sound speed are almost at the same level, which indicates variation of sound speed has little effect on liner acceleration. The pressure fluctuation varies dramatically with sound speed. Figure 4.37 and Figure 4.38 shows that pressure fluctuation at sound speed 1000m/s is the largest, which trend is almost the same as the crankcase and water coolant passage model. At sound speed $c=1000\text{m/s}$, the pressure fluctuation at ignition timing of #1 and #4 cylinder become larger, which is influenced by the 2nd acoustic mode of water acoustic field and 10-th mode of crankcase.

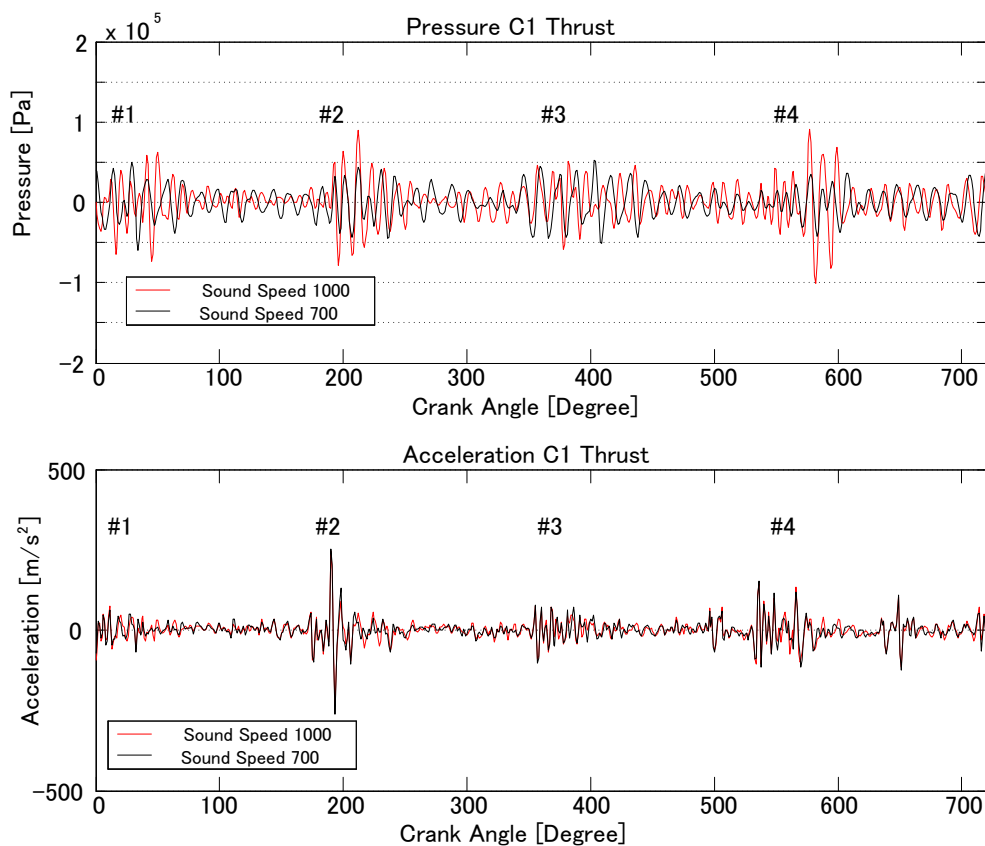


Fig.4.37 Calculated pressure fluctuation and acceleration at #1 cylinder of assembled engine (Comparison of water sound speed $c=1000\text{m/s}$ and $c=700\text{m/s}$)

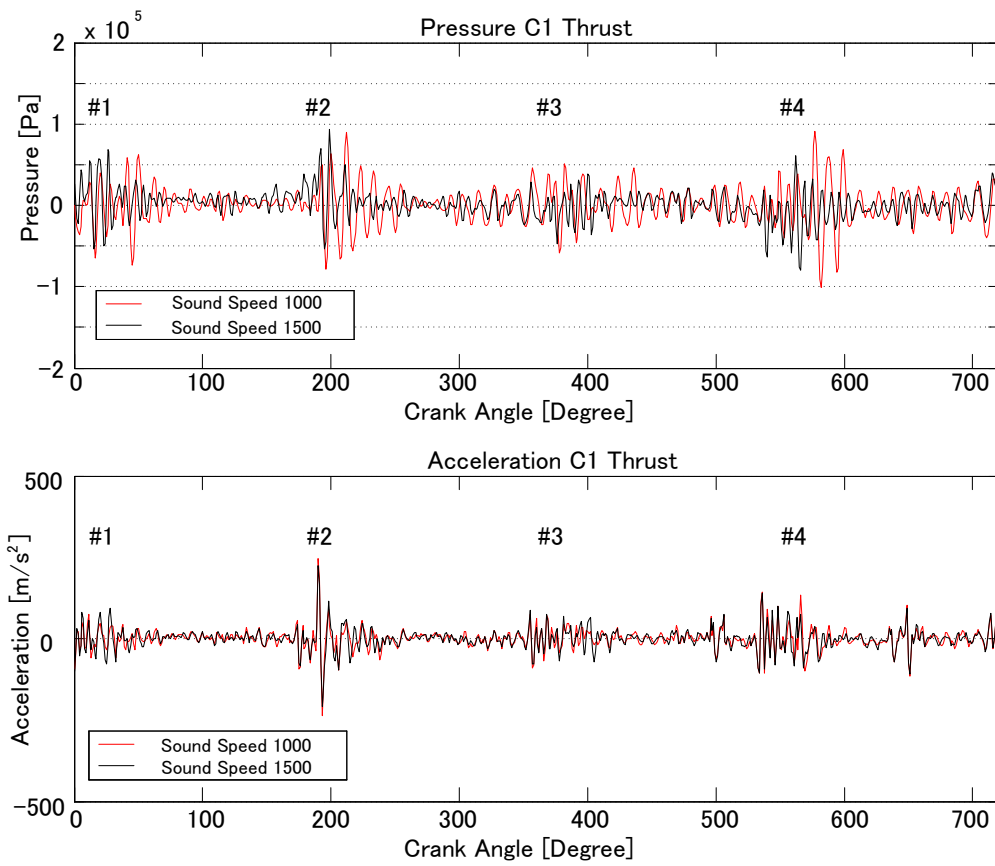


Fig.4.38 Calculated pressure fluctuation and acceleration at #1 cylinder of assembled engine (Comparison of water sound speed $c=1000m/s$ and $c=1500m/s$)

4.5 Chapter summary

Dynamic characteristics of crankcase structure and water acoustic field were calculated by FEM and these coupled dynamic properties were determined by the present method and its validity was verified by impact vibration experiments in air. Piston slap forces were simulated and applied to the cylinder liners of this coupled system. Pressure fluctuation on the cylinder wet surface was predicted under the action of piston slap force. The influence of sound speed of water on water pressure fluctuation was investigated. At sound speed $c=1000\text{m/s}$, the absolute value of negative pressure fluctuation reaches to its maximum value. The distribution of pressure fluctuation in water coolant passage was calculated and the difference of the maximum water pressure at each cylinder was examined based on the coupled mode shape of acoustic field and crankcase. In this case, the pressure fluctuation of #1 cylinder was the largest followed by #4 cylinder, which came from the coupled mode of crankcase torsional mode and the second acoustic mode in which pressure phase was reversed at front and rear side.

Water pressure fluctuation of assembled engine model has been estimated considering all excitation forces and rotating shaft system. Pressure fluctuation and liner vibration induced by all exciting forces and only piston slap were examined and it revealed that the pressure fluctuation and liner acceleration were mainly induced by piston slap forces under running condition. The influence of sound speed was also discussed and pressure fluctuation of assembled engine caused by all excitation forces also results in the largest at sound speed $c=1000\text{m/s}$. This tendency was almost same as crankcase and water coolant passage model.

Chapter 5

CONCLUSION

Liner cavitation seriously affects the reliability of water cooled internal combustion engine and it is a complex mechanical and electrochemical phenomenon. Engine vibration especially liner vibration is deemed as the primary cause, which is mainly induced by piston slap forces. Engine vibration brings the pressure fluctuation which may cause evaporation and condensation of cavities in the coolant. The repeating of implosion of cavities will finally result in cavitation erosion on the wet surface of cylinder liner. This research has developed an numerical method to predict the water pressure fluctuation in the water coolant passage considering the coupling effect between engine structure and water coolant passage under the action of external forces like combustion pressure, piston slap, main bearing impact and gear impact at the engine operating condition.

By use of FEM and modal analysis technique, equation of motion of coupled system of structure and water acoustic field inside was derived and furthermore incorporated into the coupled equation of engine total system to predict the water acoustic pressure fluctuation in running condition. The rectangular tank model was employed to examine the availability of the numerical procedure above mentioned. Bottom plate vibration was induced by impact force and vibration and water pressure fluctuation were measured simultaneously. Calculated natural frequencies and mode shapes of the coupled system and waveform of water pressure were in good agreement with the measurements. When impact force acting on the bottom plate was increased and water pressure dropped to the vapor pressure or less, high frequency pressure fluctuation which implies the occurrence of cavitation was observed

Dynamic characteristics of crankcase structure and acoustic field in water coolant passage were calculated by FEM and these coupled dynamic properties were determined by the present

method and its validity was verified by impact vibration experiments in air. Piston slap forces were simulated and applied to the cylinder liners of this coupled system. Pressure fluctuation on the cylinder wet surface was predicted under the action of piston slap force and pressure fluctuation amplitude changed with the sound speed in water coolant passage. It was revealed that the coupling term of structure mode and water acoustic pressure mode and the proximity of these natural frequencies had the large influence of the water pressure response. Calculated results showed that the magnitude of pressure fluctuation at different cylinder wet surface was influenced by the coupled mode shape of structure and acoustic field

Water pressure fluctuation of assembled engine with main components were incorporated has been estimated considering all excitation forces. Pressure fluctuation and liner vibration induced by all exciting forces or only piston slap were examined and it was concluded that the pressure fluctuation and liner acceleration were mainly induced by piston slap forces under running condition. The influence of sound speed was also discussed and pressure fluctuation of assembled engine caused by all excitation forces changed with water sound speed. This tendency was almost the same as crankcase and water coolant passage model.

In this study, numerical procedure to predict the pressure fluctuation in the water coolant passage in engine running condition was developed and its validity was confirmed by the experiment of rectangular box model. It was clarified that pressure fluctuation which is the main cause of liner cavitation was influenced by the coupled vibration characteristics of engine structure and acoustic characteristics of water coolant passage.

ACKNOWLEDGEMENTS

Special thanks and deep respect from the author to his parents for their supports, encouragements and advices, etc.

The author would like to express his deep thanks to his supervisor Professor Kazuhide OHTA for all of his guidance, encouragements and supports through the four years.

Warmest thanks are also given to Professor Shinya KIJIMOTO and Adjacent Professor Tatsumi KITAHARA for their advice and guidance on this doctoral thesis.

The author would like to express his warm thanks to the graduated student Hayashida for his pioneer work on liner cavitation research in this laboratory; Thanks are given to graduated students Tajima, Katae, Murae, Nakahara and Akano for their help and care in life and study. I feel grateful for the graduated students Nagatoshi, Azumatani and Ono for their cooperation in study and experiments. Thanks are also given to master second grade students Saeki and Enokizono for the laboratory activities organized by them. The master first grade student Yoshida is a very polite student who is an excellent partner.

The author would like to thank the former laboratory sectary Mrs. Kaneko who is very lovely and generous in helping others. Special thanks are given to the present laboratory sectary Mrs. Tomezuka who is very nice especially to foreign students.

Thanks are given to all the other members of Machinery Analysis Laboratory for all the good times spent together. I will remember the beautiful scenery of Kyushu University Ito Campus.

Reference

- [1]. Franc, J. P. and Michel, J. M. (Eds.), Fundamentals of cavitation. Springer Science & Business Media, 2006.
- [2]. Wagner, W. and Pruss, A., Journal of Physical Chemistry Reference Data, 1993, 22: 783-787.
- [3]. Newton, I., Opticks, or, a treatise of the reflections, refractions, inflections & colours of light, Courier Corporation, 1952,
- [4]. Eisenberg, P., Cavitation Damage (No. TR-233-1), HYDRONAUTICS INC LAUREL MD, 1963.
- [5]. Parsons, C. A. and Cook, S. S., Investigations into the causes of corrosion or erosion of propellers. Journal of American Society for Naval Engineers, 1919, 21(2): 536-541
- [6]. Philip, J. R., Hydrostatics and hydrodynamics in swelling soils. Water Resources Research, 1969, 5(5): 1070-1077.
- [7]. Rayleigh, L. VIII. On the pressure developed in a liquid during the collapse of a spherical cavity. The London, Edinburgh, and Dublin Philosophical Magazine and Journal of Science, 1917, 34(200): 94-98.
- [8]. Hickling, R. and Plesset, M. S. Collapse and rebound of a spherical bubble in water. Physics of Fluids (1958-1988), 1964, 7(1): 7-14.
- [9]. Yeh, H. C., & Yang, W. J. Dynamics of bubbles moving in liquids with pressure gradient. Journal of Applied Physics, 1968, 39(7): 3156-3165.
- [10]. Kornfeld, M., and L. Suvorov. "On the destructive action of cavitation." Journal of Applied Physics, 1944, 15(6): 495-506.
- [11]. Benjamin, T. Brooke, and Ao T. Ellis. "The collapse of cavitation bubbles and the pressures thereby produced against solid boundaries." Philosophical transactions of the Royal Society of London. Series A, Mathematical and physical sciences, 1966, 260(1110): 221-240.
- [12]. Plesset M S, Chapman R B. Collapse of an initially spherical vapour cavity in the neighborhood of a solid boundary[J]. Journal of Fluid Mechanics, 1971, 47(02): 283-290.
- [13]. Lauterborn W, Bolle H. Experimental investigations of cavitation-bubble collapse in the neighborhood of a solid boundary[J]. Journal of Fluid Mechanics, 1975, 72(02): 391-399.
- [14]. Fortes Patella, Regiane, et al. "Cavitation Erosion Mechanism: Numerical Simulations of the Interaction Between Pressure Waves and Solid Boundaries." <http://resolver.caltech.edu/cav2001:sessionA3.006> (2001).
- [15]. Haosheng, Chen, et al. Damages on steel surface at the incubation stage of the vibration cavitation erosion in water[J]. Wear, 2008, 265(5): 692-698.
- [16]. Kling C. L., A high speed photographic study of cavitation bubble collapse[R]. MICHIGAN UNIV ANN ARBOR CAVITATION AND MILTI PHASE FLOW LAB, 1970.
- [17]. Philipp A, Lauterborn W. Cavitation erosion by single laser-produced bubbles[J]. Journal of Fluid Mechanics, 1998, 361: 75-116.

- [18]. Bai L X, Xu W L, Zhang F X, et al. Cavitation characteristics of pit structure in ultrasonic field[J]. Science in China Series E: Technological Sciences, 2009, 52(7): 1974-1980.
- [19]. Berchiche N, Franc J P, Michel J M. A cavitation erosion model for ductile materials[J]. Journal of fluids engineering, 2002, 124(3): 601-606.
- [20]. Hammitt F G. Cavitation and multiphase flow phenomena[M]. McGraw-Hill, 1980.
- [21]. Hammitt F G. Cavitation erosion: the state of the art and predicting capability[R]. MICHIGAN UNIV ANN ARBOR DEPT OF MECHANICAL ENGINEERING, 1979.
- [22]. Hercamp R D. An overview of cavitation corrosion of diesel cylinder liners [J]. ASTM SPECIAL TECHNICAL PUBLICATION, 1993, 1192: 107-107.
- [23]. Speller F N, LaQue F L. Water Side Deterioration Of Diesel Engine Cylinder Liners [J]. Corrosion, 1950, 6(7): 209-215.
- [24]. Yu-Kang Z, Jiu-Gen H, Hammitt F G. Cavitation erosion of cast iron diesel engine liners[J]. Wear, 1982, 76(3): 329-335.
- [25]. Hercamp, R. D., and R. D. Hudgens. Cavitation Corrosion Bench Test for Engine Coolants. No. 881269. SAE Technical Paper, 1988.
- [26]. Pogodaev L I, Tret'yakov D V, Valishin A G, et al. Simulation of durability of cylinder liners of an internal combustion engine under vibration cavitation[J]. Journal of Machinery Manufacture and Reliability, 2008, 37(2): 143-151.
- [27]. Chance R L, Walker M S, Rowe L C. Evaluation of Engine Coolants by Electrochemical Methods[C]//Engine Coolant Testing: Second Symposium: Second International Symposium on Engine Coolants and Their Testing, Philadelphia, Pennsylvania, 9-10 April 1984. ASTM International, 1986, 887: 99.
- [28]. Ross T K, Aspin A F. The water-side corrosion of diesel engines[J]. Corrosion Science, 1973, 13(1): 53-61.
- [29]. Moore, W., The basics of diesel-engine coolant, Construction Equipment, 2005, pp.46-49
- [30]. Hercamp, R. D., and R. D. Hudgens. Silicate gelation in heavy-duty diesel engine cooling systems. No. 852327. SAE Technical Paper, 1985.
- [31]. Hercamp,R.D. "Recycling Used Coolant from Heavy Duty Engines," Presented at the Forum on Coolant Disposal and Recycling, National Automotive Radiator Service Association National Meeting, Atlanta, 30 March, 1989
- [32]. Mitchell, W.A., 'Statistical Treatment of Laboratory Data for ASTM D 1387-70 Using Soft Solder,' Engine Coolant Testing: State of the Art, ASTM STP 705, W.H. Ailor, Ed., American Society for Testing and Materials, Philadelphia, 1980, pp.220-232.
- [33]. Pinelli, J., Cummins Internal Report, 1990
- [34]. Schulmeister R. Vibratory tests in water on the combined action of cavitation and corrosion[J]. Characterization and Determination of Erosion Resistance, ASTM STP, 1970, 474: 109-126.
- [35]. Ron H. Cavitation erosion of cylinder liners and how to eliminate it. Pipeline & Gas journal, 1999, 266(3): 36-39

- [36]. Hobbs J. M., 'Experience with a 20KC Cavitation Erosion test', Erosion by cavitation on Impingement, ASTM STP 408, American Society for Testing and Materials, Philadelphia, 1967, pp.159-179
- [37]. Garcia R., Hammitt F. G. Cavitation Damage and Correlations With Material and Fluid Properties J.Fluids Eng. 89(4), 753-763 (1967)
- [38]. Thiruvengadam A. High-frequency fatigue of metals and their cavitation-damage resistance[J]. Journal of Manufacturing Science and Engineering, 1966, 88(3): 332-340.
- [39]. Kerr, S. L., Determination of the relative resistance to cavitation erosion by the vibratory method. Trans ASME, 59, 1937,373-397.
- [40]. Mousson, J. M., Pitting resistance of metals under cavitation conditions. Trans. ASME, 59, 1937, 399-408
- [41]. Beeching, R., Selecting alloys to resist cavitation erosion. Prod. Eng.,19, 1948, 110.
- [42]. Rheingans, W. J., Accelerated-cavitation research. Trans ASME, 72, 1950, 705.
- [43]. Higgins, R.I. The resistance of cast iron to cavitation erosion. BCIRA J.Res. Devel., 7, 1957, 476.
- [44]. Higgins, R. I. The nature of pitting attack on cast iron propellers and preliminary experiments on its prevention by cathodic protection. Brit CIRA Res. Rep., 1957, 476
- [45]. Margulis, W., McGowan, J.A. and Leith, W.C. Cavitation control through diesel engine water treatment. Trans SAE, 65, 1957, 331.
- [46]. Leith, W.C. and Thompson, A.L. Some corrosion effects in accelerated cavitation damage. Trans. ASME J. Basic Eng., 82, 1960, 795.
- [47]. Bogachev, I.N.,Senkevich, V.F. and Petukhova, T.M. Resistance of cast irons to cavitation erosion. Met. Sci. Heat Treat., 8, 1966, 795.
- [48]. Preece C M. Cavitation erosion[J]. Treatise on Materials Science and Technology, Vol. 16, Erosion, 1979: 249-308.
- [49]. Lopez Vazquez, L.B. Study of vibratory cavitation in castings: diesel engine cylinder liners, I, II. Fundicion, 29, 1982, 2-14, 58-75.
- [50]. Pokhmurskii V I, Tolstova S V, Milyakov A P, et al. Cavitation-corrosion resistance of steel and cast iron with diffusion coatings[J]. Materials Science, 1976, 10(6): 621-623.
- [51]. Voroshnin L G, Khappalaev A Y, Abacharaev M M. Cavitation resistance of chromium diffusion coatings on steels and cast irons[J]. Metal Science and Heat Treatment, 1981, 23(5): 370-372.
- [52]. Collins, H.H., "Introduction to Cavitation Corrosion", Symposium on Cavitation Corrosion and Its Prevention in Diesel Engines, British Railways Board, London, Nov, 1965, pp.5-9
- [53]. Retolaza, J. Further Developments in the Manufacture and Applications of Steel Chrome-Plated Cylinder Liners with Special Reference to Cavitation and Erosion Problems on the Water Side. No. 740315. SAE Technical Paper, 1974.
- [54]. Endo H, Ikenouchi M. Cavitation Erosion on the Surface of Cylinder Liners in Diesel

- Engine. JOURNAL OF THE MARINE ENGINEERING SOCIETY IN JAPAN. 1970;5(7):489-97.
- [55]. Ikenouchi M, Endo Y. Cavitation Erosion on the Surface of Cylinder Liners in Diesel Engine (2nd Report). JOURNAL OF THE MARINE ENGINEERING SOCIETY IN JAPAN. 1972, 7(6):485-95.
- [56]. Yonezawa T, Kanda H. Study of Cavitation Erosion on Cylinder Liner and Cylinder Block. The Japan Institute of Marine Engineering. 1984, 19(5):384-390.
- [57]. Yonezawa T. A study on Cavitation erosion of cylinder liner and cylinder block (Calculation method of cylinder liner vibration), Journal of the M.E.S.J., 1985, 20(4):258-264.
- [58]. Yonezawa T, Kanida H, Katsuragi K. Study on Cavitation Erosion of Cylinder Liner: 1st Report, Estimation of Cylinder Liner Vibration, Transactions of Japan Society of Mechanical Engineers, Series C, 1984, 50(459):2104-2112.
- [59]. Yonezawa T, Senda J, Okubo M, Fujimoto H, Miki H. Experimental Analysis on the Behavior of Cavitation Bubbles at Cylinder Liner Erosion in Diesel Engines. JOURNAL OF THE MARINE ENGINEERING SOCIETY IN JAPAN. 1985, 20(6):361-9.
- [60]. Yonezawa T, Senda J, Yoshiki K, Saitou M, Fujimoto H, Miki H. BEHAVIOR OF BUBBLES IN A VIBRATION FIELD. Nippon Kikai Gakkai Ronbunshu, B Hen/Transactions of the Japan Society of Mechanical Engineers, Part B. 1987, 53(491):1894-900.
- [61]. Yonezawa T, Senda J, Saito M, Fujimoto H, Miki H. Analysis of Cavitation on Cylinder Liner and Cylinder Block. JOURNAL OF THE MARINE ENGINEERING SOCIETY IN JAPAN. 1987, 22(5):308-16.
- [62]. Yonezawa T, Senda J, Saitou M, Yoshiki K, Fujimoto H, Miki H. Analysis of Cavitation on Cylinder Liner and Cylinder Block. JOURNAL OF THE MARINE ENGINEERING SOCIETY IN JAPAN. 1988, 23(1):38-46.
- [63]. Gladwell, G. M. L., Zimmermann G. "On energy and complementary energy formulations of acoustic and structural vibration problems [J]" Journal of Sound and Vibration. 1966, 3(3): 495-506.
- [64]. Craggs A. The transient response of a coupled plate-acoustic system using plate and acoustic finite elements[J]. Journal of Sound and Vibration, 1971, 15(4): 509-528.
- [65] Shuku T, Ishihara K. The analysis of the acoustic field in irregularly shaped rooms by the finite element method[J]. Journal of Sound and Vibration, 1973, 29(1): 67-IN1.
- [66]. Gladwell G M L. A variational formulation of damped acousto structural vibration problems[J]. Journal of Sound and vibration, 1966, 4(2): 172-186.
- [67] Sandberg G, Göransson P. A symmetric finite element formulation for acoustic

- fluid-structure interaction analysis[J]. *Journal of sound and vibration*, 1988, 123(3): 507-515.
- [68]. Zienkiewicz O C, Bettess P. Fluid- structure dynamic interaction and wave forces. An introduction to numerical treatment[J]. *International Journal for Numerical Methods in Engineering*, 1978, 13(1): 1-16.
- [69]. Wolf J A, Nefske D J, Howell L J. Structural-acoustic finite element analysis of the automobile passenger compartment[R]. SAE Technical Paper, 1976.
- [70]. Shiraki, K., Noise control design and simulation, Ouyou-gijyutu-shuppan, 1987(in Japanese) .
- [71] He, J., and Zhi, Z., 2001. *Modal Analysis*. Butterworth Heinemann, Oxford
- [72] Petyt, M., 1990. *Introduction to Finite Element Vibration Analysis*. Cambridge University Press, Cambridge.
- [73] Genta, G., 2009. *Vibration Dynamics and Control*. Spring, New York.
- [74] Hagiwara, I., and Ma, Z., 1991. Improved modesuperposition technique for modal frequency response analysis of coupled acoustic-structural systems." *AIAA Journal*, 29(10),pp.93-106.
- [75] Ohta K, Ikeda K, Zheng G, Okimoto T, Honda I. Vibration Response and Noise Radiation of Engine Block Coupled with the Rotating Crankshaft and Gear Train. *Transactions of the Japan Society of Mechanical Engineers, Series C*, 2009, 75(752):789-795.
- [76]. Zheng, G. Z., PhD Thesis, Kyushu University, 2011
- [77]. Xiang Ling, Shan-Tung Tu, Jian-Ming Gong, Application of Runge-Kutta=merson algorithm for creep damage analysis, *International Journal of Pressure Vessels and Piping*, Vol.77 (2000) 243–248.
- [78]. J.C. Butcher, Numerical methods for ordinary differential equations in the 20th century, *Journal of computation and applied mathematics*, Vol.125 (2000) 1–29.
- [79]. Ohta K, Murae S, Nagatoshi S, Azumatani K and Wang X, Study on the piston slap induced liner cavitation (Prediction of the pressure fluctuation), *JSME Dynamic and Design Conference 2012*, 2012.
- [80]. Ohta K, Nagatoshi S, Azumatani K, Wang X and Ono A, Study on the piston slap induced liner cavitation (Prediction of the pressure fluctuation), *JSME Dynamic and Design Conference 2013*, 2013.
- [81]. Shamsborhan, H., Coutier-Delgosha, O., Caignaert, G., and Nour, F. A., 2010, Experimental Determination of the Speed of Sound in Cavitating Flows, *Exp.Fluids*, 49(6), pp. 1359–1373.
- [82]. Wagner, W., and Pruss, A., 1993, “Reference Data,” *J. Phys. Chem.*, 22(2), pp.334–337.
- [83]. K. Ohta, Y. Irie, K. Yamamoto, H. Ishikawa, Piston slap induced noise and vibration of internal combustion engines (1st report), *SAE*. 20 (1985) 258–264.

- [84]. K. Ohta, K. Amano, A. Hayashida, G. Zheng, I. Honda, Analysis of piston slap induced noise and vibration of internal combustion engine (effect of piston profile and pin offset), *Journal of Environment and Engineering*. 6 (2011) 712–722.
- [85]. K. Ohta, K. Azumatani, A. ONO, A. Saeki, X. Wang, Study on the liner cavitation induced by piston slap (Box model experiment and structural-acoustic analysis), *JSME Dynamic and Design Conference 2014*, 2014.

Appendix A

Left eigenvectors and eigenvalue

$$-\omega_i^2 \begin{bmatrix} \tilde{\mathbf{M}}_S & 0 \\ -\Psi^t \mathbf{S} \Phi & \tilde{\mathbf{M}}_A \end{bmatrix} \begin{pmatrix} \mathbf{a}_i \\ \mathbf{b}_i \end{pmatrix} + \begin{bmatrix} \tilde{\mathbf{M}}_S & \Phi^t \mathbf{S} \Psi \\ 0 & \tilde{\mathbf{K}}_A \end{bmatrix} \begin{pmatrix} \mathbf{a}_i \\ \mathbf{b}_i \end{pmatrix} = 0 \quad (\text{A.1})$$

From Eq.(1), the equation below holds

$$-\omega_i^2 \tilde{\mathbf{M}}_S \mathbf{a}_i + (\Phi^t \mathbf{S} \Psi) \mathbf{b}_i + \tilde{\mathbf{K}}_S \mathbf{a}_i = 0 \quad (\text{A.2})$$

Transporting Eq.(2) and considering the symmetric of mass and stiffness matrix

$$\begin{aligned} -\omega_i^2 \mathbf{a}_i^t \tilde{\mathbf{M}}_S + \mathbf{b}_i^t (\Psi^t \mathbf{S} \Phi) + \mathbf{a}_i^t \tilde{\mathbf{K}}_S &= 0 \\ -\mathbf{a}_i^t \omega_i^2 \tilde{\mathbf{M}}_S + \frac{1}{\omega_i^2} \mathbf{b}_i^t (\omega_i^2 \Psi^t \mathbf{S} \Phi) + \mathbf{a}_i^t \tilde{\mathbf{K}}_S &= 0 \end{aligned} \quad (\text{A.3})$$

From Eq.(1), the equation below holds

$$\omega_i^2 \Psi^t \mathbf{S} \Phi \mathbf{a}_i - \omega_i^2 \tilde{\mathbf{M}}_A \mathbf{b}_i + \tilde{\mathbf{K}}_A \mathbf{b}_i = 0 \quad (\text{A.4})$$

Transporting Eq.(4) and considering the symmetric of mass and stiffness matrix

$$\begin{aligned} \omega_i^2 \mathbf{a}_i^t \Phi^t \mathbf{S} \Psi - \omega_i^2 \mathbf{b}_i^t \tilde{\mathbf{M}}_A + \mathbf{b}_i^t \tilde{\mathbf{K}}_A &= 0 \\ \frac{1}{\omega_i^2} \mathbf{b}_i^t (-\omega_i^2 \tilde{\mathbf{M}}_A) + \mathbf{a}_i^t \Phi^t \mathbf{S} \Psi + \frac{1}{\omega_i^2} \mathbf{b}_i^t \tilde{\mathbf{K}}_A &= 0 \end{aligned} \quad (\text{A.5})$$

Eq.(3) and Eq.(5) can be composed as

$$\left(\mathbf{a}_i^t, \frac{1}{\omega_i^2} \mathbf{b}_i^t \right) \left(-\omega_i^2 \begin{bmatrix} \tilde{\mathbf{M}}_S & 0 \\ -\Psi^t \mathbf{S} \Phi & \tilde{\mathbf{M}}_A \end{bmatrix} + \begin{bmatrix} \tilde{\mathbf{K}}_S & \Phi^t \mathbf{S} \Psi \\ 0 & \tilde{\mathbf{K}}_A \end{bmatrix} \right) = 0 \quad (\text{A.6})$$

Left eigenvector can be expressed as

$$(\mathbf{c}^t, \mathbf{d}^t) \left(-\omega^2 \begin{bmatrix} \tilde{\mathbf{M}}_s & 0 \\ -\Psi^t \mathbf{S} \Phi & \tilde{\mathbf{M}}_A \end{bmatrix} + \begin{bmatrix} \tilde{\mathbf{K}}_s & \Phi^t \mathbf{S} \Psi \\ 0 & \tilde{\mathbf{K}}_A \end{bmatrix} \right) = 0 \quad (\text{A.7})$$

Left eigenvector $\left(\mathbf{a}_i^t, \frac{1}{\omega_i^2} \mathbf{b}_i^t \right)$ which share the same eigenvalue ω_i can be got.

Appendix B

1. Analysis of acoustic field by Nastran

1.1 Acoustic Wave Equation

A small element in fluid is under consideration as shown in Fig.B.1. The displacement and density are assumed to be $\mathbf{d}(\xi, \eta, \zeta)$ and ρ_a with pressure p acting on the element. According to Newton's law,

$$\rho_a \frac{\partial^2 \mathbf{d}}{\partial t^2} = - \left(\frac{\partial}{\partial x} + \frac{\partial}{\partial y} + \frac{\partial}{\partial z} \right) p = -\nabla p \quad (\text{B.1})$$

Pressure p can be expressed in terms of fluid compressibility ($\kappa = \frac{1}{\rho c^2}$) as

$$p = -\frac{1}{\kappa} \left(\frac{\partial \xi}{\partial x} + \frac{\partial \eta}{\partial y} + \frac{\partial \zeta}{\partial z} \right) = -\frac{1}{\kappa} \nabla \mathbf{d} \quad (\text{B.2})$$

According to Eq.(1) and Eq.(2), the acoustic wave equation can be expressed as

$$\frac{\partial^2 p}{\partial t^2} = \frac{1}{\kappa \rho_a} \left(\frac{\partial^2 p}{\partial x^2} + \frac{\partial^2 p}{\partial y^2} + \frac{\partial^2 p}{\partial z^2} \right) = \frac{1}{\kappa \rho_a} \nabla^2 p \quad (\text{B.3})$$

One-dimensional acoustic vibration can be given as below,

$$\kappa \frac{\partial^2 p}{\partial t^2} = \frac{1}{\rho_a} \frac{\partial^2 p}{\partial x^2} \quad (\text{B.4})$$

Assuming small element contacts with solid wall with impedance Z_n , the boundary condition can be expressed as below,

$$p = j \frac{1}{\rho_a \omega} Z_n \nabla p \quad (\text{B.5})$$

Where, ω is the circular angle (rad/sec)

- Boundary of open end $Z_n = 0$; $p = 0$
- Boundary of rigid wall $Z_n = \infty$; $\nabla p = -j\rho_a\omega\xi = 0$
- Boundary of impedance $0 < Z_n < \infty$; $p = j\frac{1}{\rho_a\omega}Z_n\nabla p = Z_n\xi$

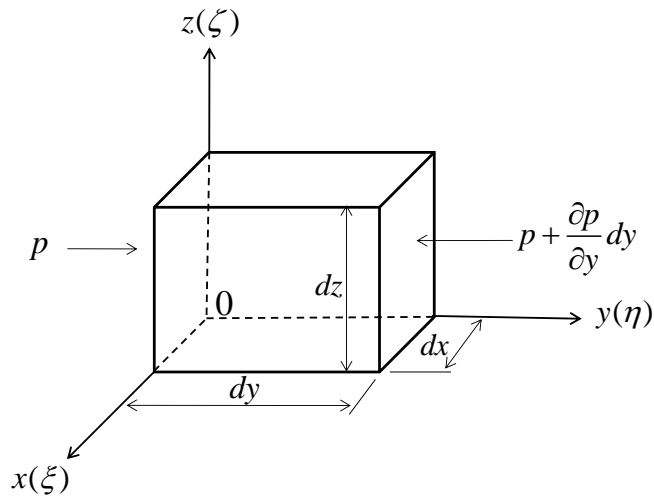


Fig.B.1 Equilibrium of small element of acoustic field in one dimension

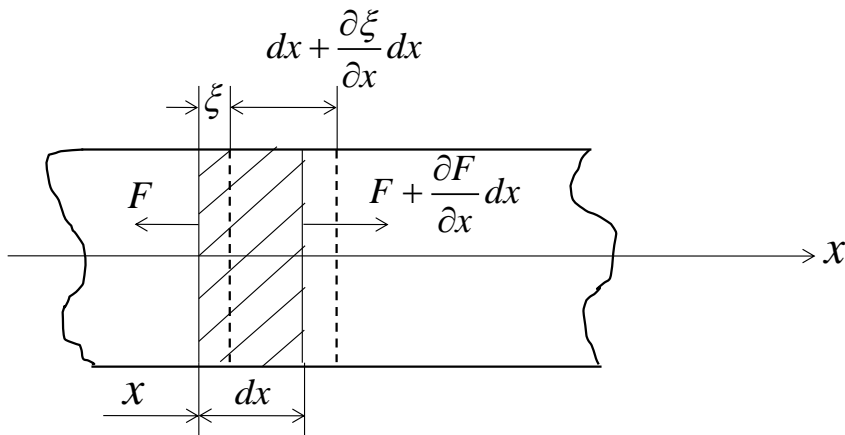


Fig.B.2 Equilibrium of small element of a bar

1.2 Solid wave equation

Considering longitudinal vibration of a solid bar and applying Newton's second law onto the small element with length of dx as shown in Fig.2, the equation of motion of this small element in x direction is given as,

$$\rho_s A dx \frac{\partial^2 \xi}{\partial t^2} = \frac{\partial F}{\partial x} dx = \frac{\partial}{\partial x} \left(EA \frac{\partial \xi}{\partial x} \right) dx \quad (\text{B.6})$$

Where, Displacement ξ , Section area A , Young's modulus E , Density ρ_s . Eq.(B.6) can be rewritten as,

$$\rho_s \frac{\partial^2 \xi}{\partial t^2} = E \frac{\partial^2 \xi}{\partial x^2} \quad (\text{B.7})$$

If the small element is connected with element nearby through stiffness k and damping coefficient C , the equation of boundary condition as shown below holds,

$$k\xi + j\omega C\xi = EA \frac{\partial \xi}{\partial x} \quad (\text{B.8})$$

- Complete unconstrained $k = 0, C = 0$; $\frac{\partial \xi}{\partial x} = \nabla \xi \neq 0$
- Complete constrained $k = \infty, C = \infty$; $\xi = 0$
- Stiffness and damping $0 < k < \infty, 0 < C < \infty$; $\xi = \frac{EA}{k + j\omega C} \frac{\partial \xi}{\partial x}$

1.3 Comparison of motion of equation between acoustic field and structure

$$\text{Acoustic : } \kappa \frac{\partial^2 p}{\partial t^2} = \frac{1}{\rho_a} \frac{\partial^2 p}{\partial x^2}$$

$$\text{Structure : } \rho_s \frac{\partial^2 \xi}{\partial t^2} = E \frac{\partial^2 \xi}{\partial x^2}$$

(Acoustic)		(Structure)
• Pressure	:	p \Leftrightarrow Displacement : ξ
• Inverse of bulk data	:	κ \Leftrightarrow Density : ρ_s
• Inverse of density	:	$1/\rho_a$ \Leftrightarrow Young's modulus : E

Comparison of boundary condition

• Open end	\Leftrightarrow	Complete constrained
• Rigid wall	\Leftrightarrow	Complete unconstrained

1.4 Three dimensional

On condition of three dimensions, the compress stiffness, shear stiffness and torsion stiffness should be considered. The compress stiffness is considered only in acoustic field. The stiffness matrix of structure is composed of elastic modulus E , shear modulus G and Poisson ratio ν .

In acoustic field, the stiffness matrix is composed by the inverse of density $1/\rho_a$

(corresponding to the Young's modulus E) only. The material characteristics of Nastran input file should be solid anisotropic, the input matrix is shown below.

$$\begin{pmatrix} \sigma_x \\ \sigma_y \\ \sigma_z \\ \tau_{xy} \\ \tau_{yz} \\ \tau_{zx} \end{pmatrix} = \begin{bmatrix} G11 & G12 & G13 & G14 & G15 & G16 \\ & G22 & G23 & G24 & G25 & G26 \\ & & G33 & G34 & G35 & G36 \\ & & & G44 & G45 & G46 \\ \text{symmetric} & & & & G55 & G56 \\ & & & & & G66 \end{bmatrix} \begin{pmatrix} \varepsilon_x \\ \varepsilon_y \\ \varepsilon_z \\ \gamma_{xy} \\ \gamma_{yz} \\ \gamma_{zx} \end{pmatrix}$$

If the inverse of density were entered into the elements (G11,G22,G33,G44,G55,G66) of the stiffness matrix, the vibration characteristics of acoustic field can be calculated.

Consider the vibration in one direction (for example X direction). The degree of freedom in

other directions (Y,Z) should be constrained. The sound pressure can be recognized as the vibration in X direction.

Parameters of acoustic field of water medium

FEM software input value (structure/SI unit)			
	Air	Water	Unit
(1)Density*	6.6542E-06	2.04082E-9	kg/m3
(2)Young's modulus**	0.76923077	0.001	Pa
Transverse elastic	0		Pa
Poisson ratio	0		-

Used value (Acoustic/SI unit)			
	Air	Water	
Density	1.3	1000	kg/m3
Sound speed	340	700	m/s
Impedance	442	700000	kg/m2s

(1): $Density^* = 1/(Density \times sound\ speed^2)$

(2): $Young's\ modulus^{**} = 1/Density$

2. Modal mass and modal stiffness

2.1. Mode shapes of acoustic field of rectangular tank (One-end-open)

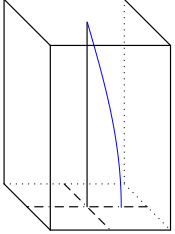
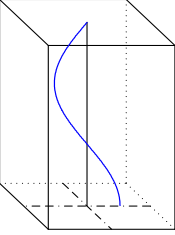
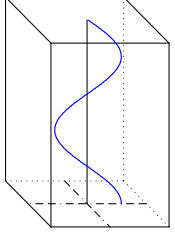
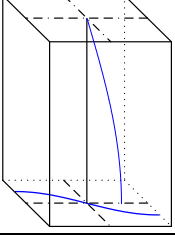
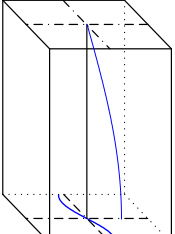
Mode		
1	$p_{A1} = p_0 \cos\left(\frac{\pi x}{2H}\right)$	
	$f_{A1} = \frac{c}{4H} = 700\text{Hz or } 850\text{Hz}$	
2	$p_{A2} = p_0 \cos\left(\frac{3\pi x}{2H}\right)$	
	$f_{A2} = \frac{3c}{4H} = 2100\text{Hz or } 2550\text{Hz}$	
3	$p_{A3} = p_0 \cos\left(\frac{5\pi x}{2H}\right)$	
	$f_{A3} = \frac{5c}{4H} = 3500\text{Hz or } 4250\text{Hz}$	
4	$p_{A4} = p_0 \cos\left(\frac{\pi x}{2H}\right) \cos\left(\frac{\pi y}{L_y}\right)$	
	$f_{A4} = \sqrt{f_{A1}^2 + f_y^2} = 3375\text{Hz or } 4334\text{Hz}$	
5	$p_{A5} = p_0 \cos\left(\frac{\pi x}{2H}\right) \cos\left(\frac{\pi z}{L_z}\right)$	
	$f_{A4} = \sqrt{f_{A1}^2 + f_z^2} = 3375\text{Hz or } 4334\text{Hz}$	

Fig.B.3 Mode shapes of acoustic field of rectangular tank at Hw=250mm

Table.B.1 Comparison between theoretical and Nastran results

No.	Mode			Nastran (Hz)	Theory (Hz)	Nastran (kg)	Theory (kg)
	x	y	z	MAT9		MAT9	
1	1	0	0	699.97	700	2.87E-12	2.87E-12
2	2	0	0	2099.1	2100	2.87E-12	2.87E-12
3	3	0	0	3495.7	3500	2.87E-12	2.87E-12
4	1	1	0	3370.8	3375	1.29E-12	1.43E-12
5	1	0	1	3370.8	3375	1.29E-12	1.43E-12

2.2. The modal mass of each mode

$$\psi_{A1} = \cos \frac{\pi x}{2H} \quad \psi_{A2} = \cos \frac{3\pi x}{2H} \quad \psi_{A3} = \cos \frac{5\pi x}{2H}$$

$$\psi_{A4} = \cos \frac{\pi x}{2H} \cos \frac{\pi y}{L_y} \quad \psi_{A5} = \cos \frac{\pi x}{2H} \cos \frac{\pi z}{L_z}$$

$$\tilde{m}_{A1} = \frac{1}{\rho c^2} \int_0^H (\iint \psi_{A1}^2 ds) dx = \frac{L_y L_z}{\rho c^2} \int_0^H \left(\frac{1}{2} + \frac{1}{2} \cos \frac{\pi x}{H} \right) dx = \frac{L_y L_z H}{2\rho c^2}$$

$$\tilde{m}_{A2} = \frac{1}{\rho c^2} \int_0^H (\iint \psi_{A2}^2 ds) dx = \frac{L_y L_z}{\rho c^2} \int_0^H \left(\frac{1}{2} + \frac{1}{2} \cos \frac{3\pi x}{H} \right) dx = \frac{L_y L_z H}{2\rho c^2}$$

$$\tilde{m}_{A3} = \frac{1}{\rho c^2} \int_0^H (\iint \psi_{A3}^2 ds) dx = \frac{L_y L_z}{\rho c^2} \int_0^H \left(\frac{1}{2} + \frac{1}{2} \cos \frac{5\pi x}{H} \right) dx = \frac{L_y L_z H}{2\rho c^2}$$

$$\begin{aligned} \tilde{m}_{A4} &= \frac{1}{\rho c^2} \int_0^H \int_0^{L_z} \int_0^{L_y} \psi_{A4}^2 dy dz dx \\ &= \frac{1}{\rho c^2} \int_0^H \left(\frac{1}{2} + \frac{1}{2} \cos \frac{\pi x}{H} \right) dx \int_0^{L_y} \left(\frac{1}{2} + \frac{1}{2} \cos \frac{2\pi y}{L_y} \right) dy \int_0^{L_z} dz = \frac{L_y L_z H}{4\rho c^2} \end{aligned}$$

$$\begin{aligned} \tilde{m}_{A5} &= \frac{1}{\rho c^2} \int_0^H \int_0^{L_z} \int_0^{L_y} \psi_{A5}^2 dy dz dx \\ &= \frac{1}{\rho c^2} \int_0^H \left(\frac{1}{2} + \frac{1}{2} \cos \frac{\pi x}{H} \right) dx \int_0^{L_z} \left(\frac{1}{2} + \frac{1}{2} \cos \frac{2\pi z}{L_z} \right) dz \int_0^{L_y} dy = \frac{L_y L_z H}{4\rho c^2} \end{aligned}$$

3. The modal stiffness of each mode

3.1 Circular frequencies

$$\left. \begin{array}{l} \omega_{A1} = 2\pi f \\ \lambda/4 = H \\ f\lambda = c \end{array} \right\} \omega_{A1} = \frac{\pi c}{2H}; \quad \left. \begin{array}{l} \omega_{A2} = 2\pi f \\ 3\lambda/4 = H \\ f\lambda = c \end{array} \right\} \omega_{A2} = \frac{3\pi c}{2H}; \quad \left. \begin{array}{l} \omega_{A3} = 2\pi f \\ 5\lambda/4 = H \\ f\lambda = c \end{array} \right\} \omega_{A3} = \frac{5\pi c}{2H};$$

$$\left. \begin{array}{l} \omega_y = 2\pi f \\ \lambda/2 = L_y \\ f\lambda = c \end{array} \right\} \omega_y = \frac{\pi c}{L_y}; \quad \left. \begin{array}{l} \omega_z = 2\pi f \\ \lambda/2 = L_z \\ f\lambda = c \end{array} \right\} \omega_z = \frac{\pi c}{L_z};$$

$$\omega_{A4}^2 = \omega_{A1}^2 + \omega_y^2 = \left(\frac{\pi^2 c^2}{4H^2} + \frac{\pi^2 c^2}{L_y^2} \right) \quad \omega_{A5}^2 = \omega_{A1}^2 + \omega_z^2 = \left(\frac{\pi^2 c^2}{4H^2} + \frac{\pi^2 c^2}{L_z^2} \right)$$

3.2 Modal stiffness

$$\tilde{k}_{A1} = \tilde{m}_{A1} \omega_{A1}^2 = \frac{L_z L_y H}{2\rho c^2} \times \left(\frac{\pi c}{2H} \right)^2 \quad \tilde{k}_{A2} = \tilde{m}_{A2} \omega_{A2}^2 = \frac{L_z L_y H}{2\rho c^2} \times \left(\frac{3\pi c}{2H} \right)^2$$

$$\tilde{k}_{A3} = \tilde{m}_{A3} \omega_{A3}^2 = \frac{L_z L_y H}{2\rho c^2} \times \left(\frac{5\pi c}{2H} \right)^2$$

$$\tilde{k}_{A5} = \tilde{k}_{A4} = \tilde{m}_{A4} \omega_{A4}^2 = \frac{L_y L_z H}{4\rho c^2} \times \left(\frac{\pi^2 c^2}{4H^2} + \frac{\pi^2 c^2}{L_y^2} \right)$$

4. Relationship between void fraction and sound speed

The sound speed in two-phase flows can be calculated based on the equation below

$$c_0 = \left[\frac{(1-\phi)^2}{c_l^2} + \frac{\phi^2}{c_g^2} + \phi(1-\phi) \frac{\rho_l}{p_l} \right]^{-1/2} \quad (\text{B.9})$$

where, ϕ is the void fraction, c_l and c_g are the sound speed in water and air respectively,

ρ_l is the density of water, p_l is the pressure of liquid at the surface of bubbles. If the void

fraction is above 0.1%, the sound speed can be approximately calculated as

$$c_0 = \sqrt{\frac{p_l}{\phi(1-\phi)\rho_l}} \quad (\text{B.10})$$

Figure B.4 shows the relationship between void fraction and sound speed in water. Figure B.5 shows the relationship between void fraction and sound speed when void fraction is in the range of $0.0 \sim 3.5 \times 10^{-4}$. ($c_l = 1500 \text{ m/s}$ $p_l = 100 \text{ kPa}$ $c_g = 340 \text{ m/s}$ $\rho_l = 1000 \text{ kg/m}^3$)

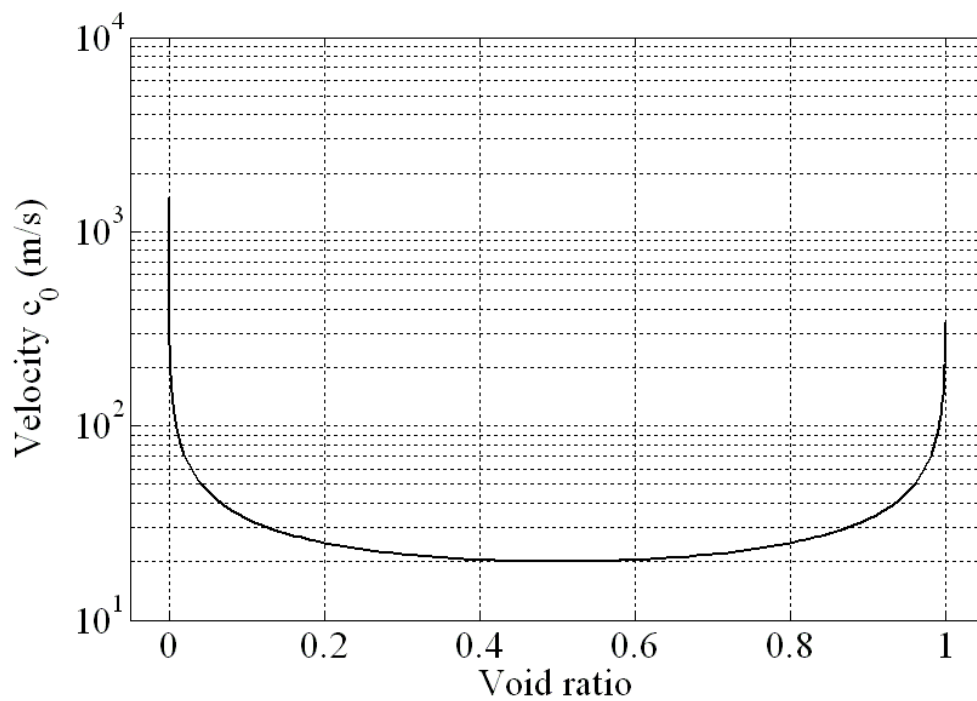


Fig.B.4 Velocity of sound depending on void ratio in water

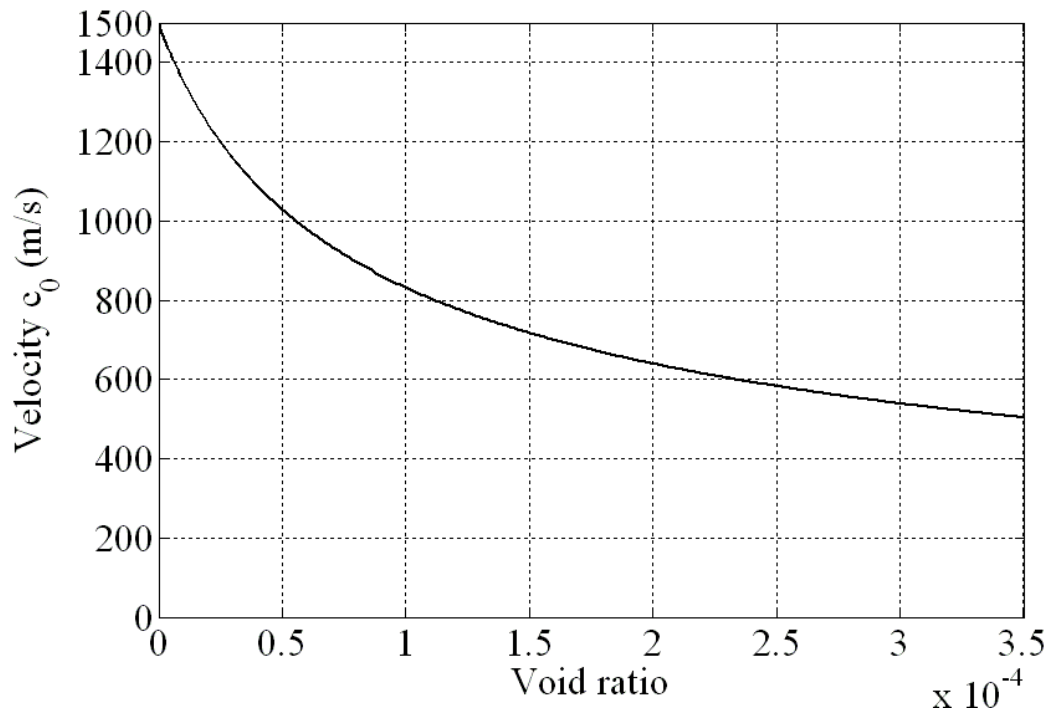


Fig.B.5 Velocity of sound depending on void ratio in water
(void ratio $0.0 \sim 3.5 \times 10^{-4}$)

Appendix C

Equation of motion of acoustic field with acceleration loading acting on the boundary

The equation of motion of acoustic vibrations formulated by Hamilton's principle using force-like functions (pressure) has been presented by Gladwell and Zimmermann[63]. The equation of motion of acoustic field is going to be described in terms of pressure and acceleration. From the perspective of energy, acoustic field can be composed of kinetic energy T , potential energy U_1 , dissipative energy U_2 and work done U_3 by volume ric acoustic sources from vibration of structure boundary. The energy balance of the system can be described as below.

$$T + U_1 + U_2 = U_3 \quad (\text{C.1})$$

The kinetic and potential energy densities for small amplitude osillations in fluids related to the particle velocity and sound pressure respectively are given in Eq.(C.2) [64~69].

$$T = \frac{1}{2} \rho_0 |\dot{\mathbf{u}}|^2 \quad U_1 = \frac{1}{2} \kappa p^2 \quad (\text{C.2})$$

where, ρ_0 is the mean density of the fluid, $\dot{\mathbf{u}}$ is particle velocity, κ is the fluid compressibility ($\kappa = 1/\rho_0 c^2$) and p is sound pressure. Most acoustic energy dissipation occurs at boundary surfaces, the work done over the r-th dissipative face by sound pressure p and displacement u_r in direction normal to the surface can be expressed in terms of acoustic impedance $Z = p/\dot{u}_r$ as

$$U_2 = pu = p \int \dot{u}_r dt = p \int \frac{P}{Z} dt \quad (C.3)$$

The work done by vibration of structure on the boundary, which equals the work done by acoustic sources acting at the boundary surface, is given by

$$U_3 = pu_r = p \int (\int \ddot{u}_r dt) dt \quad (C.4)$$

In case of harmonic vibration, such that $p = p_0 \exp(j\omega t)$ and $u = u_0 \exp(j\omega t)$, the conservation of momentum of acoustic wave equation can be expressed as

$$\begin{aligned} \partial p / \partial x &= -\rho_0 \ddot{u}_x = -\rho_0 j\omega \dot{u}_x \\ \partial p / \partial y &= -\rho_0 \ddot{u}_y = -\rho_0 j\omega \dot{u}_y \\ \partial p / \partial z &= -\rho_0 \ddot{u}_z = -\rho_0 j\omega \dot{u}_z \end{aligned} \quad (C.5)$$

$$|\dot{u}|^2 = (\dot{u}_x)^2 + (\dot{u}_y)^2 + (\dot{u}_z)^2 = -\frac{1}{(\rho_0 \omega)^2} \left[\left(\frac{\partial p}{\partial x} \right)^2 + \left(\frac{\partial p}{\partial y} \right)^2 + \left(\frac{\partial p}{\partial z} \right)^2 \right] = -\frac{(\nabla p)^2}{(\rho_0 \omega)^2} \quad (C.6)$$

$$\nabla p = (\partial p / \partial x, \partial p / \partial y, \partial p / \partial z)$$

Substituting Eq.(C.6) into Eq.(C.2), the kinetic energy can be expressed as

$$T = -\frac{1}{2\rho_0 \omega^2} (\nabla p)^2 \quad (C.7)$$

Dissipative energy U_2 can be transformed from Eq.(C.3) in harmonic vibration as below

$$U_2 = pu_r = p \int \dot{u}_r dt = p \int \frac{P}{Z} dt = \frac{P^2}{j\omega Z} \quad (\text{C.8})$$

Work done on the boundary by harmonic structural vibration U_3 can be expressed as

$$U_3 = pu_r = p \int (\int \ddot{u}_r dt) dt = \frac{p\ddot{u}_r}{-\omega^2} \quad (\text{C.9})$$

The Lagrangian yields

$$\begin{aligned} L &= \iiint_V (T + U_1) dV + \iint_{S_2} U_2 dS - \iint_{S_3} U_3 dS \\ &= \iiint_V \left(-\frac{(\nabla p)^2}{2\rho_0\omega^2} + \frac{1}{2\rho_0c^2} p^2 \right) dV + \iint_{S_2} \frac{P^2}{j\omega Z} dS - \iint_{S_3} \frac{p\ddot{u}_r}{-\omega^2} dS \end{aligned} \quad (\text{C.10})$$

Supposing the pressure in an element "e" can be expressed by the node pressure \mathbf{p}_e through shape function \mathbf{g} as

$$p = \mathbf{g}^t \mathbf{p}_e = \mathbf{p}_e^t \mathbf{g} \quad (\text{C.11})$$

The gradient and gradient square can be written as

$$\nabla p = \begin{pmatrix} \partial \mathbf{g}^t / \partial x \\ \partial \mathbf{g}^t / \partial y \\ \partial \mathbf{g}^t / \partial z \end{pmatrix} \mathbf{p}_e = \begin{pmatrix} \mathbf{g}_x^t \\ \mathbf{g}_y^t \\ \mathbf{g}_z^t \end{pmatrix} \mathbf{p}_e, \quad (\nabla p)^2 = (\nabla p)^t (\nabla p) \quad (\text{C.12})$$

The Lagrangian for element "e" can be written as

$$L_e = \frac{1}{2\omega^2} \left\{ \begin{aligned} & \iiint_{V_e} \left[-\frac{\mathbf{p}_e^t (\mathbf{g}_x \mathbf{g}_x^t + \mathbf{g}_y \mathbf{g}_y^t + \mathbf{g}_z \mathbf{g}_z^t) \mathbf{p}_e}{\rho_0} + \frac{\omega^2}{\rho_0 c^2} \mathbf{p}_e^t \mathbf{g} \mathbf{g}^t \mathbf{p}_e \right] dV \\ & - \iint_{S_{e2}} j\omega \frac{2\mathbf{p}_e^t \mathbf{g} \mathbf{g}^t \mathbf{p}_e}{Z} dS + \iint_{S_{e3}} 2\mathbf{p}_e^t \mathbf{g} \ddot{u}_{en} dS \end{aligned} \right\} \quad (C.13)$$

where, \ddot{u}_{en} is the boundary acceleration normal to the surface of element "e", which can be calculated by inner product of $\ddot{\mathbf{u}}_e$ and normal vector \mathbf{n}_e of element "e". The normal vector obeys the right hander screw rule which always points to the side of acoustic field as shown in Fig.C.1.

The Lagrangian of the entire acoustic field can be expressed as summation of each element.

$$L = \sum_e L_e \quad (C.14)$$

Substituting the Lagrangian L into Euler-Lagrange equation as shown in Eq.(C.15) and taking node pressure \mathbf{p}_e^t as the generalized coordinate, the Euler-Lagrange equation of acoustic field can be given as Eq.(C.16)

$$\frac{d}{dt} \frac{\partial L}{\partial \dot{q}} - \frac{\partial L}{\partial q} = 0 \quad (C.15)$$

$$\begin{aligned} \frac{\partial L}{\partial \mathbf{p}_e^t} &= \sum_e \frac{\partial L_e}{\partial \mathbf{p}_e^t} = \sum_e \frac{1}{2\omega^2} \left\{ \begin{aligned} & \iiint_{V_e} \left[-\frac{(\mathbf{g}_x \mathbf{g}_x^t + \mathbf{g}_y \mathbf{g}_y^t + \mathbf{g}_z \mathbf{g}_z^t) \mathbf{p}_e}{\rho_0} + \frac{\omega^2}{\rho_0 c^2} \mathbf{g} \mathbf{g}^t \mathbf{p}_e \right] dV \\ & - \iint_{S_{e2}} j\omega \frac{2\mathbf{g} \mathbf{g}^t \mathbf{p}_e}{Z} dS + \iint_{S_{e3}} 2\mathbf{g} \ddot{u}_{en} dS \end{aligned} \right\} \\ &= \sum_e \frac{1}{2\omega^2} (-\mathbf{K}_e \mathbf{p}_e + \omega^2 \mathbf{M}_e \mathbf{p}_e - j\omega \mathbf{D}_e \mathbf{p}_e + \mathbf{f}_e) = 0 \end{aligned} \quad (C.16)$$

The equation of motion of acoustic field derived by finite element method can

be given as Eq.(C.17)

$$-\omega^2 \mathbf{M}_A \mathbf{p} + j\omega \mathbf{D}_A \mathbf{p} + \mathbf{K}_A \mathbf{p} = \mathbf{f} \quad (\text{C.17})$$

where,

$$\mathbf{M}_A = [\mathbf{M}_{ij}^e], \quad \mathbf{M}_{ij}^e = \sum_e \iiint_{V_e} \frac{\mathbf{g}\mathbf{g}^t}{\rho_0 c^2} dV$$

$$\mathbf{D}_A = [\mathbf{D}_{ij}^e], \quad \mathbf{D}_{ij}^e = \sum_e \iint_{S_{e2}} \frac{2\mathbf{g}\mathbf{g}^t}{Z} dS$$

$$\mathbf{K}_A = [\mathbf{K}_{ij}^e], \quad \mathbf{M}_{ij}^e = \sum_e \iiint_{V_e} \frac{(\mathbf{g}_x \mathbf{g}_x^t + \mathbf{g}_y \mathbf{g}_y^t + \mathbf{g}_z \mathbf{g}_z^t) \mathbf{p}_e}{\rho_0} dV$$

$$\mathbf{f} = \iint_{S_{e3}} 2\mathbf{g}\ddot{u}dS = \mathbf{S}\ddot{\mathbf{x}}_B$$

$$\mathbf{S} = \begin{bmatrix} \ddots & & 0 \\ & S_e & \\ 0 & & \ddots \end{bmatrix}, \quad \ddot{\mathbf{x}}_B = \begin{pmatrix} \vdots \\ 2\mathbf{g}\ddot{u}_{en} \\ \vdots \end{pmatrix} = \begin{pmatrix} \ddot{x}_{en} \\ \vdots \end{pmatrix}$$

S_e is the area of boundary element "e". $\ddot{\mathbf{x}}_B$ is the acceleration loading on the boundary.

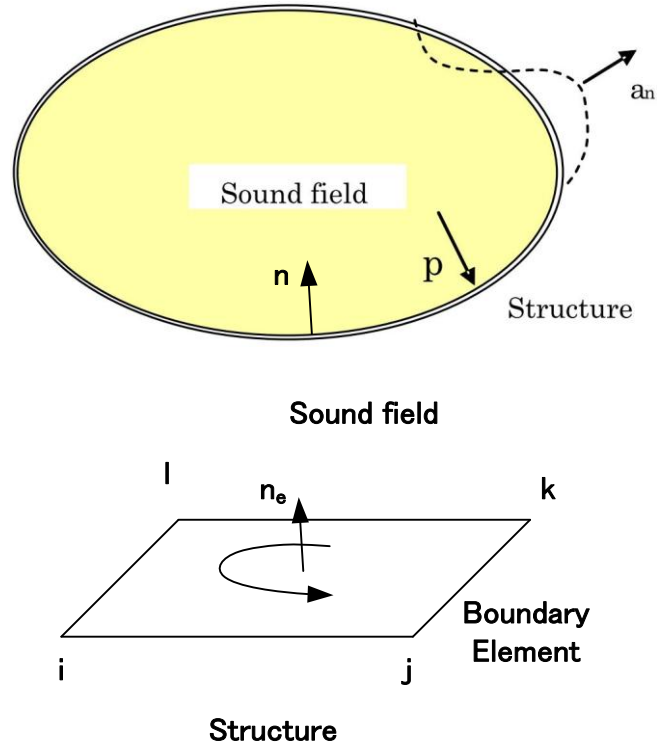


Fig.C.1 Analytical model of structural-acoustic coupled system

Appendix D

Mechanism of piston slap

1 . Inertia force and moment of piston due to piston motion

Figure D.1 shows velocities at piston pin and center of gravity of piston.

$$v_G = v_P + v \quad (v: \text{relative velocity between P and G})$$

$$\left. \begin{array}{l} v_{Gx} = v_{Px} + v_x \\ v_{Gy} = v_{Py} + v_y \end{array} \right\} \Rightarrow \left. \begin{array}{l} \dot{x}_G = \dot{x}_P + (y_G - y_P)\dot{\theta}_P \\ \dot{y}_G = \dot{y}_P - (x_G - x_P)\dot{\theta}_P \end{array} \right\} \Rightarrow \left. \begin{array}{l} \dot{x}_G = \dot{x}_P + L_y\dot{\theta}_P \\ \dot{y}_G = \dot{y}_P - L_x\dot{\theta}_P \end{array} \right\} \quad (D.1)$$

From the geometrical relationship shown in Fig.D.2, we can get the expression of y_P as follow,

$$y_P = \sqrt{l^2 - [r \sin(\alpha - \gamma_0) + x_{CO} - x_P - x_{PO}]^2} + r \cos(\alpha - \gamma_0) - l_0 \quad (D.2)$$

$$\text{Supposed } \alpha = \omega t; \quad A = r \sin(\alpha - \gamma_0) + x_{CO} - x_P - x_{PO}$$

$$y_P = \sqrt{l^2 - A^2} + r \cos(\omega t - \gamma_0) - l_0 \quad (D.3)$$

$$\dot{y}_P = -(l^2 - A^2)^{\frac{1}{2}} \cdot A \cdot A' - r\omega \sin(\omega t - \gamma_0) \quad (D.4)$$

$$\begin{aligned} \ddot{y}_P &= \frac{[A^2 A'^2 + (l^2 - A^2) A'' + A'' A (l^2 - A^2)]}{-(l^2 - A^2)^{\frac{3}{2}}} - r\omega^2 \cos(\omega t - \gamma_0) \\ &= \frac{[l^2 r^2 \omega^2 \cos^2(\omega t - \gamma_0) - r\omega^2 \sin(\omega t - \gamma_0) A (l^2 - A^2)]}{-(l^2 - A^2)^{\frac{3}{2}}} - r\omega^2 \cos(\omega t - \gamma_0) \\ &= -r\omega^2 \left[\frac{rl^2 \cos^2(\omega t - \gamma_0) - A(l^2 - A^2) \sin(\omega t - \gamma_0)}{(l^2 - A^2)^{\frac{3}{2}}} + \cos(\omega t - \gamma_0) \right] \quad (D.5) \end{aligned}$$

The kinetic energy of piston can be expressed as

$$T = \sum \frac{1}{2} m v^2 + \sum \frac{1}{2} I \theta^2 \quad (\text{D.6})$$

Kinetic energy of piston is composed of kinetic energy of gravity of piston and piston ring and the small end of con rod. we can have the following equation of kinetic energy

$$T = \frac{1}{2} m_p (x_G^2 + y_G^2) + \frac{1}{2} I_G \dot{\theta}_G^2 + \frac{1}{2} m_r (\dot{x}_p^2 + \dot{y}_p^2) + \frac{1}{2} m_{rg} y_p^2$$

Considering Eq.(D.1) and $\dot{\theta}_p = \dot{\theta}_G$ the kinetic energy of piston will be

$$T = \frac{1}{2} m_p \left[(\dot{x}_p + L_y \dot{\theta}_p)^2 + (\dot{y}_p - L_x \dot{\theta}_p)^2 \right] + \frac{1}{2} I_G \dot{\theta}_p^2 + \frac{1}{2} m_r (\dot{x}_p^2 + \dot{y}_p^2) + \frac{1}{2} m_{rg} \dot{y}_p^2 \quad (\text{D.7})$$

F_{IX}, F_{IY} are transverse and vertical inertia force respectively, T_I is the rotational moment of inertia around piston pin. Using Lagrange equation, we can obtain F_{IX}, F_{IY}, T_I

$$F_{IX} = \frac{d}{dt} \left(\frac{\partial T}{\partial \dot{x}_p} \right) - \frac{\partial T}{\partial x_p} = m_p (\ddot{x}_p + L_y \ddot{\theta}_p) + m_r \ddot{x}_p = (m_p + m_r) \ddot{x}_p + m_p L_y \ddot{\theta}_p \quad (\text{D.8})$$

$$\begin{aligned} F_{IY} &= \frac{d}{dt} \left(\frac{\partial T}{\partial \dot{y}_p} \right) - \frac{\partial T}{\partial y_p} = m_p \ddot{y}_p - m_p L_x \ddot{\theta}_p + m_r \ddot{y}_p + m_{rg} \ddot{y}_p \\ &= (m_p + m_r + m_{rg}) \ddot{y}_p - m_p L_x \ddot{\theta}_p \end{aligned} \quad (\text{D.9})$$

$$\begin{aligned} T_I &= \frac{d}{dt} \left(\frac{\partial T}{\partial \dot{\theta}_p} \right) - \frac{\partial T}{\partial \theta_p} = m_p L_y \ddot{x}_p - m_p L_x \ddot{y}_p + \left[I_G + (L_x^2 + L_y^2) m_p \right] \ddot{\theta}_p \\ &= m_p L_y \ddot{x}_p - m_p L_x \ddot{y}_p + I_p \ddot{\theta}_p \quad (I_p = I_G + (L_x^2 + L_y^2) m_p) \end{aligned} \quad (\text{D.10})$$

2. Forces applied on piston

2.1 Gas force is shown as

$$F_g = \frac{\pi}{4} D^2 p \quad (D.11)$$

D: diameter of cylinder;
p: pressure in the cylinder
Downward is positive

2.2 Reaction force of connecting rod

From the equilibrium of the force acting on the piston in vertical direction (Fig.D.3), we can get the following equation

$$F_l \cos \beta + F_{f1} + F_{f2} + \sum_{i=1}^3 F_{qi} - F_g = F_{IY} \quad (D.12)$$

Substituted Eq.(D.9) into Eq.(D.12)

$$F_l \cos \beta = (m_p + m_r + m_{rg}) \ddot{y}_p - m_p L_x \ddot{\theta}_p - F_{f1} - F_{f2} - \sum_{i=1}^3 F_{qi} + F_g \quad (D.13)$$

$$F_l = F_{I1} - \frac{m_p L_x}{\cos \beta} \ddot{\theta}_p \quad (D.14)$$

$$\text{where } F_{I1} = \frac{(m_p + m_r + m_{rg}) \ddot{y}_p - F_{f1} - F_{f2} - \sum_{i=1}^3 F_{qi} + F_g}{\cos \beta}$$

Side force $F_{ly} = F_l \sin \beta$

2.3 Moment due to friction

Figure D.4 shows the moment due to friction

$$T_p = \text{sgn}(\dot{\phi}) \mu_p R_p F_l \quad (D.15)$$

$\left\{ \begin{array}{l} R_p : \text{Radius of piston pin} \\ \mu_p : \text{friction coefficient} \end{array} \right.$

$$\dot{\phi} = \dot{\beta} - \dot{\theta}_p \quad \text{sgn}(\dot{\phi}) = \begin{cases} 1 & \dots \dot{\phi} > 0 \\ -1 & \dots \dot{\phi} < 0 \end{cases}$$

2.4 Vertical friction force between j-th piston ring and the liner

$$P_{ej} B_j \pi D_j = \int_0^{2\pi} F_{ej} d\phi \Rightarrow P_{ej} = \frac{2F_{ej}}{B_j D_j} \quad (\text{D.16})$$

- F_{ej} : the tension of the j-th piston ring (ring is compressed)
- B_j : the thickness of the j-th piston ring
- D_j : the outside diameter of the j-th ring
- P_{ej} : the pressure due to the tension of the j-th ring
- P_j : the pressure between j-1th and j-th ring

The average pressure of P_j and P_{j+1} acting on the j-th ring is $\frac{1}{2}(P_j - P_{j+1})$ as

shown in Fig D.5.

So the compress force is $\frac{B_j}{2}(P_j - P_{j+1})$

The total force per unit length (as shown in Fig.D.9 is

$$W_j = \frac{B_j}{2}(P_j - P_{j+1}) + P_{ej} B_j \quad (\text{D.17})$$

The vertical friction force between j-th piston ring and the liner is

$$F_{qj} = -\text{sgn}(\dot{y}_p) \mu_{qj} W_j \pi D_j \quad (\text{D.18})$$

where

$$\begin{cases} \mu_{qi} = 0.05 \sim 0.2 : \text{friction coefficient between ring and liner} \\ \text{sgn}(\dot{y}_p) = \begin{cases} 1 & \dot{y}_p > 0 \\ -1 & \dot{y}_p < 0 \end{cases} \end{cases}$$

2.5 Transverse friction force between the j-th piston ring and the ring groove

Figure D.6 shows the transverse friction forces

$$F_{rj} = -\text{sgn}(\dot{x}_j) \mu_{rj} F_{qj} \quad (\text{D.19})$$

where

$$\left\{ \begin{array}{l} \mu_{rj} = 0.15 \sim 0.2: \text{friction coefficient between ring and groove} \\ \text{sgn}(\dot{x}_j) = \begin{cases} 1 & \dots \dot{x}_j > 0 \\ -1 & \dots \dot{x}_j < 0 \end{cases} \quad \dot{x}_j: \text{piston velocity at the j-th ring} \end{array} \right.$$

2.6 Vertical friction force between the piston and the liner

Figure D.7 shows the vertical friction force

$$\begin{aligned} F_{f1} &= -\text{sgn}(\dot{y}_p) \mu_f \sum F_{Ai} \\ F_{f2} &= -\text{sgn}(\dot{y}_p) \mu_f \sum F_{Ei} \end{aligned} \quad (\text{D.20})$$

$$\left\{ \begin{array}{l} \mu_f \approx 0.1: \text{friction coefficient between skirt and liner} \\ \text{sgn}(\dot{y}_p) = \begin{cases} 1 & \dots \dot{y}_p > 0 \\ -1 & \dots \dot{y}_p < 0 \end{cases} \quad \dot{y}_p: \text{piston velocity at the j-th ring} \end{array} \right.$$

2.7 Recovering force of piston ring in transverse direction

Figure D.8 shows the recovering force of piston ring

$$F_{kr} = -k_r x_{kr} \quad (\text{D.21})$$

$$\left\{ \begin{array}{l} k_r: \text{spring constant of wave spring} \\ x_{kr}: \text{displacement at attaching point} \end{array} \right.$$

2.8 Impact force between piston and liner

x_{PAi} : displacement of piston at thrust side

x_{LAi} : displacement of liner at thrust side

The impact force at collision point i of the thrust side can be expressed as

$$F_{Ai} = -k_i(x_{PAi} - x_{LAi}) - c_i(\dot{x}_{PAi} - \dot{x}_{LAi}) \quad (D.22)$$

The impact force at anti-thrust side can be expressed as

$$F_{Ei} = -k_i(x_{PEi} - x_{LEi}) - c_i(\dot{x}_{PEi} - \dot{x}_{LEi}) \quad (D.23)$$

$i = 1 \sim N_p$: number of the collision point

k_i : spring constant to simulate dynamic stiffness of piston (Fig D.10)

c_i : damping coefficient to simulate damping effect of oil film (Fig D.10)

3. Equation of motion of coupled piston and liner system

3.1 Equation of motion of piston as a rigid body

According to the equilibrium of forces acting on the piston (Fig.D.2) in x direction, the following equation holds

$$F_{IX} + F_l \sin \beta + \sum F_{Ei} = \sum F_{Ai} + \sum F_{ri} + F_{kr} \quad (D.24)$$

Substitute Eq.(D.8) and Eq.(D.14) into Eq.(D.24), the following equation holds

$$(m_p + m_r)\ddot{x}_p + m_p(L_y - L_x \tan \beta)\ddot{\theta}_p = -F_{l1} \sin \beta + \sum F_{Ai} + \sum F_{ri} - \sum F_{Ei} + F_{kr} \quad (D.25)$$

Consider moment equilibrium around piston pin, the following equation holds

$$T_l + \sum F_{Ai} H_{Ai} + F_{f1} \left(\frac{\bar{D}}{2} + x_{po} \right) = T_p + \sum F_{Ei} H_{Ei} + F_{f2} \left(\frac{\bar{D}}{2} - x_{po} \right) + F_g x_{po} + F_{kr} H_{kr} + \sum F_{ri} H_{ri} \quad (D.26)$$

Substitute Eq.(D.10) into Eq.(D.27) the following equation holds

$$m_p L_y \ddot{x}_p + I_p \ddot{\theta}_p = m_p L_x \ddot{y}_p + T_p + \sum F_{Ei} H_{Ei} + F_{f2} \left(\frac{\bar{D}}{2} - x_{po} \right) + F_g x_{po} + F_{kr} H_{kr} + \sum F_{ri} H_{ri} - \sum F_{Ai} H_{Ai} - F_{f1} \left(\frac{\bar{D}}{2} + x_{po} \right) \quad (D.27)$$

\bar{D} : the mean diameter of the piston

Rewrite Eq.(D.25) and Eq.(D.27) in matrix form

$$\begin{pmatrix} m_p + m_r & m_p(L_y - L_x \tan \beta) \\ m_p L_y & I_p \end{pmatrix} \begin{pmatrix} \ddot{x}_p \\ \ddot{\theta}_p \end{pmatrix} = \begin{pmatrix} f_x \\ f_\theta \end{pmatrix} \quad (D.28)$$

where

$$\begin{cases} f_x = -F_l \sin\beta + \sum F_{Ai} + \sum F_{ri} - \sum F_{Ei} + F \\ f_\theta = m_p L_x \ddot{y}_p + T_p + \sum F_{Ei} H_{Ei} + F_{f2} \left(\frac{\bar{D}}{2} - x_{po} \right) + F_g x_{po} + F_{kr} H_{kr} \\ \quad + \sum F_{ri} H_{ri} - \sum F_{Ai} H_{Ai} - F_{f1} \left(\frac{\bar{D}}{2} + x_{po} \right) \end{cases}$$

3.2 Equation of motion of elastic vibration of piston

Elastic vibration amplitude of piston at point i is the superposition of each eigen vector $\phi_{i,n}$

$$x_{pi} = \sum_{n=1}^N \phi_{i,n} a_n(t) \quad (\text{D.29})$$

a_n : the n-th mode response of piston

The equation of motion

$$\tilde{m}_{Pn} \ddot{a}_n + 2\zeta_n \omega_n \tilde{m}_{Pn} \dot{a}_n + \tilde{m}_{Pn} \omega_n^2 a_n = \tilde{f}_{Pn} \quad (\text{D.30})$$

$$\left\{ \begin{array}{l} \tilde{m}_{Pn} : \text{modal mass} \\ \zeta_n : \text{damping ratio} \\ \omega_n : \text{natural circular frequency of n-th mode of piston} \\ \tilde{f}_{Pn} = \sum F_{Ai} \phi_{Ai,n} - \sum F_{Ei,n} \phi_{Ei,n} : \text{Modal force} \end{array} \right.$$

3.3 Equation of motion of elastic vibration of liner

Vibration amplitude of liner is the sum of eigen mode $\psi_{i,n}$

$$x_{Li} = \sum_{n=1}^N \psi_{i,n} b_n \quad (\text{D.31})$$

b_n : the n-th mode response of liner

The equation of motion

$$\tilde{m}_{L_n} \ddot{b}_n + 2\zeta_n \omega_n \tilde{m}_{L_n} \dot{b}_n + \tilde{m}_{L_n} \omega_n^2 b_n = \tilde{f}_{L_n} \quad (\text{D.32})$$

$$\text{Modal force: } \tilde{f}_{L_n} = -\sum F_{A_i} \psi_{A_i, n} + \sum F_{E_i, n} \psi_{E_i, n}$$

3.4 Coupled vibration response of piston and liner system

Rewrite the Eq.(D.28), Eq.(D.30) and Eq.(D.32) in matrix form, we can get the following equation

$$\begin{pmatrix} M_{P1} \\ \\ M_{P2} \\ \\ M_L \end{pmatrix} \begin{pmatrix} \ddot{x}_P \\ \ddot{\theta}_P \\ \ddot{A} \\ \ddot{B} \end{pmatrix} + \begin{pmatrix} C_{P2} \\ \\ C_L \end{pmatrix} \begin{pmatrix} \dot{x}_P \\ \dot{\theta}_P \\ \dot{A} \\ \dot{B} \end{pmatrix} + \begin{pmatrix} K_{P2} \\ \\ K_L \end{pmatrix} \begin{pmatrix} x_P \\ \theta_P \\ A \\ B \end{pmatrix} = \begin{pmatrix} f_x \\ f_\theta \\ \tilde{F}_{P2} \\ \tilde{F}_L \end{pmatrix}$$

where

$$\begin{aligned} M_{P1} &= \begin{pmatrix} m_p + m_r & m_p(L_y - L_x \tan \beta) \\ m_p L_y & I_p \end{pmatrix} & M_{P2} &= \begin{pmatrix} \ddots & & \\ & \tilde{m}_{Pn} & \\ & & \ddots \end{pmatrix} \\ M_L &= \begin{pmatrix} \ddots & & \\ & \tilde{m}_{Ln} & \\ & & \ddots \end{pmatrix} & C_{P2} &= \begin{pmatrix} \ddots & & \\ & 2\zeta_n \omega_n \tilde{m}_{Pn} & \\ & & \ddots \end{pmatrix} & C_L &= \begin{pmatrix} \ddots & & \\ & 2\zeta_n \omega_n \tilde{m}_{Ln} & \\ & & \ddots \end{pmatrix} \\ K_{P2} &= \begin{pmatrix} \ddots & & \\ & \tilde{m}_{Pn} \omega_n^2 & \\ & & \ddots \end{pmatrix} & K_L &= \begin{pmatrix} \ddots & & \\ & \tilde{m}_{Ln} \omega_n^2 & \\ & & \ddots \end{pmatrix} \\ A &= \begin{pmatrix} a_1 \\ a_2 \\ \vdots \\ a_n \end{pmatrix} & B &= \begin{pmatrix} b_1 \\ b_2 \\ \vdots \\ b_n \end{pmatrix} & \tilde{F}_{P2} &= \begin{pmatrix} \tilde{f}_{P1} \\ \tilde{f}_{P2} \\ \vdots \\ \tilde{f}_{P3} \end{pmatrix} & \tilde{F}_L &= \begin{pmatrix} \tilde{f}_{L1} \\ \tilde{f}_{L2} \\ \vdots \\ \tilde{f}_{L3} \end{pmatrix} \end{aligned}$$

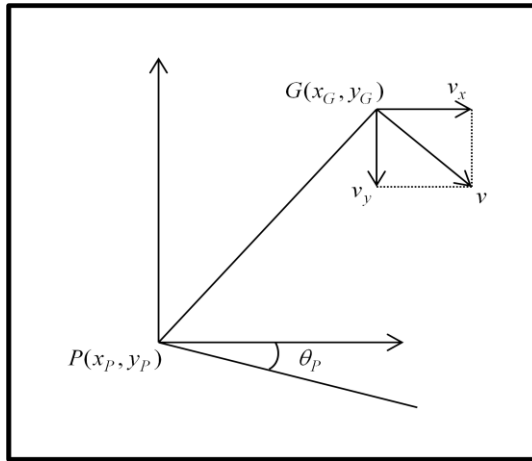


Fig.D.1 The relationship between piston pin and gravity of piston

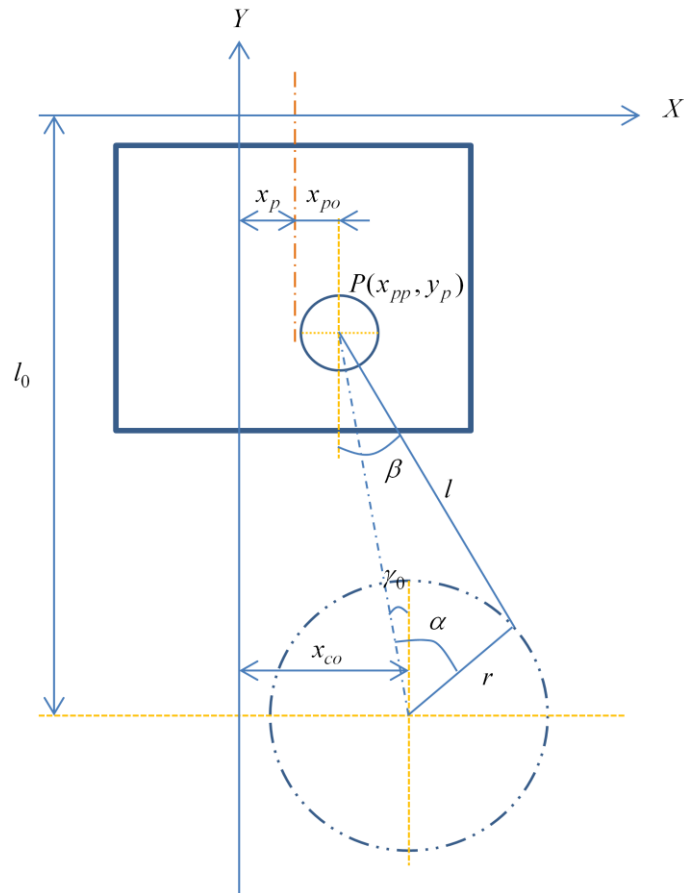


Fig.D.2 Piston motion and coordinates in vertical direction

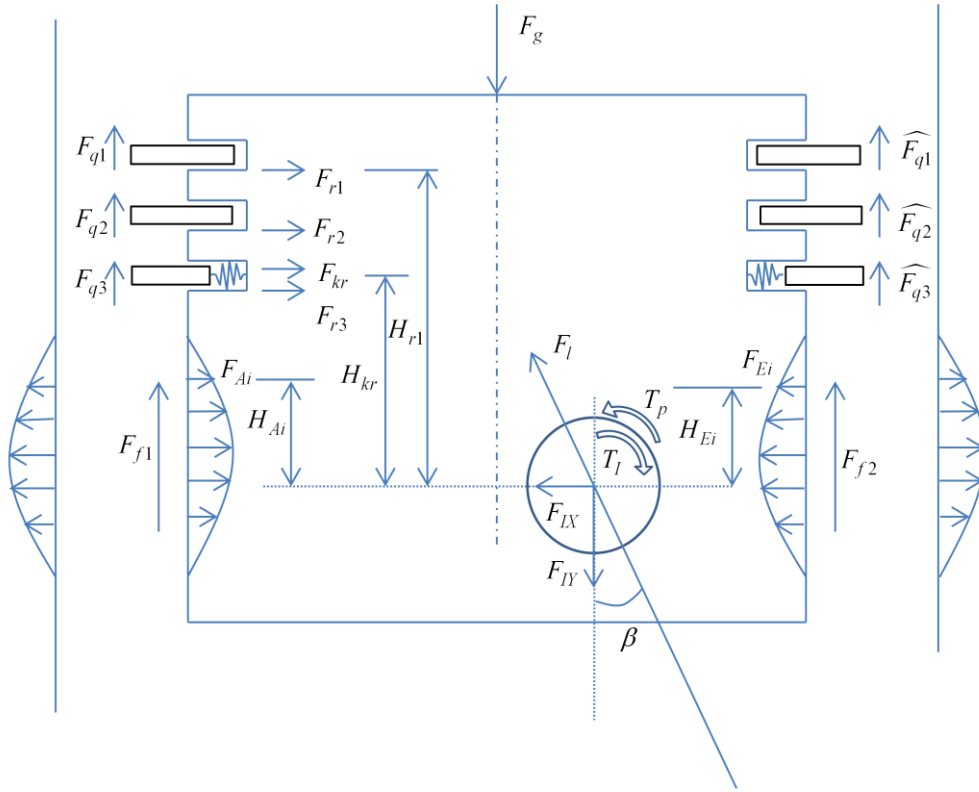


Fig.D.3 Forces applied on the piston liner system

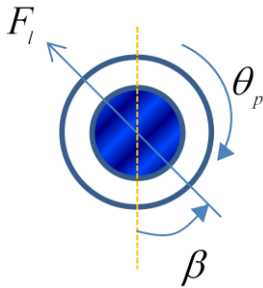


Fig.D.4 Friction between piston and piston pin

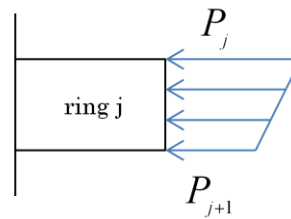


Fig.D.5 Average pressure on the ring

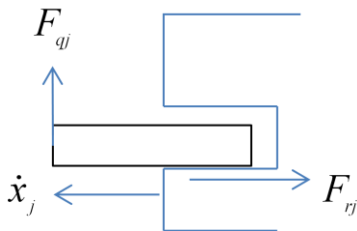


Fig.D.6 Friction force between ring and groove

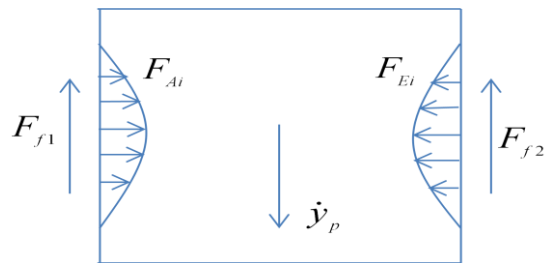


Fig.D.7 Friction force between piston and liner in vertical direction

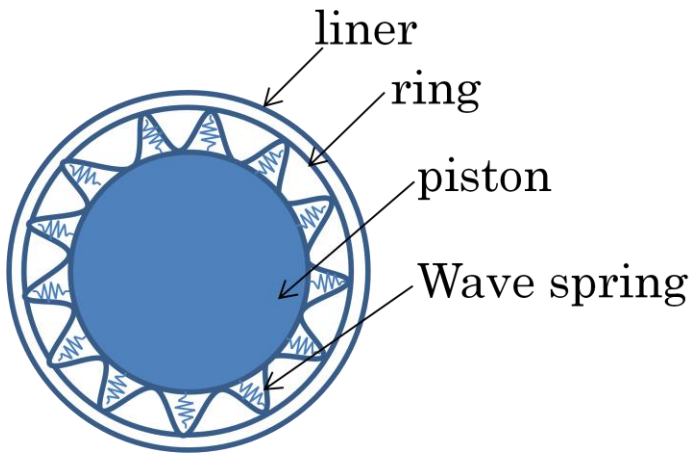


Fig.D.8 Structure of wave spring

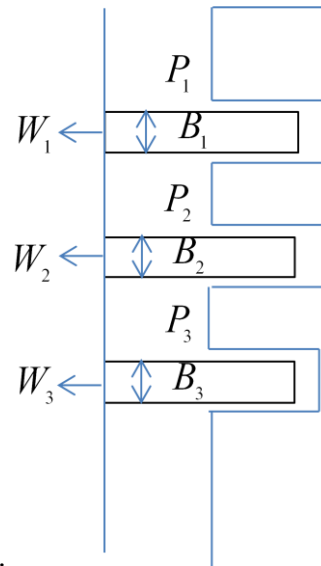


Fig.D.9 Compress force between ring and liner

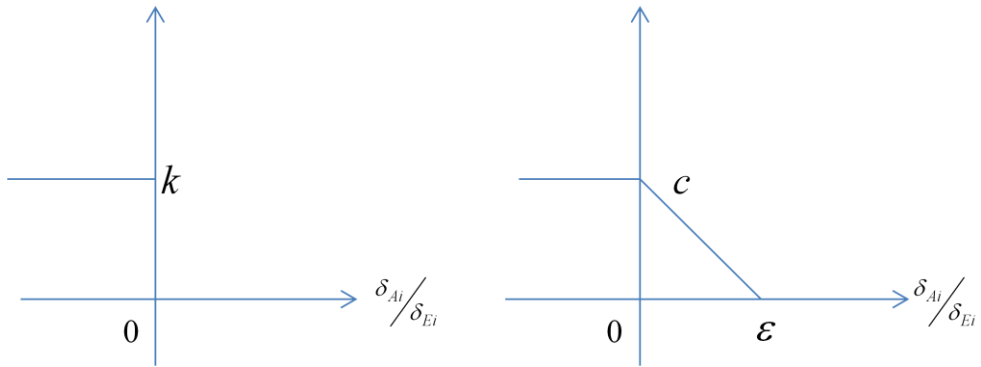


Fig.D.10 Spring and damping coefficients at compact points